UNIVERSITÀ DEGLI STUDI DI ROMA
"TOR VERGATA"
Facoltà di Scienze Matematiche, Fisiche e Naturali

Dottorato Di Ricerca in Astronomia
XXI ciclo (2006-2008)

Near infrared diagnostics of Class 0/I protostars: the jets and accretion region

Rebeca García López

A.A. 2008/2009

Relatore esterno: Dott.ssa Brunella Nisini

Relatore interno: Prof. Roberto Buonanno

Coordinatore: Prof. Pasquale Mazzotta

Dedicado a mis abuelos Raquel y Marcelino.

Abstract

In this thesis a study of the accretion and ejection properties of low mass embedded protostar (the so-called Class 0/I sources) through ISAAC NIR high angular observations is presented. The physics, kinematics and dynamics of five Class 0/I jets (HH1, HH111,HH212 / HH34, HH46-47) have been analysed in order to give some insights about the jet generation and the dependence of the jet properties on the evolutionary stage of the source. In addition, the accretion properties of a sample of ten Class I sources have been measured in order to revise their evolutionary status.

All the studied jets have been observed through atomic and molecular emission, traced by [Fe II] and H_2 transitions. Applying near-IR diagnostic techniques important physical parameters have been inferred. In particular, one milestone of this thesis was to derive the physical properties of embedded protostellar jets as a function of the jet radial velocity. For instance, at large distances from the source, the electron density (n_e) has been found to decrease with lower velocities. Average values over the brightest knots of 2600-6200 cm^{-3} have been found. The amount of mass transported along the flows has been also inferred. The results show that Class 0/I jets transport more mass than the more evolved jets from CTTS, while the accretion to ejection ratio remains roughly constant independently of the evolutionary stage of the source.

The inner region of Class I jets has been studied in detail in order to constrain the jet launching mechanism. Similarly to what found in CTTS jets, Class I jets present two velocity components at high and low velocity (the HVC and LVC) in both the atomic and molecular gas. The LVC in Class I jets reaches, however, larger distances (up to $\sim$ 1000 AU from the source) with respect to jets from CTTS. At variance with what found at large distances from the source, in the inner jet region, n_e increases with decreasing velocity, while the mass flux along the jet is always higher in the HVC. When comparing these results with the predictions of MHD jet launching models, the kinematical characteristics of the line emission are found to be, at least qualitatively, reproduced by the studied models. None of them can explain, however, the extent of the LVC and the velocity dependence of electron density that is observed.

On the other hand, the study of the set of Class I sources reveals no clear correlation between accretion and ejection features. In addition, in spite of what is expected by embedded protostars, only four of the ten sources show accretion dominated luminosities. This result suggests that most of the objects considered as Class I sources are, instead, more evolved sources that have already acquired most of their mass. Despite this fact, the inferred mass accretion rates are larger that those found in CTTS of the same mass.

Sommario

In questa tesi viene presentata una analisi detagliata delle propietà di accrescimento ed eiezione da stelle giovanni estinte di basa massa attraverso osservazioni ad alta risoluzione angolare nel vicino infrarosso effettuate con la camera infrarossa ISAAC. In questo modo, sono state analizzate la fisica, cinematica e dinamica di 5 getti di Classe 0/I (HH1, HH111, HH212 / HH34, HH46-47) al fine di ricavare informazioni circa l'origine dei getti e la dipendenza delle loro propietà fisiche rispetto allo stadio evolutivo della sorgente. Inoltre, le propietà di accrescimento di un campione di dieci sorgenti di Classe I sono state misurate con lo scopo di acertare loro stadio evolutivo.

Tutti i getti studiati sono stati osservati per mezzo di emisione atomica e molecolare, traciate da righe di [Fe II] e H_2. Applicando tecniche di daignostica nel vicino infrarosso, sono stati ricavati importanti parametri fisici. In particolare, un punto fondamentale di questa tesi è stato derivare come varianno le propietà fisiche di questi oggetti in funzione della velocità radiale dello getto. Ad essempio, ne risulta che la densità elettronica decresce al diminuire della velocità a grande distanza dalla sorgente, con valori medi intorno 2600-6200 cm^{-3}. Inoltre, è stata ricavata la masa trasportata da i getti che risulta maggiore di quella trovata in oggetti più evoluti di tipo TTauri, mentre il rapporto tra eiezione e accrescimento rimane approssimativamente costante indipendentemente dallo stato evolutivo dalla sorgente.

È stata altresì studiata in detaglio la regione interna dei getti di Classe I con il preciso fine di determinarne il mechanismo di lancio. Come per i getti da stelle di tipo TTauri, la cinematica delle regioni interne è caratterizzata da due componenti ad alta e bassa velocità (HVC and LVC) in entrambe le emissioni atomiche e molecolare. La componente a bassa velocità nei getti di Class I ragiunge distanze maggiori dalla sorgente (fino a 1000 AU) che nei getti di tipo TTauri. Inoltre, contrariamente a quanto trovato lontano dalla sorgente, nelle vicinanze della stella la densità elettronica aumenta al diminuire della velocità, mentre la componente ad alta velocità trasporta sempre la maggiore quantità di masa. I risultati qui mostrati sono stati inoltre confrontati con le predizione trovate dai modelli di lancio di getti. Mentre le propietà cinematiche sono, al meno qualitativamente, riprodotte da questi modelli, nessuno di loro riesce ad spiegare l'andamento osservato dalla densità elettronica in funzione della velocità.

D'altraparte, non è possibile stabilire alcuna correlazione tra la presenza di indicatori di acrescimento ed egezione entro il campione di sorgenti di Classe I. Inoltre, diversamente da ciò che previsto per le stelle giovanni, soltanto quatro delle dieci sorgenti hanno una luminosità dominata da accrescimento. Questo risultato sembra suggerire che

la maggioranza di stelle giovanni clasificate come Classe I sono in realtà sorgenti molto più evolute che hanno già acquisito la maggior parte della loro massa. Nonostante ciò, i valori di tasa di accrescimento ottenuti sono in media più alti di quelli trovati in stelle di tipo TTauri della stessa massa.

Contents

List of Figures

List of Tables

Introduction

The star formation process is a fundamental issue in stellar physics. It represents, however, the less known process in the whole stellar evolution. This is mostly due to the difficulty of observing the protostars and the region nearby. Indeed, in the first stages of evolution, when most of the final stellar mass is accumulated, protostars are embedded in dense molecular clouds of gas and dust from which they originate. As a consequence, the younger protostars (the so-called Class 0 and I sources) are hidden to optical wavelengths and become only visible after they have dissipated most of their dense envelopes. This happens when they have overpassed their main accretion phase and are observed as pre-main sequence stars evolving towards the main sequence (Class II and III sources). Only during the last twenty years, thanks to the development of infrared instrumentation, it has been possible to perform extensive studies on star forming regions.

Embedded protostars are very complex systems composed by a dense core surrounded by a circumstellar disc and a dense envelope, which represents the store of infalling material. As matter flows from the disc to the protostar surface part of the material is ejected away from the star in the form of collimated bipolar jets. These jets have a fundamental role in the star formation process, since they remove angular momentum from the star-disc system, allowing the accretion of matter onto the protostar to proceed. In addition, they influence the final mass of the star as they disrupt infalling material dissipating the surrounding envelope. Accretion and ejection of matter are thus intimately associated and represent the fundamental mechanism regulating the formation of a solar mass star.

In spite of their crucial role, the details of these processes are still largely unknown. Several models have been so far proposed for the mechanism regulating the accretion process and the consequent formation of the collimated jet. Most of these models have been developed to explain the properties derived from optical observations of Class II TTauri stars, sources that have already accumulated most of their final mass. Little is known, however, about the application of the same mechanism to the younger and actively accreting Class 0/I sources.

The main observational difficulty is to investigate the inner regions of the embedded Class 0/I sources at a spatial resolution high enough to resolve the relevant spatial scales. The accretion disc and the jet launching regions are, indeed, characterised by a size of the order of 0.1-1 AU, which corresponds to angular sizes of less than a few milliarcseconds even in the nearest star-forming clouds. Such angular scales can be directly probed only through IR interferometric techniques that at present are still under development. Alternatively, observational constraints to these phenomena can be provided only through indirect tracers. In this respect, the study of the collimated jets provide a fundamental tool to get quantitative information on the active processes occurring in young stars. The jets extend up to large distances from their driving source, reaching regions at low obscuration where they can be studied in detail. As a consequence, the study of the jet often represents the only mean to indirectly infer some properties of its driving source. Protostellar jets interact with the ambient medium producing strong shock waves which compress and heat the gas: this, in turn, cools down by emitting atomic and molecular lines over a large spread of wavelengths. The near IR spectral region is particularly suited to study the jets from embedded objects because several bright transitions excited in shocks can be found in this wavelength domain, able to diagnose important physical parameters of the jet. IR sensitive spectroscopic observations can, moreover, penetrate close to the jet base, thus providing information on the physics occurring as near as possible to the jet origin.

In addition to the study of jets, important information of the accretion process can be also inferred through the observations of spatially not resolved line emission features characterising the IR spectra of Class I objects. Permitted HI lines, in particular, are believed to originate from the region of accretion that connects the circumstellar disc to the protostar. Their luminosity and profiles provide therefore an important tool to investigate whether the protostar is still actively accreting or has already accumulated its final mass.

High dispersion IR spectroscopy performed on 8-m class telescopes provides an excellent tool to perform the kind of investigations described above, since it couples the needed sensitivity and adequate spatial resolution with a spectral resolution high enough to study the dynamics of the matter in infall or being ejected from the source.

The work presented in this thesis aims at studying the accretion an ejection process in low mass embedded protostars (Class 0/I) through high resolution IR spectroscopy obtained with the ISAAC instrument at VLT. The work is divided in main parts whose goals are summarised below:

- The main part of this thesis deals with the detailed study of the physical and kinematical properties of five classical Class 0/I jets. Long-slit ISAAC spectra have been obtained with the slit aligned along the jets in order to derive important parameters as a function of the distance from the driving source. The IR investigation makes it possible to trace the jet very close to the central source. Thus, the excitation and dynamics of these jets have been probed as close as ~100 AU from their origin in less embedded Class I sources, where their properties have not been yet modified by the interaction with the surrounding medium and still retain important information about the jet acceleration mechanism. Diagnostic techniques employing ratios and luminosity of lines, e.g., [Fe II] and H_2 transitions, have been used to derive important physical parameters such as electron density (n_e) and mass flux rates ($\dot{M}_{jet}$) in the different jet velocity components. These parameters, together with the kinematical information, have been compared with the predictions of theoretical models to constrain the jet launching mechanism. The physical properties derived in our Class 0 and I sample will be also compared with those of the jets from more evolved CTTSs to understand if the excitation conditions and the dynamical properties change as a function of the source evolutionary state.

- The second part of the thesis address the accretion properties of a sample of ten Class I sources selected in the ρ Oph molecular cloud. The accretion properties and mass accretion rates of the sources have been measured from the luminosity of the permitted HI lines in order to investigate whether they are really sources in their main accretion phase or not. Indeed, it is usually assumed that the bolometric luminosity of Class I objects is dominated by the accretion luminosity due to the release of energy in the impact of the infalling matter onto the star surface. Should be this the case, we would expect that all the sources of our sample have a large L_{acc}/L_{bol} ratio. Mass accretion rates derived from the selected sources will be compared with the values measured in samples of TTauri stars to study if there is really an evolutionary sequence among Class I and Class II objects. This analysis will make it possible to discern whether the Class I are really younger than TTauri stars or they also are evolved objects but seen with edge-on circumstellar discs, thus appearing more embedded.

This thesis is structured as follows: In Chapter 1 a review of the star formation theory is presented, while in Chapter 2 a description of the present knowledge of the accretion an ejection properties of young stars is done, together with a brief description of the proposed models for these phenomena. In Chapter 3 the main diagnostic capabilities of IR emission lines are briefly described. The basic notions of IR spectra acquisition and analysis techniques are presented in Chapter 4 together with a discussion on the advantages and limitations of IR observations and a description of our source sample and instrument set-up. In Chapter 5 the results on the ejection properties of Class 0/I jets are presented, while in Chapter 6 the findings on the accretion properties of the studied Class I sources are shown. Finally, conclusions are presented, summarising the main results of this work and describing future projects.

Chapter 1

The birth of stars

1.1 From molecular clouds to protostars

Most of the protostars are born inside Giant Molecular Clouds (GMCs). These are the largest molecular structures in the galaxy with sizes ranging between 10 and 100 parsec (pc), masses from 10^4 to 10^6 $M_\odot$ and average kinetic energies of only ~10 K. Their principal chemical components are hydrogen (90%) and helium (9%), while the abundance of other elements depends mainly on the history of the cloud as, for example, the presence of some supernova explosion nearby. GMCs are far to be uniform with the dust and gas distributed along very complex and filamentary structures with areas of high density corresponding to star formation regions. Most of the information we have about GMCs is derived through the analysis of emission lines coming from rovibrational transitions of CO, CS or NH_3 molecules. Although the main constituent is H_2, molecular clouds cannot be mapped through this molecule due to the high temperatures (~510 K) required to excite detectable emission. The best tracer of the molecular cloud structure is the CO molecule since is quite abundant ($[CO]/H_2 \sim 10^{-4}$) and can be easily populated under collisions at low temperatures (T~ 5 K with n(H_2 >100 cm^{-3})). In addition, the CO dissociation energy is very high (11.09 eV) meaning that is a very stable molecule. The CO emission in our galaxy is located mainly in the spiral arms suggesting that GMCs have lifetimes of the order of 10^7 years. The larger is the molecular cloud the shorter is its lifetime. This is due to the photoevaporation produced by O and B stars that form inside large molecular clouds. These stars produce high energy photons that ionise and destroy their molecular surroundings.

The complicated density structure of GMCs (Fig. 1.1) can be roughly classified in terms of clouds, clumps and pre-stellar cores (Williams et al. 2000). Clumps are gravitationally bound structures inside which stellar clusters are formed. Pre-stellar cores are the smallest fragments out of which individual stars or multiple systems are born. These initially gravitationally bound condensations form from the fragmentation of molecular clumps. A large number of pre-stellar cores have now been observed, both in molecular line tracers of dense gas such as NH_3, CS, N_2H^+ and HCO^+ (Andre et al. 2000) and in sub-millimetre dust continuum (Kirk et al. 2002).

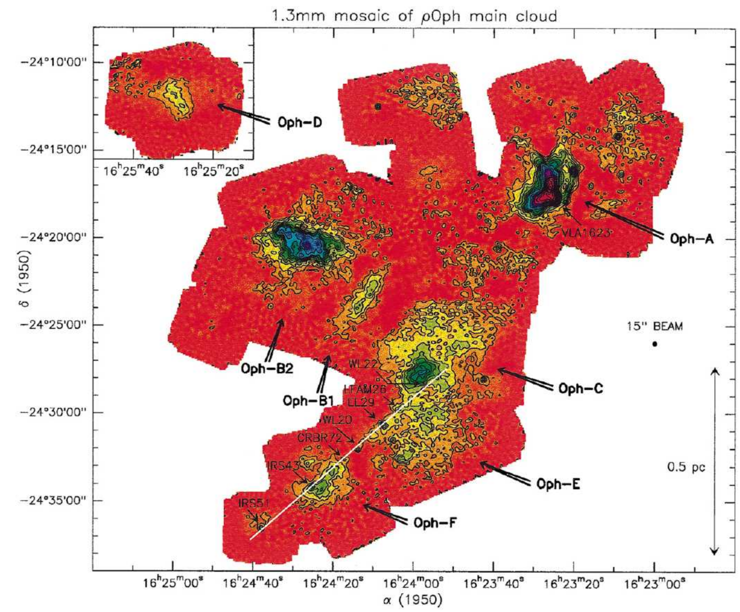

Figure 1.1: The ρ Ophiuchus molecular cloud complex mapped at 1.3 mm. Figure taken from Motte et al. (1998)

There is yet not a complete understanding of how stars are born from dense cores. A core begins to collapse when the thermal pressure of the gas within the core is no longer sufficient to contrast self-gravity. This means, in the classical theory proposed by Jeans (Jeans 1902), that collapse occurs when the gravitational energy of the cloud core is greater than its thermal energy,

$$|E_g| > E_{th} \tag{1.1}$$

which, for a homogeneous spherical core with mass M, radius R and temperature T, is given by:

$$\frac{3}{5}\frac{GM}{R} > \frac{3}{2}\frac{M}{\mu m_H}kT \tag{1.2}$$

where G is the gravitational constant, k the Boltzmann constant, μ the mean molecular weight and m_H the mass of the hydrogen atom. This inequality is, usually, expressed in terms of the Jeans mass M_J: gravitational collapse begins when the core mass M is greater than M_J,

$$M > M_J = \left(\frac{3}{4\pi\rho}\right)^{1/2}\left(\frac{5kT}{2G\mu m_H}\right)^{3/2} \simeq 6M_\odot\left(\frac{T^3}{n}\right)^{1/2} \tag{1.3}$$

where ρ is the density of the gas and $n = \rho/\mu m_H$ is the numerical density.

In absence of pressure support, the collapse due to gravitation occurs in a free-fall time:

$$t_{ff} = \left(\frac{3\pi}{32G\rho}\right)^{1/2} \simeq 1.4 \times 10^6 \left(\frac{n}{10^3[cm^{-3}]}\right)[yr] \tag{1.4}$$

If T=10 K and $n \geq$50 cm^{-3}, which are typical values for GMCs, we have $M_J \simeq$100 M$_\odot$and $t_{ff} \simeq$10^5 yr. These values are smaller than the observed values of mass (10^4-10^6 M$_\odot$) and lifetime (>10^7 yr) of the clouds. Thus, on the basis of the classical theory, molecular clouds should be small short-lived structures with a star formation rate of about 250-300 M$_\odot$ yr^{-1}, while observations indicate rates of only 3 M$_\odot$ yr^{-1}.

The Jeans criterion is thus unable to describe observational data, providing only a necessary and not sufficient condition to have an unavoidable collapse. Other mechanisms capable of hampering and delaying gravitational contraction must be, therefore, present within the clouds.

Nowadays, three physical mechanisms are believed to concur with the thermal pressure in supporting the core against self-gravity: magnetic field, core rotation and gas turbulence. Thus, the most general condition to be satisfied is:

$$|E_g| > E_{th} + E_{mag} + E_{turb} + E_{rot}, \tag{1.5}$$

where E_{th} is the thermal energy due to gas pressure, E_{mag} is the magnetic energy due to magnetic pressure and E_{turb} and E_{rot} are the terms due to turbulence and rotational velocity of the clumps, respectively. We will now briefly describe these terms:

- **Rotation:** From measurements of the rotational velocity by means of the study of Doppler shifts in lines from molecular species, we know that the cores rotate very slowly ($\Omega \sim 10^{-13} - 10^{-14}$ rad/s, Goodman et al. 1993). Therefore, E_{rot} can be neglected if we compare it with the pressure gradients and the self-gravity. This rotation play a fundamental role, however in the formation of protostellar disc as we will see in Sect. 1.2.

- **Magnetic field:** The presence of a magnetic field B (usually smaller than 10 μG in molecular clouds and up to 50 μG in the cores) provides support against gravitational collapse because the ions present in the cloud gas tend to couple with the magnetic field lines. Moreover, neutral constituents are affected by this phenomenon, since collisions couple ions with neutrals, resulting in an overall magnetic pressure which halts and slows down gravitational contraction. Assuming that the magnetic energy is the only term capable to compensate the gravitational energy of the cloud in eq. 1.5, the criterion for core collapse can be expressed in terms of critical magnetic mass M_ϕ:

$$M > M_\phi \simeq 0.3G^{-1/2}BR^2 = 200M_\odot \left(\frac{B}{3[\mu G]}\right)\left(\frac{R}{1[pc]}\right)^2 \tag{1.6}$$

  If the cloud mass M exceeds M_ϕ, the cloud globally implodes forming stars: this is the case of high mass stars in magnetically supercritical cloud cores ($M \gg M_\phi$), where the collapse takes place in a free-fall time-scale t_{ff}. Otherwise, the formation of low mass stars occurs in magnetically subcritical cloud cores ($M \ll M_\phi$), that are quasi-static equilibrium structures resulting from the balance of gravitational, magnetic and pressure forces. The core collapse in these systems occurs because of a process called “ambipolar diffusion”: since ions and neutrals are not strongly coupled, the neutrals can drift across the field lines resulting in a gravitational condensation of the cloud matter without compressing the magnetic field lines. Truly neutral drift motion deforms the magnetic field lines, producing Alfvén waves that dissipate the magnetic field. As a result, ambipolar diffusion produces the effect of decreasing the critical magnetic mass, so that the core can collapse when $M \gg M_{\phi}$ in a time-scale (ambipolar diffusion time t_{AD}) that depends on the efficiency of the coupling between ions and neutrals. For typical values of molecular cores t_{AD} ~$5{\times}10^6$ yr, one order longer than the free-fall t_{ff}.

Magnetic diffusion was believed to be the dominant physical process controlling star formation and it was widely accepted in the 80s. During the last decade, with the improvement in instrumentation and computer modelling techniques, this theory has seemed, however, to fail on some aspects, although the debate is still open. Indeed, observations seem to suggest that protostellar cores are supercritical (i.e. the magnetic fields are too week to retard the gravitational collapse of cores) and infall motions detected in the cores contradict the long lasting phase that is expected in the standard theory. Finally, a high fraction of cores which contain embedded protostellar objects is observed: if cores evolved on ambipolar diffusion time-scales, we would expect to find a significantly larger number of starless cores.

- **Supersonic turbulence:** During the last decade, substantial observational evidence suggests that supersonic turbulence is the main process controlling star formation.

  The random supersonic motion in molecular clouds is described by the Mach number $M = v_{turb}/c_s$, where $v_{turb} = \sqrt{\langle v^2 \rangle}$ is the average speed of the random motions and c_s is the sound speed. The observational evidence of this motion comes from velocity dispersion measurements of molecular line widths of 4-6 km s^{-1}, that cannot be accounted for unless considering non-thermal motions.

  Turbulent supersonic motion is a dissipative phenomenon able to reallocate energy inside the cloud, providing a global support against gravitational collapse. The dissipation time for turbulent kinetic energy is indeed:

$$t_d = \frac{L_d}{v_{turb}} = 3\,Myr \left(\frac{L_d}{50[pc]}\right)\left(\frac{v_{turb}}{6[kms^{-1}]}\right)^{-1} \tag{1.7}$$

  where L_d is the driving scale of the turbulence. Numerical methods and computer simulations demonstrate that supersonic turbulence within large clouds would dissipate in a time-scale which is comparable to the free-fall time-scale. A recurring injection of energy is, then, needed to maintain turbulence as long as is necessary to obtain the observed core contraction times. Several mechanisms have been considered, such as galactic rotation, MHD wave propagation, protostellar outflows and, in particular, supernova explosions.

1.2 The evolution of Young Stellar Objects (YSOs)

As described above, low-mass star formation is thought to occur when a molecular cloud core becomes unstable and begins to collapse. During the last years, several studies have been done trying to measure the infalling motions gas within the cloud core. However, the detection of these motions are very difficult. The velocities of collapse are too small if we compare them with the random motions inside the molecular cloud. This fact becomes extreme if we try to distinguish the infall motion against fast molecular gas put in motion by bipolar outflows (see Sect. 2.1). On top of all this, the highest velocities are expected to be present in the central regions of the cloud, where, however, the amount of mass is really low and the extinction is very high.

Despite the lack of measurements of infalling velocities, some theoretical models have been developed in order to give some light about the very first phases of the stellar evolution. One of the simplest models assumes that the molecular core about to collapse presents a density profile $\rho \propto R^{-2}$ (singular isothermal sphere in quasi-equilibrium between thermal pressure and gravity). When the structure becomes gravitationally unstable, the collapse starts, following the free-fall time-scale. Being $\tau_{ff} \propto \rho^{-1/2}$, the central zones collapse more rapidly than the outer part. As a result, at the centre of the structure a core in hydrostatic equilibrium is formed, which accretes matter from the surrounding infalling envelope. In this simple infall model, with an initial cloud spherically symmetric that exhibits asymmetric rotation, the infall solution has complete symmetry above and below the equatorial plane. With this assumption, the momentum fluxes of infalling material on either side of the equatorial disc plane perpendicular to the disc are equal in magnitude and opposite in direction. The result is that the infalling gas must pass through a shock at the equator, which cancels the kinetic energy component perpendicular to it. This process will lead to an accumulation of matter in a thin structure in the equatorial plane, i.e., a rotating disc. Ultimately, disc material will be redistributed by the process of angular momentum transport and energy loss driving disc accretion. The accretion rate depends on the sound speed in the medium ($c_s = (kT/\mu m_H)^{1/2}$):

$$\frac{dM}{dT} \equiv \dot{M}_{acc} = \rho 4\pi R^2 c_s = 2\frac{c_s^3}{G} \tag{1.8}$$

For typical values, accretion rates of $\sim 10^{-5}$-10^{-6} $M_\odot yr^{-1}$ are derived. In this way, the time expected for the formation of a solar mass star is around 10^6 years. In this phase, there are no nuclear reactions in the star and the luminosity of the YSO comes from the energy realised during the accretion in the so called “accretion shocks”. Assuming a spherical geometry for the accretion, the luminosity emitted is given by the conversion of gravitational energy:

$$L_{acc} = \frac{GM_* \dot{M}_{acc}}{R_*} \tag{1.9}$$

where M_* and R_* are the mass and radius of the central condensation. For a typical values of low-mass protostars ($M_* = 1\,M_\odot$, $R_* = 4\,R_\odot$ and $\dot{M}_{acc} = 10^{-5}\,M_\odot/yr$) the accretion luminosity is around 50 $L_\odot$, much higher than the luminosity of a main sequence star with the same mass. It has been observed that the accretion process is usually accompanied by the ejection of material from the protostar. This is the origin of the so-called protostellar jets, the main topic of this thesis and described in detail in the following sections.

In the early stage of evolution, protostars have a low surface temperature (T < 2000 K) and thus emit most of their energy at IR wavelengths. In addition, the emitted radiation is absorbed by the external envelope and re-emitted at longer wavelengths. This means, that in the protostellar phase the YSO is not simply characterised by a single temperature and thus cannot be positioned in the Hertzsprung-Russel (HR) diagram. When the gravitational collapse finishes and the envelope has been dissipated, the YSO becomes visible at optical wavelengths and can be positioned in the HR diagram. This is the so-called pre-main sequence phase (see Fig. 1.2). At this stage, the star has almost reached its final mass and the accretion rate is very small, around 10^{-7}M$_{\odot}$/yr. In the pre-main sequence phase the central temperature of the stellar core is still too low to permit the hydrogen fusion into helium. Deuterium fusion occurs at temperatures lower than hydrogen fusion, but since deuterium abundance is relatively low, the deuterium fusion can last only for a short period of time ($\sim 1 \times 10^{-6}$ yr). Without fusion energy release, the protostar must contract, generating gravitational potential energy to replace the energy lost by the radiation of the stellar photosphere. Thus, the luminosity is mainly the energy irradiated by the stellar photosphere:

$$L_* = 4\pi R^2 \sigma T_{eff}^4 \tag{1.10}$$

where σ is the Stephen-Boltzmann constant and T$_{eff}$ is the temperature of the stellar photosphere. When protostars appear for the first time on the HR diagram, they are located along the so-called "birthline", whose position in the HR diagram depends on the protostellar accretion rate. While the protostar contracts (typical time-scale of 10^7 yr), it moves in the HR diagram along the pre-main sequence tracks. The contraction will stop when the star arrives in the main-sequence, at which point the energy released by the hydrogen fusion compensate the energy radiated by the stellar photosphere.

The low-mass (M $\lesssim$ 2 M$_{\odot}$) pre-main sequence stars, with stellar spectral types F-M are called T Tauri stars (Joy 1945). These stars are fully convective and follow the so-called Hayashi tracks, along which the temperature is roughly constant, while the luminosity decreases with the radius. Higher-mass (M ~2-10 M$_{\odot}$) pre-main sequence stars are named Herbig Ae/Be stars (Herbig 1960) to distinguish them from other types of more evolved A-B emission line stars. These stars have, at variance with TTauri, radiative nuclei and follow evolutionary tracks nearly horizontal (see Fig. 1.2).

1.3 The Spectral Energy Distribution classification of YSOs

The evolutionary status of a "normal", low-mass star can be determined by its position on the HR diagram (see previous section). This method works as far as the star produces a black-body like spectrum and thus can be accurately spectrally classified. This is, however, very difficult for most of the YSOs. The circumstellar gas and dust around these objects absorb and reprocess most of the radiation emitted by the embedded star, thus

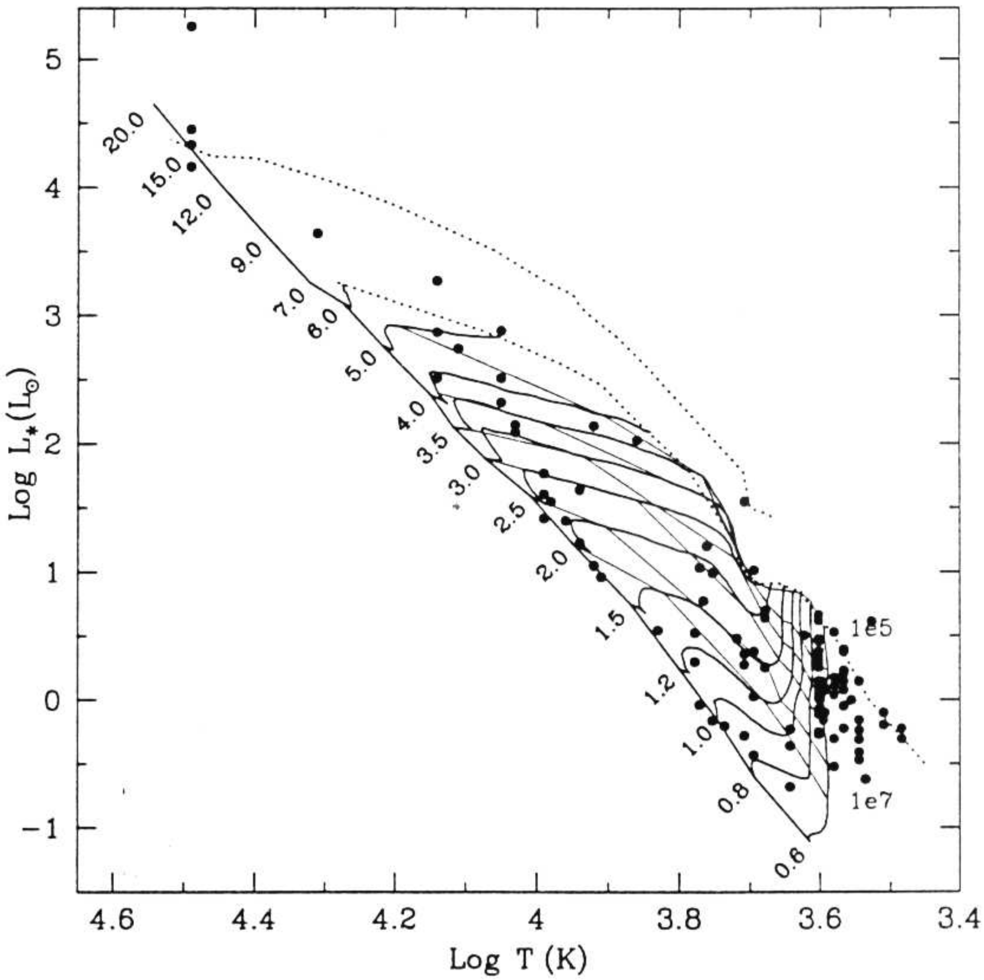

Figure 1.2: Hertzsprung-Russel diagram for a sample of T Tauri and Herbig Ae/Be pre-main sequence stars (black points). The evolutionary tracks (Palla & Stahler 1993) for stars with masses $M < 6\,M_\odot$ show the path of the stars from the birthline corresponding to an accretion rate of $10^{-5}\,M_\odot$/yr (bottom dotted line) to the Zero Age Main Sequence (ZAMS, solid line on the left). The top dotted line is the birthline corresponding to $\dot{M}_{acc} = 10^{-4}\,M_\odot$/yr. The evolutionary tracks are almost vertical (Hayashi tracks) for stellar masses smaller than $0.8M_\odot$, while the tracks relative to stellar masses between 2 and $6\,M_\odot$(Herbig Ae/Be stars) are horizontal. The birthline intersects the ZAMS for $M = 6\,M_\odot$, thus the stars with larger masses have not a pre-main sequence phase. The thinner solid lines are the isochrones for stellar ages of 10^5, 5×10^5, 10^6, 2×10^6, 5×10^6 and 10^7 yr.

altering its spectral appearance. In fact, the youngest objects are not detected at optical wavelengths due to the presence of a thick protostellar disc and a dense envelope that radiate most of their energy in the IR. In addition, in their first evolutionary stages, the circumstellar gas and envelopes have spatial extent larger than the protostar photosphere itself and thus, the YSO will exhibit a wide range of effective temperatures. As a result, the detected spectral distribution is much wider than a simple black-body spectrum. For all these reasons to place a YSO on a HR diagram is very difficult.

Lada (1987) found that the infrared sources could be classified as a function of their IR energy distributions (i.e., log(λF_λ) vs. log(λ)). The shape of the broad-band IR spectrum of a YSO depends both on the nature and distribution of the surrounding material. We would expect that more embedded objects show a spectral distribution with a black-body profile at the dense envelope temperature, while more evolved objects should have a spectral distribution characterised by the black-body emission of the central protostar (since they should be accreted most of their surrounding material). In this way, the spectral energy distribution (SED) of a YSO can give some clues about its evolutionary status.

Lada & Wilking (1984) classified the YSOs as a function of their SED from Class I to Class III objects. With the pass of the years it was necessary to include a new type of colder objects, the Class 0 objects (Andre et al. 1993). This first stage (see Fig. 1.3) corresponds to a very embedded protostar, where the mass of the central core is small in comparison to the mass of the accreting envelope. The SED of these objects is characterised by the blackbody emission of the envelope and peaks at sub-millimeter wavelengths. The accretion rate of Class 0 objects is very high, of the order of $\dot{M}_{acc} \sim 10^{-4}$ $M_\odot$/yr. The next stage is represented by the Class I objects. They are poor evolved embedded stars with less mass in the envelope and more massive central cores with respect to the Class 0 objects. Their SED peaks in the far-infrared and is characterised by a weak contribution of the blackbody of the central star (detected at near-IR wavelengths) and the emission of a thick disc and dense envelope. The accretion rate is lower than in Class 0 objects with a typical value of the order of $\dot{M}_{acc} \sim 10^{-6}$ $M_\odot$/yr. Class II objects are the classical T Tauri stars (CTTS) with a SED due to the emission of a thin disc and the central star. They have accumulated most of their final mass, dispersed quite completely their circumstellar envelope, but still accreting at a very low rate of the order of $\dot{M}_{acc} \sim 10^{-7}$-$10^{-8}$ $M_\odot$/yr. Finally, Class III objects have pure photospheric spectra. Their SED is peaked in the optical and is well approximated by a blackbody emission with a faint infrared excess due to the presence of a residual optically thin disc that may be the origin of planetesimals.

This classification scheme can be made more quantitative by defining the spectral index:

$$\alpha = \frac{dln(\lambda F_\lambda}{dln(\lambda)} \tag{1.11}$$

defining the slope of the spectrum between 2 and 12 μm . α varies from 0 to +3 for Class I objects, -2 < α < 0 in Class II objects and for Class III objects it ranges from -3 to -2. This variation in SED shape represents an evolutionary sequence corresponding to the gradual dissipation of gas and dust envelopes around young stars. Adams et al. (1987) were able to theoretically model this empirical sequence from protostar to young main

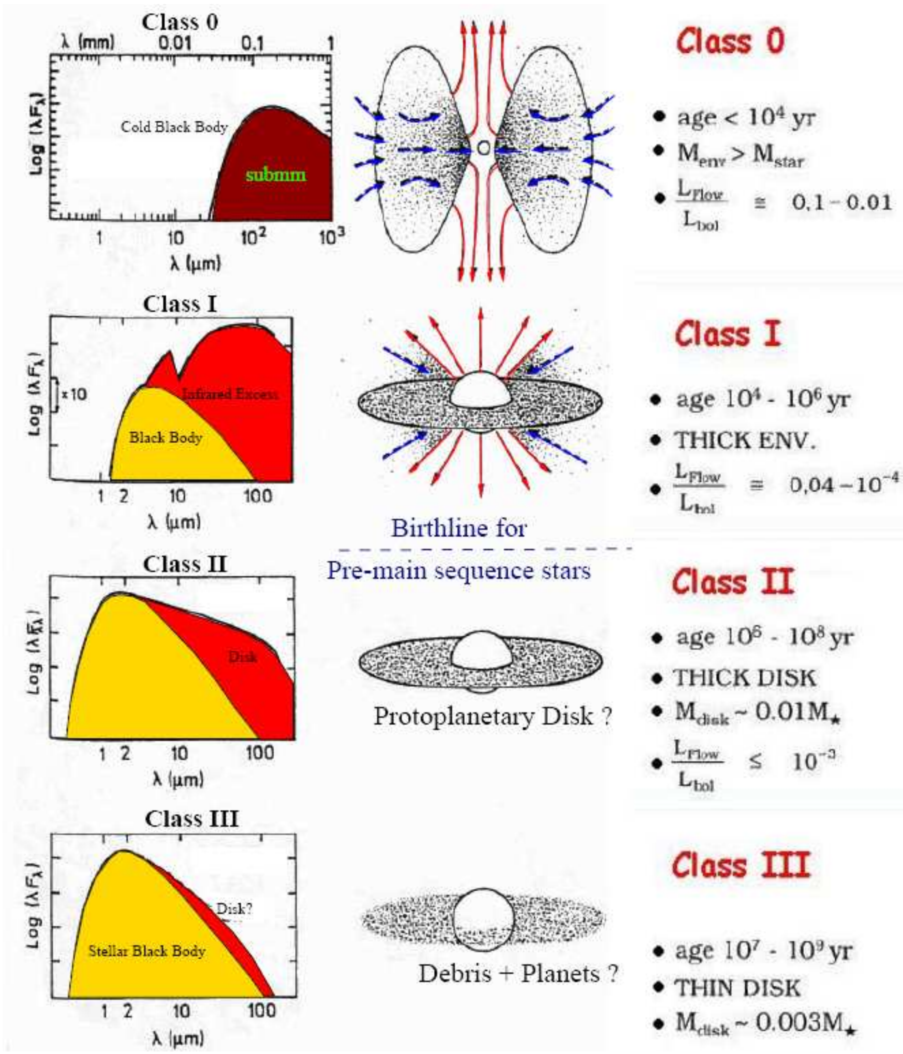

Figure 1.3: Schematic description of the various phases that characterise the formation of an individual star, from the earliest main accretion phase (Class 0), to the time when all the circumstellar matter is dissipated (Class III). The SED typical of objects in the various phases is represented on the left, while typical physical parameters of YSO according to their classification are listed on the right.

sequence stars.

Today this classification must be applied with some caution. Although the general scheme is probably correct, recent observations have lead to some doubts about the existence of real physical differences between many Class I and II objects. Geometrical effects due to the orientation of the structures with respect to the observing line of sight may alter the shape of the SED causing a misclassification of the objects. This issue will be addressed in the second part of this thesis (Chap. 6).

Chapter 2

Ejection and accretion of material in low-mass YSOs

Accretion and ejection of matter are two phenomena intimately related during the formation of a star. This thesis reports an observational study of the ejection, through collimated jets, and accretion of matter in young embedded Class 0/I protostars. To put the presented work in a context, I will make here an overview of the present knowledge of the accretion an ejection properties of young stars, presenting also a brief description of the proposed models for these phenomena.

The Chapter is divided in two main sections dealing with jets (Sect. 2.1) and accretion properties of YSOs (Sect. 2.2).

The discussion about protostellar jets is subdivided into a summary of the main ejection models (Sect. 2.1.1), an overview of the large scale observational characteristics (Sect. 2.1.2) and a description of the physical properties found at the base of protostellar jets (Sect. 2.1.3).

Finally in Sects. 2.2.1 and 2.2.2 the accretion characteristics of CTTS and Class I sources are discussed separately.

2.1 Protostellar jets

The evolution from Class 0 to Class III requires the dissipation of the circumstellar material in the protostellar infalling envelope and in the disc. In principle, this could be done by accreting all the surrounding material onto the star. We know, however, that star forming cores contain more mass than the stars themselves. This suggests that at some point in the early evolution of a YSO the cloud material has been partially removed. In addition, the mass accretion process needs to be followed by the dissipation of angular momentum. In fact, to conserve angular momentum the star would be forced to rotate at increasing velocities leading to its break-up.

As noted in the previous chapter, the accretion process is associated with ejection of material from the star in form of energetic bipolar outflows since the first stages of proto-

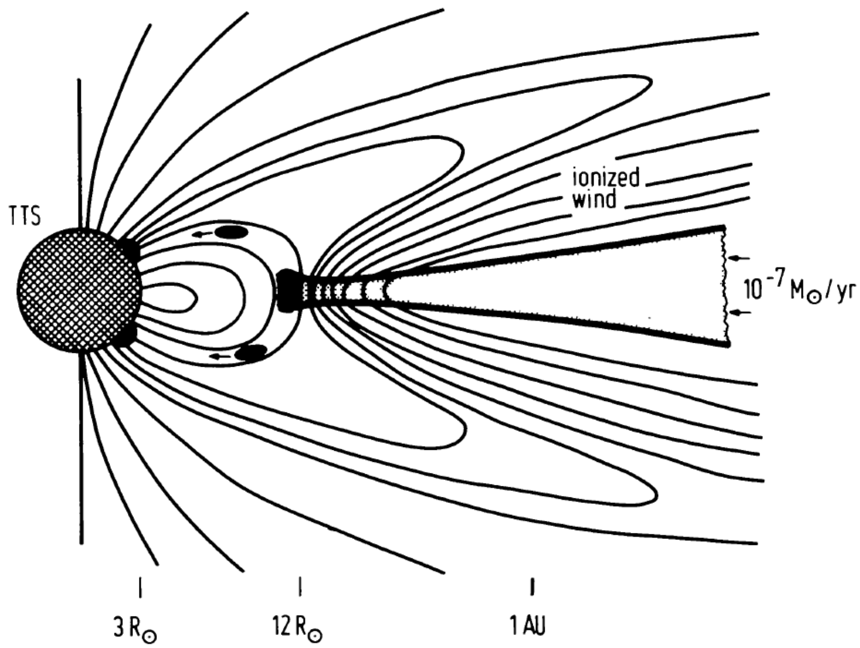

Figure 2.1: The interaction between the rotating magnetosphere of the central star and the circumstellar disc (Camenzind 1990).

stellar evolution . These supersonic and collimated jets significantly contribute at both the angular momentum removal and envelope dissipation. In fact, recent observations seem to indicate that protostellar jets rotate (Bacciotti et al. 2002; Coffey et al. 2004), suggesting that they can efficiently contribute to the remove of angular momentum from the system (Ferreira & Casse 2004), helping to spin-down the protostar (Ferreira et al. 2006) and allowing the accretion of material. In addition, as protostellar jets propagate supersonically through the molecular cloud, they disrupt infalling material from the collapsing cloud influencing the final mass of the protostar (Terebey et al. 1984). Protostellar jets have therefore a fundamental role in the star formation process, although the exact mechanism for their formation is still unclear.

In this section, the basics of theoretical models so far developed for the jet launching are presented, together with a general description of their physical properties as derived from observations.

2.1.1 The launching mechanism

Theoretical models for accretion and ejection of matter in YSOs have as a common element the influence of the magnetic field. The magnetic field structure in the inner regions of the star-disc system is believed to acquire a configuration like the one in Fig. 2.1. A magnetised star with a dipolar field configuration accretes material from a disc through the magnetic field lines. The magnetic field of the protostar is believed to be strong enough to truncate the disc at a few stellar radii from the star (the truncation radius or magne-

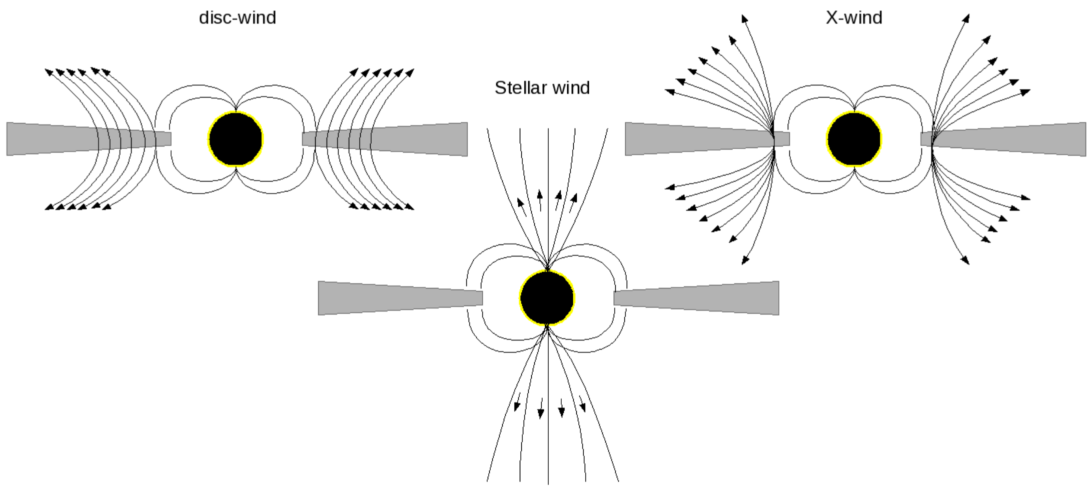

Figure 2.2: Possible locations for the launching of MHD winds in young stars: disc-wind model (upper panel, on the left), X-wind model (upper panel, on the right) and stellar wind (lower panel). In a disc-wind model, an extended magnetic field threads the disc, while in a X-wind model the magnetic field thread the disc through a singe annulus at the interaction point between the magnetosphere and the inner disc radio. When the field lines are anchored onto a rotating star we have a stellar wind.

topause) and creates a magnetospheric cavity as shown in the Fig. 2.1. Very briefly, the accretion process is supposed to occur as follows. The material from the outer parts of the disc spirals toward the inner disc region. At this point, if the material is ionised enough it will be forced to move longward the magnetic field lines to partially accrete onto the protostar and partially be ejected in a wind. When the material reaches the protostar surface, through the so-called accretion-columns, it produces strong accretion shocks that create hot spots on the star surface. There are several observational evidences for the presence of such hot spots on the surface of accreting protostars (see e.g. Bouvier et al. 1995).

The accretion is only possible if the truncation radius is smaller than the corotation radius (R_{CO}). The corotation radius is the radial distance at which the keplerian velocity of the material of the disc equals the stellar angular velocity. Outside the R_{CO}, the angular velocity of the star is larger than the keplerian velocity. Thus, the material along the field lines of the magnetosphere is thrown away due to the presence of a strong centrifugal force, thus generating a “wind”.

Following the general idea described above, various Magneto-Hydro-Dynamic (MHD) models have been proposed (Konigl & Pudritz 2000; Shu et al. 2000). It remains to be established, however, where the wind/jet is launched from: the circumstellar accretion disc, the rotating star, or its magnetosphere (or a combination of them). The most popular MHD ejection models are the X-wind, the disc-wind and the stellar wind (see Fig. 2.2). I will briefly describe below the main properties of each of these models.

Disc-wind and X-Wind model

In such models, a large scale magnetic field is assumed to thread the disc from its

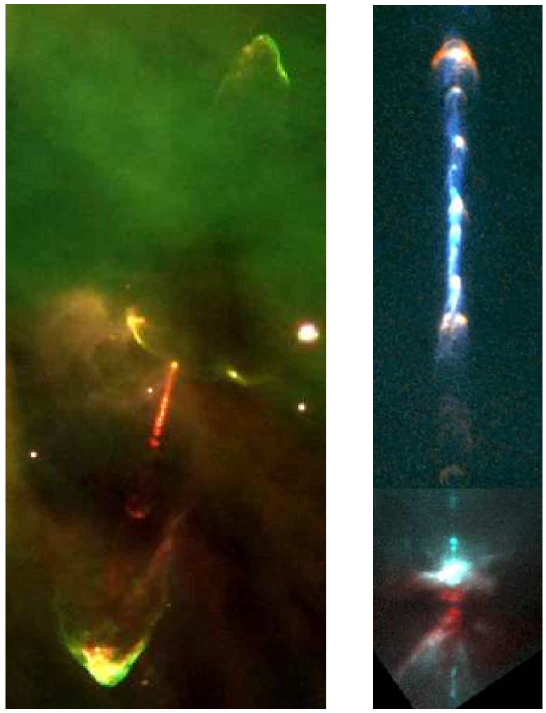

Figure 2.3: Left: the HH34 jet imaged by the VLT with the optical camera FORS2. Only the blue-shifted lobe of the jet is optically detected, while the red-shifted lobe remains invisible as propagates inside the cloud. Both lobes terminate in a typical bow-shock structure. Right. The HH111 jet imaged at optical and near-IR wavelengths by Hubble Space Telescope. This jet presents a typical morphology with a chain of knots and a bow-shock at the head of the flow. Figures taken from ESO Press Release 17/99 (left) and Reipurth et al. (1997;right).

inner radius to a certain external radius (smaller than the outer disc radius). In an extended disc-wind model, the magnetic field is threading the disc over an extended range of disc radii and thus the jet originates in a large disc region up to a few AUs from the star (Ferreira 1997). In a X-wind model (Shu et al. 1995) the magnetic field is anchored to a single disc annulus at the interaction region between the disc inner edge and the stellar magnetosphere.

The only difference between these two models is the amount of magnetic flux threading the disc. The ejection process is, in fact, identical: a recombination between the close stellar magnetic field lines and open field lines carrying accretion material. In both situations, jets carry away the exact amount of angular momentum required to allow accretion. However, the predicted terminal velocities and angular momentum fluxes are different and can be tested against observations (see Sect. 5.6.1).

MHD stellar winds

Self-collimated stellar winds are produced from open stellar magnetic field lines. However, the star has to rotate near the break-up in order to provide enough rotational

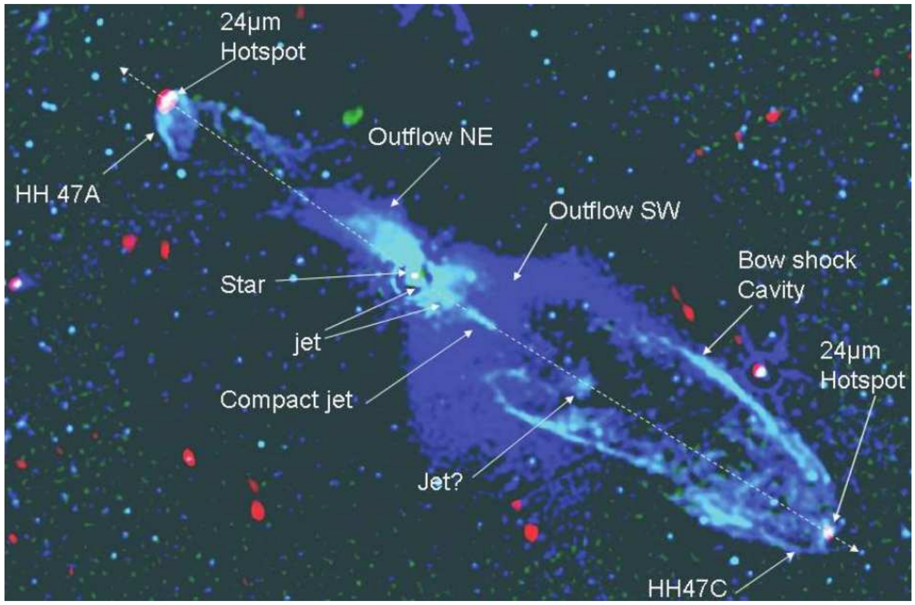

Figure 2.4: Spitzer image resulting from combining 3.6 μm(blue), 4.5+5.8 μm(green) and 24 μm(red) images of the HH46-47 protostellar jet. A wide-angle outflow cavity is clearly seen together with a compact jet propagating inside it. Two characteristic bow-shock structures are detected (HH47A and HH47C) corresponding to the end of the blue- and red-lobe of the outflow. Image taken from Velusamy et al. (2007).

energy to magnetically accelerate stellar winds. Low-mass protostars, such as TTauri stars, have been found to be slow rotators (see e.g. Bouvier 2007) and thus stellar winds can hardly provide the protostellar rotational energy necessary to launch the jet. Therefore, although the presence of stellar winds cannot be excluded, they seem not efficient enough to be the main responsible for the launching of the most energetic jets.

2.1.2 An observational overview of protostellar jets

The first evidences of outflow activity linked to the formation of a star have been discovered in the 1950's by Herbig (1950;1951) and Haro (1952;1953), who detected diffuse line emitting nebulae spatially not associated with any star. From the beginning, it was realised that these nebulae were linked to star formation since they were associated with star forming regions. However, their origin was unknown until the 1970's when Schwartz (1975) proposed that these objects (called Herbig-Haro, HH, objects) could be shock fronts moving away from the young star.

Enormous progresses have been done over the last 20 years on the understanding of jet physics through imaging and spectroscopy at different wavelengths, providing information about their morphology, kinematics and physical properties.

Protostellar jets are ejected perpendicular to the disc plane and are usually bipolar structures, although the red-shifted lobe is often hidden at optical wavelengths since it moves toward the cloud, through regions at high visual extinction (e.g., Fig. 2.3).

Class 0/I protostars usually drive outflows more energetic than more evolved objects as

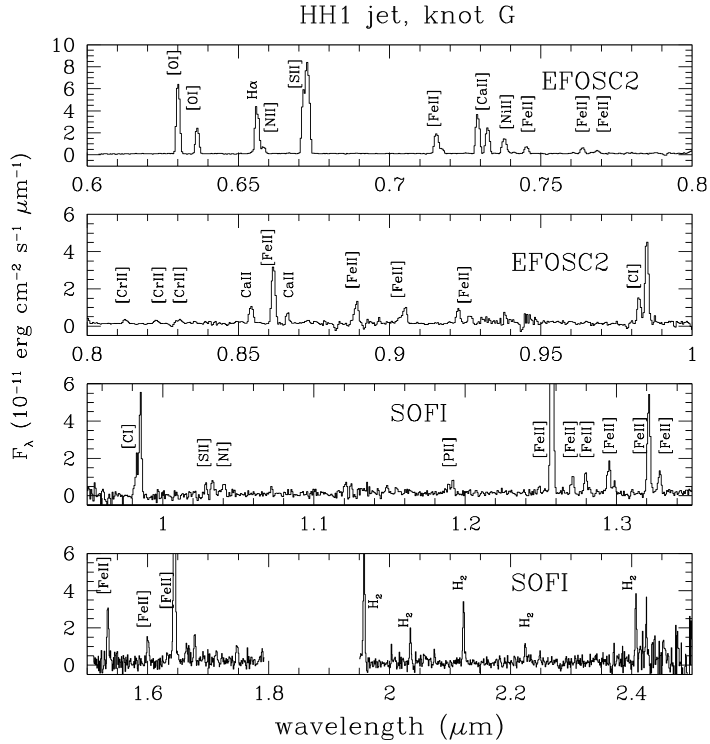

Figure 2.5: Spectrum of the HH1 jet from 0.6 to 2.5 μm. Several atomic and molecular emission lines are detected. Figure taken from Nisini et al. (2005b).

CTTS. It is believed that the younger is the object the larger is the accretion and thus, the higher is the amount of material ejected from the protostar. The supersonic jets, travelling at velocities ranging from 100 to 500 $\mathrm{km\,s^{-1}}$, impact with the ambient cloud generating emission knots and curved shock structures (bow shocks) at distances from few thousands of AU to several parsecs (McGroarty & Ray 2004). The leading bow-shock, expanding through the cloud create large cavities inside which the collimated jet propagates (see Fig. 2.4). The shocked regions are observed over a large range of wavelengths (from UV to radio) exhibiting a line spectrum usually with no continuum emission. The very fast shocks can even produce X-ray emission (Bonito et al. 2007). Usually, the youngest protostellar jets, i.e., Class 0 jets, are detected through molecular emission such as, H_2, CO and SiO at IR and mm wavelengths, while older objects (e.g. jets from CTTSs) emit mainly in the optical through forbidden emission lines from atoms or ions at low ionisation. Jets from Class I sources, which are the argument of this thesis, present both atomic and molecular components emitting the bulk of their energy in the IR (e.g. Fig. 2.5).

From the analysis of images and spectra taken at different epochs, it appears that jets are not static objects, as the knots position and velocity vary with time. Large proper motions have been inferred for the knots of several jets (see e.g. Bally et al. 2002; Hartigan et al. 1993), as well as jet wiggling, probably caused by the precession of the jet due to the

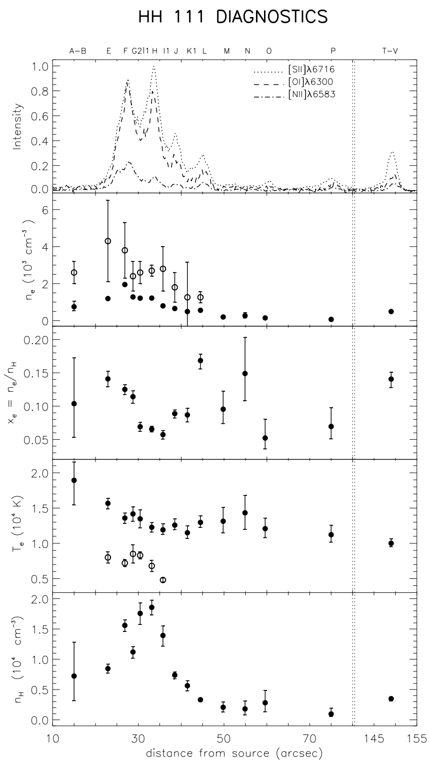

Figure 2.6: Variation of physical parameters along the HH111 jet. From top to bottom panel are represented: intensity profiles of the optical lines, the electron density, n_e, in units of 10^3 cm^{-3}, the ionisation fraction, x_e, the electron temperature, T_e in units of 10^4 K and the total density, n_H in units of 10^4 cm^{-3}. The open circles are the values derived from [Fe II] infrared lines, while filled circles represent values derived from [S II], [N II], [O I] optical lines.

misalignment of the jet axis with the rotational axis of the star (see e.g. Caratti o Garatti et al. 2008). These properties suggest that knots are likely to be internal working surfaces due to time ejection variability.

Detection of radial velocity asymmetries across the jet axis has been recently obtained through HST observations at sub-arcsecond resolution. These asymmetries have been interpreted as rotation of the jet around its axis (Coffey et al. 2004; Bacciotti et al. 2002), although other interpretations have been also proposed. If interpreted as rotation, these observations will imply that jets are the principal responsible for extracting excess angular momentum from the inner disc. Detailed information on jets main physical parameters has been obtained in the last years thanks to diagnostic techniques employing ratio and luminosity of optical and IR lines (e.g., Bacciotti & Eislöffel 1999; Nisini et al. 2005b). In optical jets from TTauri stars the combination of different lines as [S II],[Ni II], [O I] have been used to derive fundamental parameters such as temperature, electron density and ionisation fraction. IR lines can be instead used to infer some physical parameters of embedded jets, as will be described in detail in Chap. 3. Class 0 jets are characterised

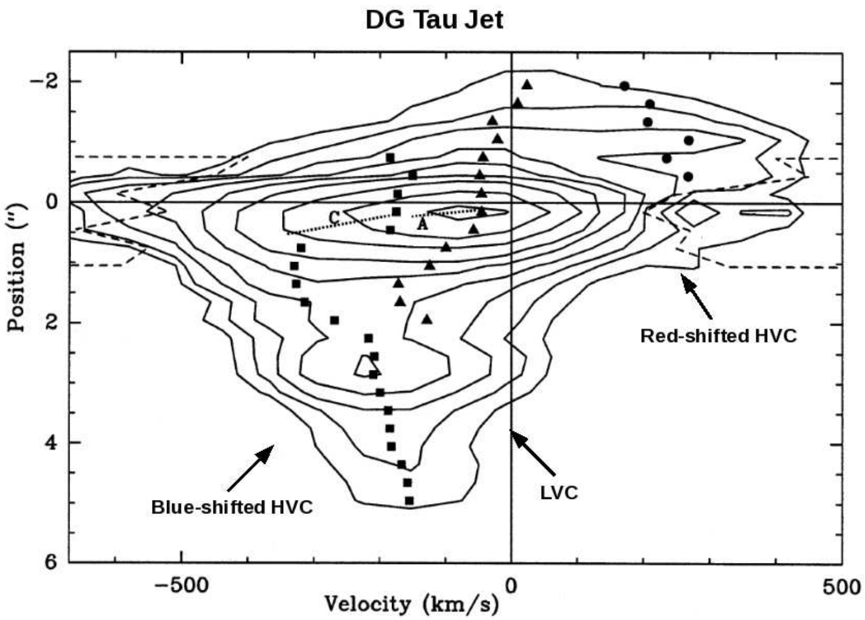

Figure 2.7: Position-velocity diagram of the DG Tau jet, the archetype of CTTS jets. In the x-axis the velocity of the jet is represented while in the y-axis the distance from the exciting source is indicated. In the diagram the intensity contours of the [O I] λ 6300 line are plotted decreasing by a factor of 2 beginning from a 83% of the peak. This jet exhibits typical kinematic features at the base, with a HVC that reaches far distances from the source and a LVC confined very close to the driving source. DG Tau is situated at a distance of ~140 pc, thus 1″ represents ~140 AU. Figure adapted from Lavalley et al. (1997).

by low temperatures ranging from ~500 K to ~3000 K (e.g. Giannini et al. 2004; Caratti o Garatti et al. 2006) and total densities between 10^4-10^6 cm^{-3}. Jets from CTTSs have on average larger temperatures (~10^4-3 10^4 K) and lower total densities (~10^3-10^4 cm^{-3}). Class I jets have usually properties in between these ranges of values. Class I/II jets are partially ionised with low ionisation fractions ranging from 0.03 to 0.06, with higher values near the source. The high degree of ionisation near the source is supposed to be due to some heating mechanism at the jet base, such as ambipolar diffusion or collimating shocks, which are, however, observationally obscured. The electron densities (n_e) have a large range of values ranging from 50 cm^{-3} to 10^4 cm^{-3}. The electron density decreases with the distance from the source, as well as the electron temperature (T_e) with values ranging from 2-3 10^4 K close to the source to 1.0-1.4 10^4 K on larger distances (Fig. 2.6). The amount of mass carried away by protostellar jets can be also observationally derived, combining emission from optically thin lines and kinematics information and varies from ~10^{-8}- 10^{-7} $M_\odot$/yr. In CTTS, the mass ejection fluxes result ~0.05-0.1 times their mass accretion rates as predicted by models (Ferreira et al. 2006).

2.1.3 The inner jet region

In the last years, observations at sub-arcsecond resolution performed in the optical with HST and through Adaptive Optics (AO) techniques have allowed the jet properties close

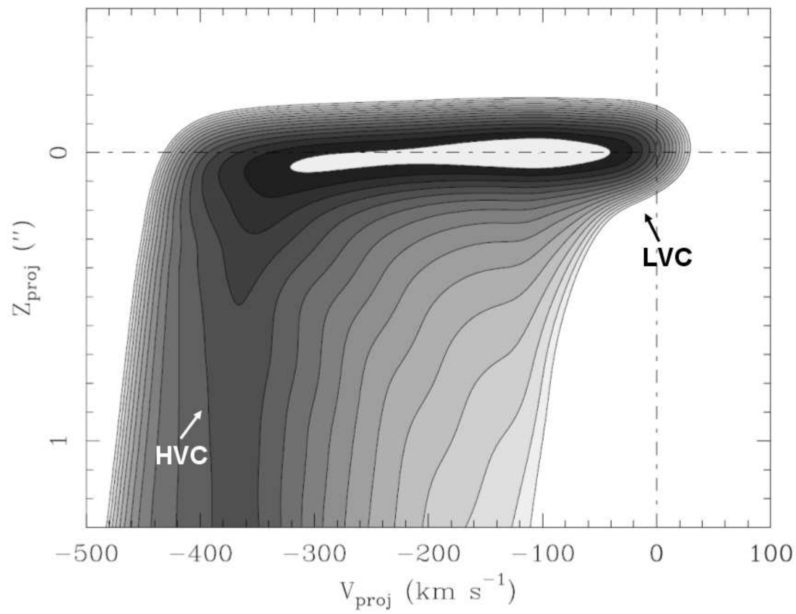

Figure 2.8: [Fe II] 1.644 μm predicted position-velocity diagram from the cold disc-wind model. In the x-axis the velocity of the jet is represented while in the y-axis the distance from the exciting source is indicated. The model reproduces well the presence of an extended HVC and a LVC near the source. Figure adapted from Pesenti et al. (2004).

to the exiting source to be studied in detail. This kind of study is very important to constrain MHD launching models (see Sect. 2.1.1 and Sect. 5.6.1) and probe the excitation conditions at the jet base, where their properties have not yet been modified by the interaction with the surrounding material. Several studies have been done so far regarding the properties near the source of jets from CTTS (see e.g. Lavalley et al. 1997; Dougados et al. 2000; Woitas et al. 2002; Ray et al. 2007). The kinematics of these jets is usually characterised by the presence of two or more velocity components at the jet base (Hartigan et al. 1995). The more collimated and extended velocity component at high-velocity (the so-called high velocity component, HVC) can reach a few hundreds of km s^{-1}, while the lower excited and collimated component (the so-called low-velocity component, LVC) has velocities ranging typically from 10 to 50 km s^{-1}. At an average distance of around 50-80 AU from the source, the low-velocity material gradually disappears, while the axial HVC survives at larger distances (see Fig. 2.7). These kinematical properties have been predicted by both X-wind and disc-wind models. An example of a synthetic position-velocity diagram from the cold disc-wind model of Garcia et al. (2001b) is presented in Fig. 2.8.

On the other hand, the base of jets from embedded Class I sources is less studied, due to the high extinction preventing high angular resolution observations in the optical. Some observational studies of the region within few hundreds of AU from the source have been, however, performed through observations at NIR wavelengths. The first studies of Class I jets close to the source revealed that the forbidden emission lines at the jet

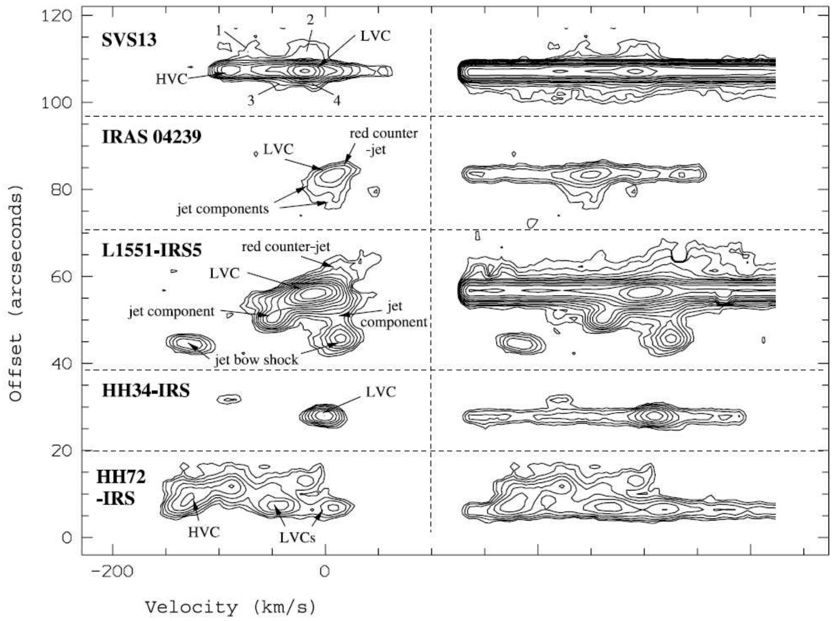

Figure 2.9: Position-velocity diagram of the SVS13, IRAS 04239, L1551, HH34 and HH72 jets near the source through the H_2 2.122 μm emission line. On the left panel the continuum of the driving source has been subtracted leaving only the emission associated with the MHEL regions. The HVC and LVC have been indicated. Figure taken from Davis et al. (2001b).

base (the so-called forbidden emission line (FEL) regions) show a kinematic structure very similar to the one found in CTTS jets (see e.g. Pyo et al. 2002; Davis et al. 2003). This fact indicates that the spread in velocities from a HVC to a LVC is already defined from very early evolutionary stages. It has been found that Class I jets also present a high-velocity H_2 emission close to the driving source (Davis et al. 2001b, 2002). In analogy with FEL regions this molecular component has been named molecular hydrogen emission-line regions (MHEL) (see Fig. 2.9). MHEL regions show, also, a HVC and a LVC with velocities ranging from 50 to 150 km s^{-1} and from 5 to 20 km s^{-1}. FEL and MHEL regions are usually spatially associated. This suggests a common origin for both regions. The [Fe II] emission has, however, higher velocities than the H_2 emission and the ratio between the brightness of the HVC and LVC is also larger for the [Fe II] emission. Recently, MHEL regions have been also detected in association with CTTS jets (Beck et al. 2008). The origin of MHEL is still unclear, some studies propose that the H_2 HVC could be formed along the interaction layer of the jet with the surrounding medium, while the H_2 LVC could be formed from the cool outer regions of a disc-wind.

One of the main aims of this thesis is to probe the kinematics and physical properties at the jet base of Class I objects and compare them with those of CTTS jets (see Sect. 5.6.1). Predictions derived from MHD jet models (see Sect. 5.6.1) will be also tested against observations to see if models developed for more evolved sources can be applied also to younger protostars.

2.2 Accretion properties of YSOs

One fundamental parameter describing the accretion activity of a young star is the mass accretion rate ($\dot{M}_{acc}$). This parameter is, however, very difficult to be determined directly, given that the accretion region is not spatially resolved.

In this section, I will briefly describe the principal methods that are usually adopted to estimate the mass accretion rate and what is so far known about variations of this parameter with the evolution and stellar mass. The accretion properties of CTTS and Class I sources are discussed separately in the following, given the different approaches used for the derivation of $\dot{M}_{acc}$ in the two cases.

2.2.1 Mass accretion in CTTS

The accretion shocks at the protostellar surface release a large amount of energy that is radiated away as a ultraviolet (UV) and optical continuum. Such a continuum is superimposed to the photospheric stellar emission. As a consequence, the photospheric absorption features of the spectra of YSOs appear “veiled”, that is, they are less deep than those of a standard star with the same spectral type. The measure of the veiling of CTT photospheric lines may be used to infer the accretion luminosity (L_{acc}) responsible for the phenomenon: the observed flux of the line is fitted by the scaled and dereddened flux of a standard star with the same spectral type, plus a continuum flux (responsible of the veiling). In this way, we may simultaneously derive the spectrum of the continuum excess and the extinction toward the star. Then, the $\dot{M}_{acc}$ can be inferred, e.g., from eq. 1.9, where the stellar mass and radius are estimated fitting a suitable evolutionary track to the position of the TTauri in the HR diagram. Several authors have used this method to estimate $\dot{M}_{acc}$ in TTauri stars in the Taurus molecular cloud (e.g. Hartigan et al. 1995) finding values ranging from 10^{-7} to $10^{-9}\,M_{\odot}\,yr^{-1}$.

Gullbring et al. (1998) found that the accretion luminosity can be also derived from the UV excess luminosity (L_{UV}). In fact, they found a close correlation between L_{acc} and L_{UV} as can be seen from Fig. 2.10. The $\dot{M}_{acc}$ determined using this method is similar to the one found applying veiling measurements being of the order of $10^{-9}\,M_{\odot}\,yr^{-1}$ for TTauri stars in Taurus (e.g., Hartmann et al. (1998)).

The methods based on optical/UV excess measurements are, however, very sensitive to extinction corrections and cannot be used to estimate $\dot{M}_{acc}$ in highly extincted regions (as e.g. the Ophiuchus molecular cloud), or embedded objects. Muzerolle et al. (1998) showed that the luminosity of the Brγ and Paβ lines from CTTSs correlate with accretion luminosities determined from UV excess measurements. In this way, they derived an empirical relationship between the Brγ and Paβ luminosities and the accretion luminosity (Fig. 2.11). The typical $\dot{M}_{acc}$ values obtained are again of the order of $10^{-8}\,M_{\odot}\,yr^{-1}$. They also tested the method in a sample of extincted Class II sources in ρ Oph finding similar results and confirming the validity of the method.

Measurements of $\dot{M}_{acc}$ for a large number of CTTSs have been done so far (e.g., Muzerolle et al. 2003 and references therein) allowing to find interesting correlations between

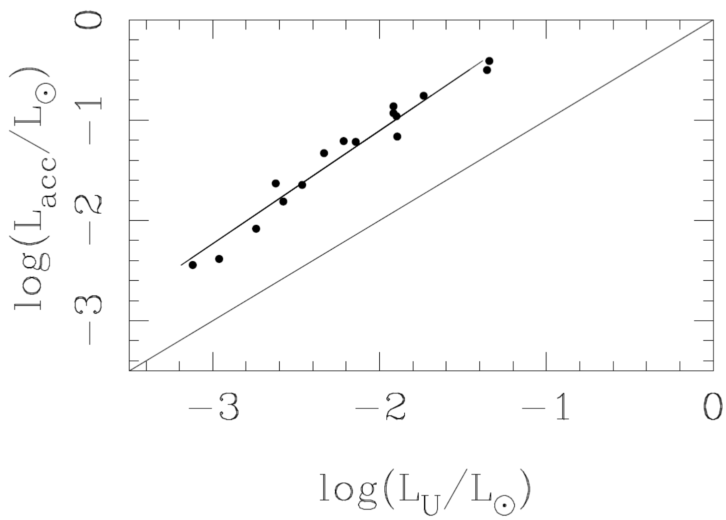

Figure 2.10: Relation between the dereddened UV luminosity and the accretion luminosity for a sample of TTauri stars in the Taurus molecular cloud. Figure taken from Gullbring et al. (1998).

the mass accretion rate and other parameters as the stellar mass and the mass ejection rate ($\dot{M}_{jet}$). Indeed, different studies have shown a tentative correlation between $\dot{M}_{acc}$ and the mass of the central object of the form $\dot{M}_{acc}$~M_*^2 (Fig. 2.12). On the other hand, $\dot{M}_{jet}/\dot{M}_{acc}$ ratios ranging from 0.1 to 0.01 have been found for accreting TTS (Hartigan et al. 1995). The large spread in the $\dot{M}_{jet}/\dot{M}_{acc}$ ratio is mainly due to the uncertainty in determining the $\dot{M}_{jet}$ which can be as large as one order of magnitude. Magnetospheric accretion models (see, Sect. 2.1.1) in which the accretion and ejection phenomena are intimately related predict a relationship between accretion and ejection of around a 10%.

2.2.2 Mass accretion in Class I sources

At variance with CTTS, the mass accretion rate in Class I sources cannot be derived from direct measurements of optical and UV excess due to the high extinction towards these objects. The first estimates of $\dot{M}_{acc}$ in Class I sources came from spherical infall models (e.g., Hartmann 1998) that derived an average accretion rate of 3×10^{-6} M$_\odot$ yr^{-1} assuming that 2×10^5 yr is the time required for a Class I star to acquire the majority of its mass. The same order of magnitude is found from the modelling of the observed SEDs using envelope collapse models and measurements of the envelope masses. These results are around 2 orders of magnitude larger than the values found for CTTSs as it would be expected for younger sources in their main phase of accretion.

White & Hillenbrand (2004) were able to observationally estimate $\dot{M}_{acc}$ in a sample of Class I sources from the analysis of high dispersion optical spectra of light scattered in their large cavities. They surprisingly found an average $\dot{M}_{acc}$ of the order of 10^{-8} M$_\odot$ yr^{-1}, very similar to the one found in CTTS. In addition, the inferred accretion luminosity values were only a 25 % of the total bolometric luminosity, whereas for Class I sources it

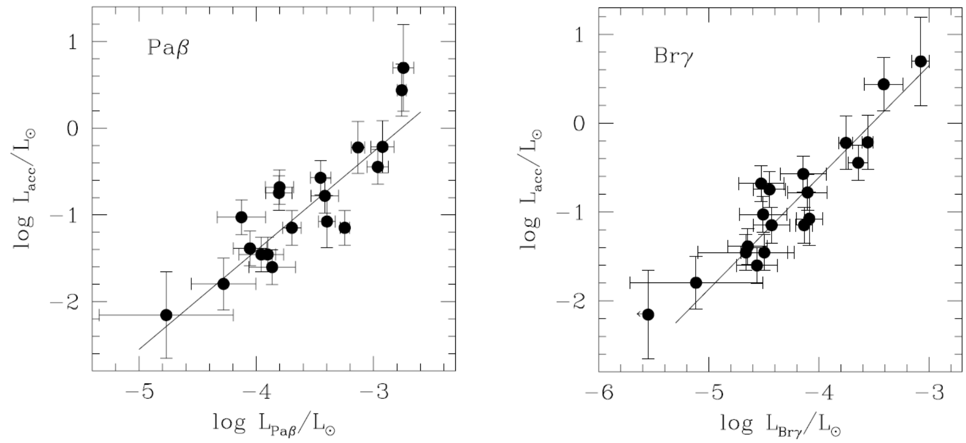

Figure 2.11: Relationships between the accretion luminosity and the luminosity of the Brγ and Paβ lines for a sample of TTS in Taurus. Figure taken from Muzerolle et al. (1998).

should be the main contribution.

Deep IR observations have been able to reveal photospheric absorption features in some Class I sources (Greene & Lada 2002; Nisini et al. 2005a) making possible to determine the IR veiling. Using this method mass accretion rates that in a few cases reach $10^{-6}\,M_{\odot}\,yr^{-1}$ have been found.

Finally, $\dot{M}_{acc}$ can be also derived from the luminosity of the Brγ and Paβ lines if one assumes that the relationships derived by Muzerolle et al. (1998) for CTTS are also valid for Class I sources. This method turns out to be very useful for highly veiled sources where also IR photospheric lines cannot be detected. The accretion rate in a few Class I sources has been measured using this method giving values of around $10^{-8}\,M_{\odot}\,yr^{-1}$, again very similar to the ones found in CTTSs (Muzerolle et al. 1998; Beck et al. 2007). As in the case of White & Hillenbrand (2004) the accretion luminosities found from these studies are very low in comparison with the total bolometric luminosity, with L_{acc}/L_{bol} ratios of 0.2-0.3 or even lower.

The discrepancy between the theoretical accretion rates, and thus accretion luminosities, and the values found from spectroscopic observations of Class I sources was firstly noted by Kenyon et al. (1990). They found that the inferred $\dot{M}_{acc}$ were too low to form a sun mass-like star in a few 10^5 yr, and thus, inconsistent with envelope collapse models. Indeed, if the infalling envelope is accreting efficiently, then the luminosity from mass accretion should dominate the photosphere luminosity. Several hypothesis have been proposed to explain the so-called “luminosity problem”. Some authors suggest that Class I sources are not in their main accretion phase, but instead that the most of their mass have been already accreted during the Class 0 stage (White & Hillenbrand 2004), while others propose that Class I objects accrete through outbursts in their mass accretion (Kenyon et al. 1990; Calvet et al. 2000). Very few studies have been done, however, on the variability of Class I stars and its origin. Beck (2007) found $\dot{M}_{acc}$ variations of some Class I sources in her sample when comparing her results with those of White & Hillenbrand

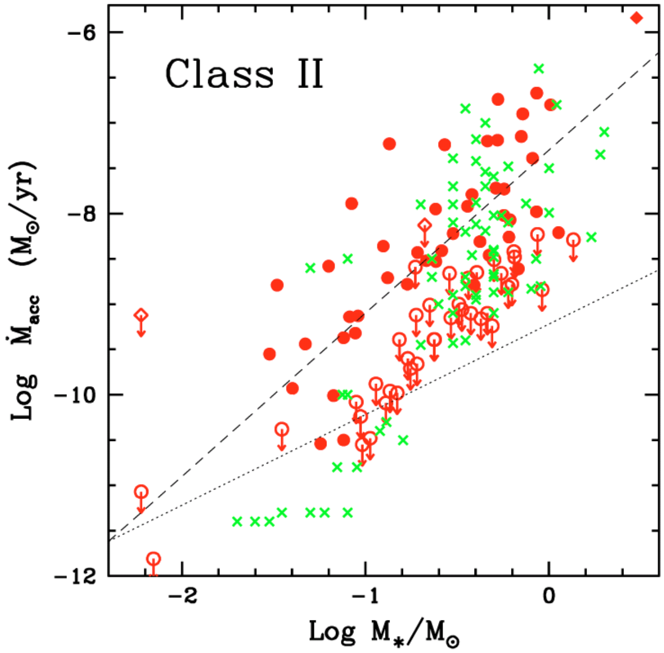

Figure 2.12: Mass accretion rates derived from IR lines as a function of the stellar mass (M_*). Dots and diamonds show $\dot{M}_{acc}$ values derived from the Paβ and Brγ line luminosities. Figure taken from Natta et al. (2006).

(2004) for the same sources. She suggested, however, that such variations are too large to be due to outburst increases in the accretion and that the Muzerolle relation derived for CTTS may not be valid for Class I sources or YSOs observed through scattered light.

Antoniucci et al. (2008) proposed, on the other hand, that an underestimation of the extinction toward the source could be the responsible of the lower accretion luminosities found in Class I sources and, as a consequence, of the inferred low mass accretion rates. In fact, the uncertainties in deriving the accretion luminosity are dominated by the imprecision of the extinction values toward the source. If A_V is underestimated by about 5 or 10 mag then the L_{acc} value (found, e.g. from the reddened fluxes of the Brγ or Paβ lines) is underestimated by a factor 1.9 or 3.7, respectively. In their work, Antoniucci et al. (2008) studied the accretion properties of a few Class I sources and found A_V values much larger than the previous measurements. They used the new A_V values to dereddened the Brγ fluxes and employed the Muzerolle relation to compute the accretion luminosity. They found that L_{acc} in these sources provides around a 50%-80% of the bolometric luminosity, while previously were estimated to be much lower. Studies of larger samples are needed, however, in order to extend these results.

Chapter 3

IR spectral analysis of protostellar jets

Spectral diagnostics is a powerful tool to study the properties of regions excited by shocks and UV photons. Indeed, this technique has been widely used to infer the physical conditions of different astronomical environments, such as planetary nebulae (e.g., Stanghellini et al. 2003), supernova remnants (e.g., Koo et al. 2007), Active Galactic Nuclei (e.g., Sturm et al. 2002) and protostellar jets (e.g., Bacciotti & Eislöffel 1999). Line diagnostic was initially applied to derive electron density (n_e) and electron temperature (T_e) through the ratio of bright optical lines (see e.g., Osterbrock & Ferland 2006). With time, the use of more sensitive instrumentation allowed the detection of fainter lines. This favoured the developing of new diagnostics capabilities that put new constrains on the gas physics (see, e.g., Bacciotti & Eislöffel 1999; Nisini et al. 2002, 2005b; Podio et al. 2006 and references therein).

The spectra of protostellar jets, in particular, are very rich in molecular and atomic emission lines, making these objects ideal candidates to apply spectral diagnostic techniques. The emitting regions in protostellar jets (as knots and bow-shocks) are formed by the interaction of a shock front with the ambient medium. The shock front heats, compresses and ionises the gas, favouring its excitation through collisions. This process leads to radiative emission that helps to cool down the gas. Within the cooling region the physical conditions vary very much giving rise to different ionic and molecular (mostly H_2) lines.

In particular, the IR spectrum of protostellar jets exhibits bright [Fe II] and H_2 transitions allowing to derive important physical parameters of both the atomic and molecular component of the jet (Fig. 3.1). In this chapter, the main diagnostic capabilities of the IR emission lines are briefly described. Although an emphasis on NIR diagnostics through [Fe II] (Sect. 3.2) and H_2 (Sect. 3.3) transitions is done, the basic concepts discussed here can be applied to other species and wavelength ranges.

3.1 Basic concepts and assumptions

Most of the optical and IR lines used for spectral analysis in shocked regions are forbidden emission lines that can be assumed optically thin and collisionally excited. The first of

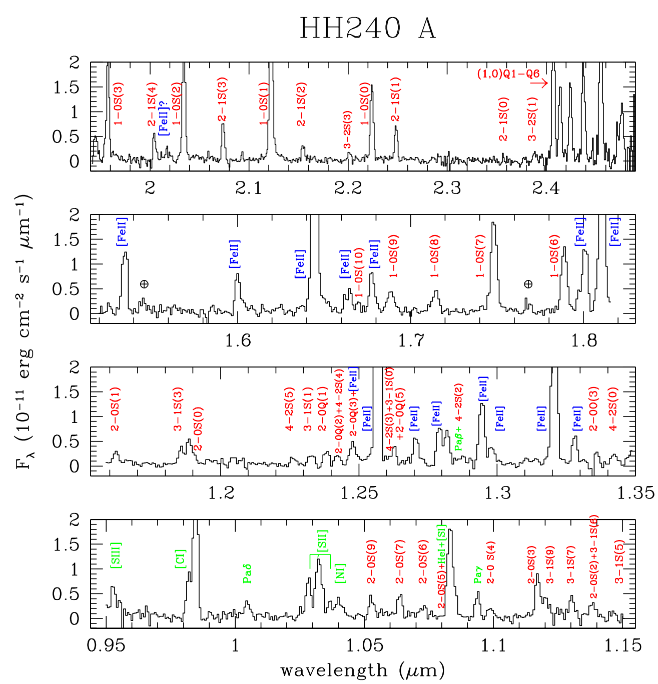

Figure 3.1: Example of a NIR spectrum of the protostellar jet HH240. Several [Fe II] lines involving the first 13 levels of the Fe^{+} and H_2 emission lines are indicated. Figure taken from Nisini et al. (2002).

these assumptions is based on the fact that forbidden lines have small radiative rates, while the second one is associated with the lack of UV photons in the shocked regions of protostellar jets. Following this, the intensity of a line, at frequency ν, connecting two levels j, i (with $E_j > E_i$) can be written as,

$$I_\nu = \int \varepsilon_\nu \, ds \tag{3.1}$$

where ν is the frequency of the line, ε_ν is the volume emission coefficient of the transition and the integration is taken along the line of sight. The volume emission coefficient is defined as the energy per unit of volume, per second, per steradian in the emission line, then,

$$\varepsilon_\nu = \frac{h\nu}{4\pi} n_j \, A_{j,i} \tag{3.2}$$

where $A_{j,i}$ is the Einstein A-coefficient of the transition and n_j is the number density of atoms in the level j. Introducing this expression into eq. 3.1, we have that,

$$I_\nu = \frac{h\nu}{4\pi} A_{j,i} \int f_j \, n \, ds \tag{3.3}$$

Here, $f_j = n_j/n$ is the fractional population of the level j, with n being the total particle density of the emitting species.

The level population can be retrieved from the statistical equilibrium equations. The principal processes involving level population in astrophysical jets are collisional excitation and de-excitation, and radiative decay. Then, the equations of statistical equilibrium can be written as,

$$\sum_{j\neq i} n_j n q_{j,i} + \sum_{j>i} n_j A_{j,i} = \sum_{j\neq i} n_i n q_{i,j} + \sum_{j<i} n_i A_{i,j} \tag{3.4}$$

where $q_{i,j}$ is the collisional transition rate from level i to level j (in units of particles cm^{-3} s^{-1}), and n is the density of the colliding particles, that in ionised environments are mostly n$_e$, while in molecular environments are H_2 particles. Assuming a Maxwellian distribution the collisional rate coefficients can be written as,

$$q_{i,j} = \frac{g_j}{g_i} q_{j,i}\, exp\left(-\frac{h\,\nu_{i,j}}{k\,T_e}\right) = \frac{8.63\times10^{-6}\,\Omega_{i,j}}{g_i\,T_e^{1/2}}\, exp\left(-\frac{h\,\nu_{i,j}}{k\,T_e}\right) \tag{3.5}$$

where g_j and g_i are the degeneracy of the levels j and i, respectively and $\Omega_{i,j}$ represents the collision strengths between the indicated levels. $\Omega_{i,j}$ over a Maxwellian distribution (valid for most of the astrophysical scenarios) are independent on electron density and almost independent on the electron temperature.

Most of the diagnostic analysis involves atoms and molecules with a large number of levels. For each transition the radiative and collisional probabilities must be determined in order to solve the set of equations given by eq. 3.4. Here, to get the general idea of the diagnostic technique, let us assume idealised atoms with only two or three levels.

For the two-level atom, eq. 3.4 leads to one equation. Using eq. 3.5 and denoting as 1 and 2 the upper and lower level, respectively, we obtain,

$$\frac{n_2}{n_1} = \frac{1}{1 + A_{2,1}/n_e\,q_{2,1}} \frac{g_2}{g_1}\, exp\left(-\frac{h\,\nu_{1,2}}{k\,T_e}\right) = b\frac{g_2}{g_1}\, exp\left(-\frac{h\,\nu_{1,2}}{k\,T_e}\right) \tag{3.6}$$

When n$_e$ is high enough that the product n$_e$ $q_{2,1}$ is much larger than $A_{2,1}$, collisional deexcitation dominates over radiative deexcitation. Under this condition the population ratio is determined by collisions and approaches its local thermodynamic equilibrium (LTE) value with $b = 1$. When the product n$_e$ $q_{2,1}$ is much smaller than $A_{2,1}$, collisional deexcitation can be ignored and the population ratio between both levels represents a balance between the collisional excitation and radiative deexcitation, with every collisional excitation producing the emission of a photon. In this case, b is small and proportional to n$_e$. These two "regimes" , determined by a low or high enough value of n$_e$, leads to the definition of a critical density that in a general case can be expressed as,

$$n_c(i) = \sum_{j<i} A_{i,j} / \sum_{j\neq i} q_{i,j} \tag{3.7}$$

In table 3.1, the critical densities for the upper levels of some useful transitions are indicated.

Table 3.1: Critical densities for the upper levels of some forbidden atomic lines.

Species	Upper level	Transition (μm)	n_c[a] (cm^{-3})
FeII	$^4D_{9/2}$	1.644, 1.257	5.6 10^4
FeII	$^4D_{3/2}$	1.600	4.3 10^4
FeII	$^4D_{7/2}$	1.533	4.6 10^4
FeII	$^4P_{5/2}$	0.8617	3.5 10^4
NII	$^1D_2$	0.5754	6.6 10^4
SII	$^2D_{3/2}$	0.6731	2.5 10^4

[a] n_c values calculated for T=10 000 K.

In the case of a three-level atom, the treatment is simplified by neglecting the direct transitions between the two upper levels, labelled as 2 and 3. As a consequence, the ratios b_2/b_1 and b_3/b_1 are each one given by eq. 3.6. The ratio between the intensity of these two lines can be expressed as,

$$\frac{I_{3,1}}{I_{2,1}} = \frac{n_3 A_{3,1} h\nu_{3,1}}{n_2 A_{2,1} h\nu_{2,1}} = \frac{g_3 A_{3,1} \nu_{3,1}}{g_2 A_{2,1} \nu_{2,1}} \left[\frac{1 + A_{2,1}/n_e q_{2,1}}{1 + A_{3,1}/n_e q_{3,1}}\right] e^{-E_{2,3}/kT} \tag{3.8}$$

If the electron density is high, the expression in brackets is equal to unity and, then, the levels are populated according to thermodynamic equilibrium following a Boltzmann statistics. Therefore, the ratio of intensities equals the ratio of the levels population in LTE multiplied by $A_{3,1}\,\nu_{3,1}/A_{2,1}\,\nu_{2,1}$. On the contrary, if n_e is small, the values $A_{j,i}$ are cancelled out in the above equation, and by using eq. 3.5 we see that the line ratio equals $q_{1,3}/q_{1,2}$. In this case, every excitation is followed by the emission of a photon.

3.2 Diagnostics with [Fe II] ratios

Under the physical conditions of molecular clouds, iron is mainly located into dust grains. Because of that, it has a very low gas-phase abundance. However, iron grains are efficiently destroyed by shocks and by photo-evaporation, releasing iron in gas-phase. The low ionisation potential of iron (~7.9 eV) makes it easily ionised and, under the physical conditions of protostellar jets environments (e.g., low ionisation and temperatures ~10 000-20 000 K, see Chap. 2), we can assume that it is single ionised. The electronic configuration of the Fe^+ gives rise to several NIR emission lines very useful to diagnose the jet properties. The brightest lines come from transitions between the ^4D-^4F and ^4D-^6D terms. A diagram of the first Fe^+ energy levels is sketched in Fig. 3.2, where some of the main transitions have been indicated. In this section, I will describe how some useful physical parameters can be derived from ratios and luminosity of suitable [Fe II] emission lines. Although I am focusing this study to the Fe^+ particular case, the same ideas

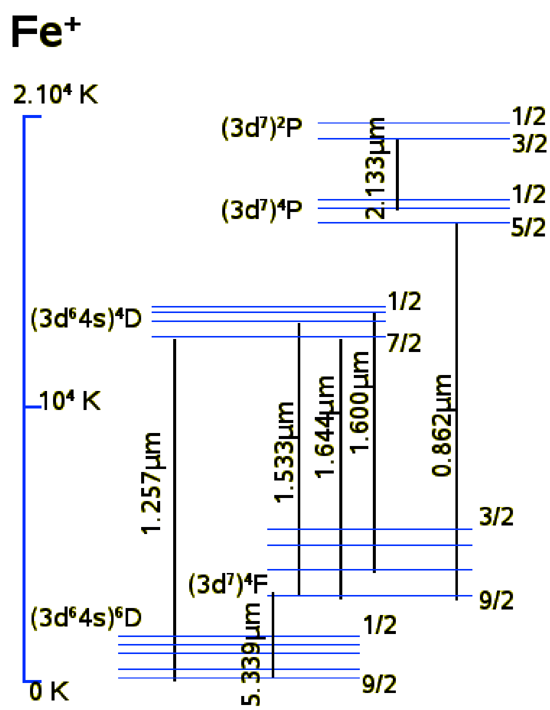

Figure 3.2: Fe^+ energy level diagram of the 16 first levels together with the ($3d^7$) ^{2}P terms. The brightest transitions are indicated.

presented here can be easily applied to other forbidden emission lines (as, e.g., [S II] and [O I]).

Electron density (n_e) and electron temperature (T_e)

As a first example of line diagnostics, we consider the ratio of two lines coming from levels with very similar excitation energies (and thus very similar excitation temperature). An example of this kind of lines are the [Fe II] 1.533 μm and [Fe II] 1.644 μm lines, where both transitions share the same upper-multiplet (see Fig. 3.2).

To simplify, we can consider the transitions as coming from a three-level atom, where the line [Fe II] 1.533 μm represents the transition between levels 3 and 1, and the line [Fe II] 1.644 μm represents the transition between levels 2 and 1. Then from eq. 3.8 and eq. 3.5 at low n_e the line ratio can be approximated as,

$$\frac{I_{1.533}}{I_{1.644}} = \frac{q_{(^4F_{9/2}\rightarrow ^4D_{5/2})}}{q_{(^4F_{9/2}\rightarrow ^4D_{7/2})}} = \frac{\Omega_{(^4F_{9/2}\rightarrow ^4D_{5/2})}}{\Omega_{(^4F_{9/2}\rightarrow ^4D_{7/2})}} \tag{3.9}$$

Therefore the ratio of lines with very close energy levels equals the ratio of the collision strengths of the transitions, since the term $e^{-E_{2,3}}/kT$ can be cancelled out. The collision strengths are independent of n_e and also highly independent of the electron temperature (T_e), thus this ratio is a fixed number for low n_e.

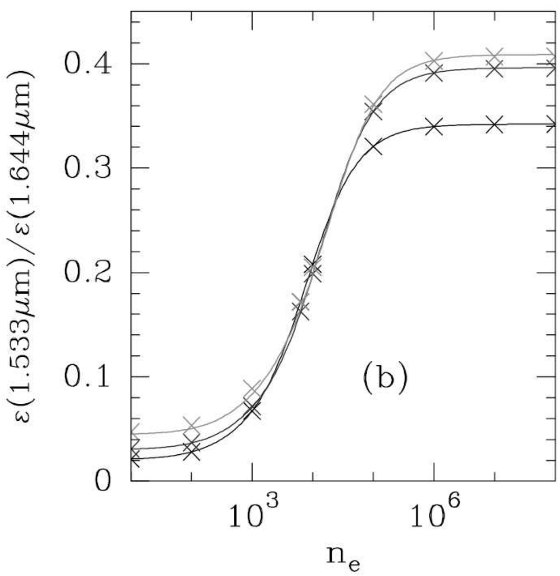

Figure 3.3: Theoretical ratio of the [Fe II] 1.533 and [Fe II] 1.644 μm lines calculated for different electron temperatures (3 000,10 000, 20 000 K). Electron temperature increases from bottom to top. These transitions come from energy levels with similar excitation energies thus their ratio is independent of electron temperature and then, very sensitive of electron density. Figure taken from Pesenti et al. (2003).

At variance with the low density case, at high n_e the ratio $I_{1.533}/I_{1.644}$ following eq. 3.8 and eq, 3.5 equals,

$$\frac{I_{1.533}}{I_{1.644}} = \frac{q_{(^4F_{9/2}\rightarrow ^4D_{5/2})}}{q_{(^4F_{9/2}\rightarrow ^4D_{7/2})}} \times \frac{A_{1.644}}{A_{1.533}} \tag{3.10}$$

Then, the ratio of two lines from very close upper-states changes from a minimum at low n_e (low density regime, LDR) to a maximum at high n_e (high density regime, HDR). This means that, while we are in between the LDR and the HDR, this ratio is a good indicator of the electron density and almost independent of T_e (see Fig. 3.3). Examples of other suitable line ratios to derive electron density are the [Fe II] 1.600/1.644 μm and the [Fe II] 1.677/1.644 μm.

On the other hand, the electron temperature can be derived using the ratio of lines with very different excitation temperatures. For example, one can combine lines coming from the ^{4}P terms with those coming from the ^{4}D terms. In this case, the lines come from levels with very different electron temperatures but quite similar critical densities, thus, their ratio is very sensitive to T_e. Examples of this kind of ratios are the [Fe II] 2.133/1.644 μm and the [Fe II] 0.8617/1.644 μm (Fig. 3.4).

Again, let us assume the different transitions as coming from a three-level atom where, e.g., the [Fe II] 0.8617 μm line represents a hypothetical transition between levels 3 to 1 and the [Fe II] 1.644 μm line represents a transition between levels 2 and 1. This time, the ratio between the lines is, however, more complex than the one expressed by eq. 3.8 since transitions between levels 2 and 3 must be taken into account. To derive a simple result, let us assume that in the LDR every upward collisional excitation is followed by

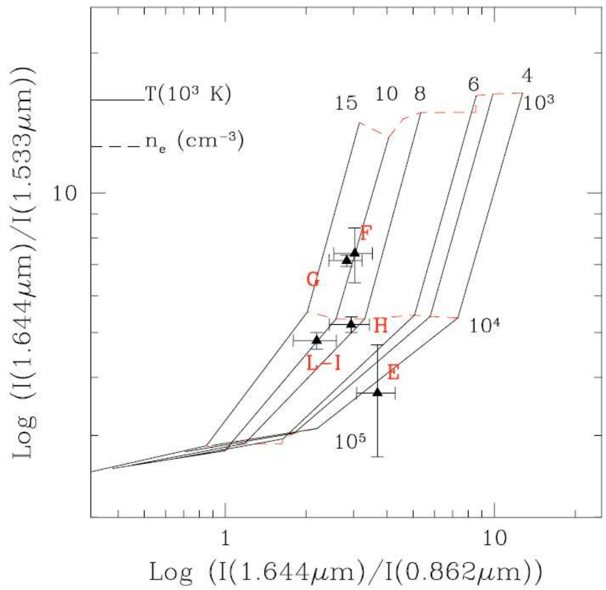

Figure 3.4: Diagnostic diagram based on [Fe II] lines. On the x-axis the [Fe II] 1.644/0.862μm line ratio (sensitive to T_e) is represent, while in the y-axis the [Fe II] 1.644/1.533μm line ratio (sensitive to n_e is plotted. Dashed and solid lines indicates n_e and T_e values of 10^3, 10^4 and 10^5 cm^{-3} and 4, 5, 6, 8, 10, $15{\times}10^3$ K. Figure taken from Nisini et al. (2005b).

a downward radiative transition and that $q_{1,3}/q_{1,2} \ll 1$. Therefore, we are ignoring the population of level 2 produced by radiative transition from level 3. Then using eq. 3.8 and eq. 3.5 we find that,

$$I_{0.862}/I_{1.644} = \frac{q_{(^4F_{9/2}\rightarrow ^4P_{5/2})}}{q_{(^4F_{9/2}\rightarrow ^4D_{7/2})}} = \frac{\Omega_{(^4F_{9/2}\rightarrow ^4P_{5/2})}}{\Omega_{(^4F_{9/2}\rightarrow ^4D_{7/2})}}\, exp\,((E_{^4D_{7/2}} - E_{^4P_{5/2}})/kT_e) \qquad (3.11)$$

where E represents the energy of the upper level of each transition and T_e indicates the electron temperature.

In the HDR, the line ratio can be written following eq. 3.8 and eq. 3.5 as,

$$I_{0.862}/I_{1.644} = \frac{q_{(^4F_{9/2}\rightarrow ^4P_{5/2})}}{q_{(^4F_{9/2}\rightarrow ^4D_{7/2})}}\frac{A_{0.862}}{A_{1.644}} = \frac{\Omega_{(^4F_{9/2}\rightarrow ^4P_{5/2})}}{\Omega_{(^4F_{9/2}\rightarrow ^4D_{7/2})}}\frac{A_{1.644}}{A_{0.862}}\, exp\,((E_{^4D_{7/2}} - E_{^4P_{5/2}})/kT_e) \quad (3.12)$$

Thus, the ratio $I_{0.862}/I_{1.644}$ change from a minimum at LDR to a maximum at HDR, while in between both values the ratio varies as a function of T_e independently of the n_e value.

Unfortunately, lines coming from the ^{4}P term usually lay in poor atmospheric transition regions or in the optical regime forcing an optical/IR study of the jet (Nisini et al. 2005b; Podio et al. 2006). In addition, several of these lines have unknown Einstein coefficients (as the case of the [Fe II] 2.133$\,\mu$m line, usually detected at the jet base), thus, making impossible their use.

Table 3.2: Radiative transition probabilities for [Fe II] lines taken from different authors.

Line id.	λ	$A_{j,i}$ (Q-SST)[a]	(Q-HFR)[a]	(NSS)[b]	(SH)[c]
[Fe II] $a^4D_{7/2}$-$a^4F_{9/2}$	1.644	5.98	5.73	4.65	4.26
[Fe II] $a^4D_{7/2}$-$a^6D_{7/2}$	1.321	1.31	1.44	1.33	1.35
[Fe II] $a^4D_{7/2}$-$a^6D_{9/2}$	1.257	4.74	5.18	4.83	4.83

Note: Air wavelengths in microns. $A_{j,i}$ values expressed in 10^{-3} s^{-1}
[a]Quinet et al. (1996)
[b]Nussbaumer & Storey (1988)
[c]Smith & Hartigan (2006)

Visual extinction

Another useful parameter that can be derived from the analysis of [Fe II] lines is the visual extinction (A_v). This can be inferred from the ratio of two lines coming from the same upper level. In this case, following eq. 3.3 the line ratio can be written as,

$$\frac{I_2}{I_1} = \frac{A_2\,\nu_2}{A_1\,\nu_1} = \frac{A_2\,\lambda_1}{A_1\,\lambda_2}\,10^{-E(\lambda_2-\lambda_1)/2.5} \tag{3.13}$$

where $E(\lambda_2 - \lambda_1)$ is the color excess between the two line wavelengths. Therefore, the ratio of lines coming from the same upper level is independent on the plasma conditions and only depends on the frequency and transition probability of the transitions. From $E(\lambda_2 - \lambda_1)$, A_v can be easily retrieved applying an extinction law. [Fe II] has several IR transitions that originate from the same upper level. The brightest ratios that are widely used are the [Fe II] 1.257/1.644 μm and the [Fe II] 1.322/1.644 μm line ratio. The determination of A_v using these lines is affected, however, by uncertainties rising mostly from the uncertain on the A-Einstein coefficients. In fact, different studies report different radiative transition probabilities for the same line. In table 3.2, an list of A-coefficients derived by different authors for the lines of interest is shown. The extinction derived using the transition probabilities of Nussbaumer & Storey (1988) is, usually, higher than the one derived using the Quinet et al. (1996) one. In addition, it has been noted that even using the same coefficients, different ratios report different extinction values. Indeed, the [Fe II] 1.257/1.644 μm line ratio gives higher extinction values (around a factor of two) with respect to the one obtained from the [Fe II] 1.321/1.644 μm line ratio using the same transition probability (Nisini et al. 2005b; Giannini et al. 2008).

The ratio of lines with the same upper level can be in principle used to experimentally determine the radiative transition probabilities if the extinction is previously known. Smith & Hartigan (2006) have applied this method to empirically derive the transition probabilities of several [Fe II] lines from a spectrum of P Cygni (some of the derived values are reported in the last column of Table 3.2). The experimental values are different to the ones theoretically calculated, but very similar to the ones derived from Nussbaumer

& Storey (1988).

Iron abundance

From the [Fe II] lines it is also possible to probe the degree of grain destruction in jets. In fact, comparing the absolute gas-phase iron abundance in the region of study with the solar iron abundance, one can infer the percentage of iron still located in grains. This is done by comparing the emission of [Fe II] with the one of a non-refractory species of known abundance. A very suitable ratio is the one between the [Fe II] 1.257 μm line and the [P II] 1.188 μm line (Oliva et al. 2001). These two lines are very close in wavelength and thus, their ratio is poorly affected by extinction. In addition, both lines are excited under similar conditions and can be assumed in the first ionised state at similar percentage. Assuming a solar abundance for both elements, the ratio between both lines is [Fe II] / [P II]~1/2 [Fe / P]~56. Then, any measured shift to this value indicates that some of the iron is located in grains. There are several evidences of iron located in grains along protostellar jets. This fact may suggest the presence of robust dust grains that need fast shocks to be destroyed (Nisini et al. 2005b; Podio et al. 2006).

3.3 Diagnostics with H_2 lines

H_2 is the most abundant molecule in molecular clouds. It is, however, very difficult to excite, as previously mentioned in Chap. 1.1. Nevertheless, it is well observed in photodissociation regions (PDR, where it is radiatively excited) and shocks (where it is mainly collisionally excited) giving us information about the physical properties of the medium. In the case of protostellar jets, the main H_2 excitation process is the collision with other H_2 molecules or neutral H.

The molecular hydrogen can be found in two different states, the ortho-H_2 (with parallel proton spins) and the para-H_2 (with antiparallel proton spins). An isolated H_2 molecule cannot change from ortho to para state, since radiative decay between the two nuclear spins state is not allowed. However, the change of state can take place by H_2 collisions with H^0, H^+ and H_3^+. H_2 is mainly formed on dust surfaces. The formation of H_2 by the radiative association of two H atoms is not possible under jets conditions due to the high densities required for the process to occur ($n \geq 10^{12}$ cm^{-3}).

Since H_2 is a homonuclear molecule, only rovibrational quadrupolar transitions are allowed. The selection rules of the transitions are $\Delta J = \pm 2, 0$ and $\Delta v = 0, \pm n$, with v and J being the vibrational and rotational quantum numbers. Typical Einstein A-coefficients for ro-vibrational transitions with the ground level are A$\sim 10^{-6}$-10^{-7} s^{-1}, while typical collision rate coefficients for collisions with other H_2 molecules are $\sim 10^{-12}$-10^{-11} cm^3 s^{-1}. Thus, the critical densities of H_2 are in the range of $\sim 10^3$-10^5 cm^{-3}. This means that in the dense environments typical of star forming regions, the H_2 lines easily reach the LTE conditions. The lowest energy quadrupolar transition is the 0-0 S(0)[1] at 28.2 μm , thus, not

[1]Spectroscopic notation: the first two numbers indicates the change in v. The letter represents the branch

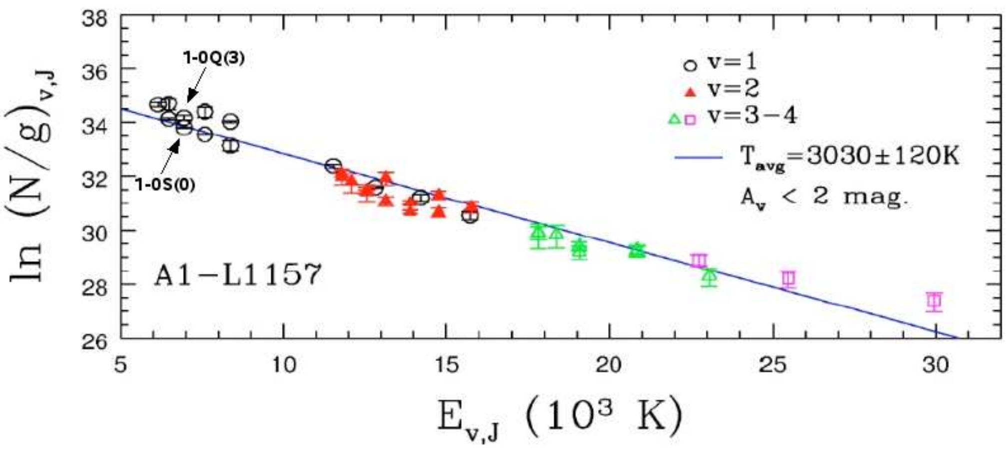

Figure 3.5: Example of a Boltzmann diagram. When the gas is isothermal the value of $ln(N(v, J)/g_{v,J})$ for each line falls in a straight line which slope indicates the T_{ex}^{-1} value. Different symbols represent lines coming from different vibrational levels. The 1-0S(1) and 1-0Q(3) lines have the same $E(v, J)$ value, thus they can be used to estimate the visual extinction (see text). Figure adapted from Caratti o Garatti et al. (2006).

observed from the ground. The v=1-4 vibrational levels have, however, several transitions falling in the NIR range of the spectrum. Lines from the v=1 trace temperatures around 2 000 K. One of the brightest lines is the 1-0S(1) at 2.122 μm. This line is widely used to trace the molecular component of protostellar jets (Eislöffel et al. 2000; Giannini et al. 2004; Caratti o Garatti et al. 2006). Temperatures higher than 2000 K can be traced using lines coming from higher vibrational levels. In the NIR, lines coming from levels as high a v=5 have been detected in several protostellar jets (Caratti o Garatti et al. 2006; Giannini et al. 2008) tracing gas temperatures up to ~5 000 K.

In the assumption of LTE emission, the H_2 line fluxes can be used to derive some important physical parameters as the temperature, H_2 column density and visual extinction, through the construction of the so-called Boltzmann excitation diagrams[2].

The column density of a given level ($N(v, J)$) with respect to the total H_2 column density ($N(H_2)$) can be written, assuming a thermal distribution, as,

$$\frac{N(v, J)}{N(H_2)} = \frac{g_{v,J}}{Q} exp(-E(v, J)/kT_{ex}) \tag{3.14}$$

$$Q = \sum_i g_i \, e^{-E_i/KT} \tag{3.15}$$

where Q and $g_{v,J}$ represent the partition function and the statistical weight[3]. Following

transition (J_{up}-J_{low}), that could be equal to S, Q and O corresponding to ΔJ=+2, ΔJ=0 and ΔJ=-2. Finally, the number inside the parenthesis indicate the rotational number of the lower factor.

[2]Boltzmann diagrams can be also named in literature as rovibrational diagrams or excitation diagrams.

[3]The statistical weight is the product of the nuclear spin statistical weight and the rotational statistical weight. In equilibrium, this product is equal to 3(2J+1) and (2J+1) in the case of ortho-H_2 and para-H_2, respectively. Thus, from a statistical point of view, for a fixed temperature, one would expect around three times more ortho-H_2 than para-H_2.

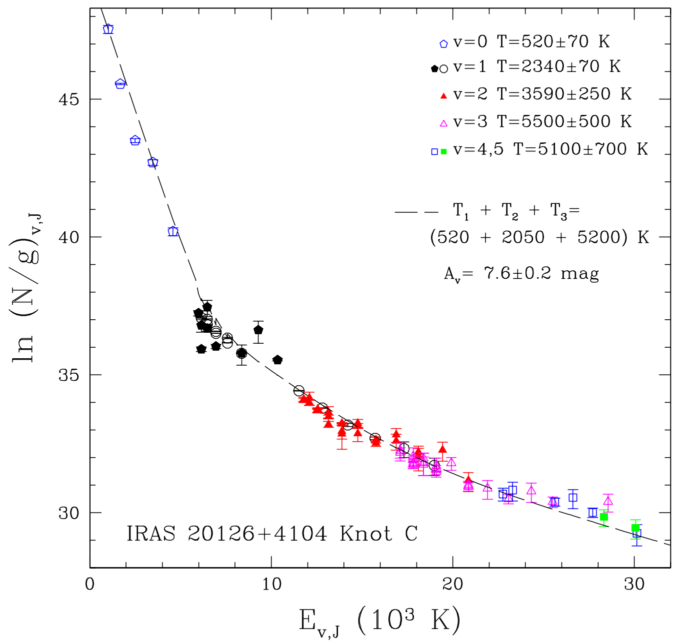

Figure 3.6: Example of a Boltzmann diagram for a thermalised gas. Different symbols indicate lines coming from different vibrational levels. In this case, the value of $ln(N(v, J)/g_{v,J})$ for each line follow a curve. The dashed line represents the theoretical population distribution of a gas at three different temperatures: 520, 2050 and 5200 K. Figure taken from Caratti o Garatti et al. (2008).

eq. 3.3, the column densities $N(v, J)$ can be derived from the observed line intensities $I(v, J)$ through the expression,

$$I_{v,J} = \frac{h\nu}{4\pi} A_{v,J}\, N(v, J) \tag{3.16}$$

From eqs. 3.14 and 3.16, it is easy to derive,

$$ln\frac{N(v, J)}{g_{v,J}} = ln\left(\frac{4\pi}{h\nu}\frac{I_{v,J}}{g_{v,J}A_{v,J}}\right) = -\frac{E(v, J)}{kT_{ex}} + ln\frac{N(H_2)}{Q} \tag{3.17}$$

This expression indicates that for a isothermal gas, the plot of $ln(N(v, J)/g_{v,J})$ versus $E(v, J)$ is a straight line (Fig. 3.5). In addition, the slope of the line is equal to the inverse of the gas temperature, T_{ex}^{-1}. From this kind of plot, it is also very easy to derive the visual extinction. In fact, two lines with the same excitation energy have the same value of $N(v, J)/g_{v,J}$ and thus should be placed at the same point in the diagram. If a shift between them is found, then, the flux of each line can be corrected applying different A_v values till they match the same position in the diagram. Examples of the most used couples of lines are the 1-0S(1)-1-0Q(3) lines (indicated in Fig. 3.5) and the 1-0S(2)-1-0Q(4) lines. However, the Q lines at ~2.3 μm fall in a poor atmospheric transmision region (more details about the atmospheric transmision in the NIR can be found in Sect. 4.1 and Fig. 4.2.), thus, their fluxes are usually affected by huge uncertainties. In addition,

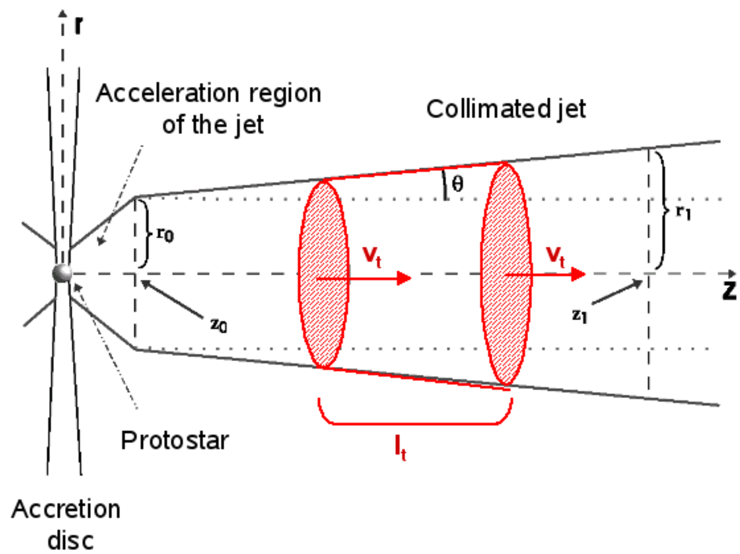

Figure 3.7: Sketch of a protostellar jet where the velocity (v_t) and length (l_t) of a section of the jet perpendicular to the line of sight is represented.

the 1-0S(i) and 1-0Q(i) lines are placed quite near in wavelength and thus, they are not sensible enough to extinction variations. The extinction derived from these lines should be considered then only as an approximate value.

Finally, the total column density, $N(H_2)$, can be easily derived from the interception to zero of the line fitted to the transitions.

We have to take in mind, however, that a straight line can be only fitted if the gas is thermalised to a single temperature. This is not the case, e.g. in a not resolved post-shocked region where the temperature decreases from a high value at the shock front to roughly the ambient medium. In this case, the position of the lines in the diagram is going to follow a curve where different vibrational levels are characterised by a different temperature (Fig. 3.6), indicating a temperature stratification.

3.4 Mass loss rates

The mass loss rate (or mass flux rate, $\dot{M}_{jet}$) is a very important parameter since regulates the dynamics of protostellar jets. The comparison between $\dot{M}_{jet}$ and $\dot{M}_{acc}$ helps to constrain MHD models that predict ejection/accretion rate ratios of ~0.1-0.01 and can be used to study the evolution of the accretion/ejection phenomenon from early protostars to CTTS (Hartigan et al. 1995; White & Hillenbrand 2004; Antoniucci et al. 2008).

For a full account of the different methods to derive $\dot{M}_{jet}$ from emission lines see e.g. Dougados (2009). Here, only a description of how to derive $\dot{M}_{jet}$ from the luminosity of forbidden emission lines and from the total column density of the H_2 is done since these are the methods used in this thesis.

$\dot{M}_{jet}$ derived from the luminosity of forbidden emission lines

From the luminosity of the forbidden atomic emission lines, it is possible to derive the mass loss rate for the atomic component of the jet ($\dot{M}_{jet}$). These lines are optically thin and thus their luminosities are proportional to the mass of the emitting gas (Hartigan et al. 1994). A very intuitive way to define the mass loss rate is from the expression,

$$\dot{M}_{jet} = M\, v_t \,/\, l_t \tag{3.18}$$

where v_t and l_t is the velocity and length of the selected area, for which $\dot{M}_{jet}$ is going to be calculated, projected perpendicular to the line of sight (see, Fig. 3.7) and M is the total mass of the jet section. The velocity v_t can be derived from the study of the proper motions of the jet or from the radial velocities if the inclination angle of the jet with respect to the plane of the sky is known. On the other hand, the total mass, M, can be written as, $M = \mu\, m_H\, \eta_{tot}$. In this last expression, η_{tot} represents the total number of atoms within the selected aperture and can be written as $\eta_{tot} = n_H V$ where V is the emitting volume and n_H is the particle density. Then, the mass loss rate is,

$$\dot{M}_j = \mu\, m_H\, (n_H V)\, dv_t/dl_t \tag{3.19}$$

The product $(n_H V)$ can be written as,

$$n_H V = n_H\, L(line)\, \epsilon_\nu^{-1} = L(line) \left(h\nu\, A_i\, f_i\, \frac{X_i}{X}\, \frac{[X]}{[H]} \right)^{-1} \tag{3.20}$$

In this expression, L(line) is the line luminosity, X_i/X is the ionisation fraction of the species X, while $[X]/[H]$ represents the total abundance of the species X with respect to hydrogen.

$\dot{M}_{jet}$ derived from the H_2 emission line fluxes

The mass loss rate transported by the molecular component ($\dot{M}_{H_2}$) can be also derived from eq. 3.18. This time the total mass equals, $M = \mu\, m_H\, \eta_{tot}$, where η_{tot} can be written as,

$$\eta_{tot} = n_H\, V = 2N(H_2)\, A \tag{3.21}$$

where A is the cross-sectional area of the jet (see, Fig. 3.7) and $N(H_2)$ is the H_2 column density derived from the Boltzmann diagram (see sect. 3.3). Therefore, the expression for $\dot{M}_{H_2}$ can be written as,

$$\dot{M}_{H_2} = 2\,\mu\, m_H\, N(H_2)\, A\, dv_t\,/dl_t \tag{3.22}$$

The $\dot{M}_{H_2}$ value found using this method is a good estimation only if the gas is isothermal. When the transitions in the Boltzmann diagram cannot be fitted by a single straight line (that is, when a temperature stratification is present), then, the $\dot{M}_{H_2}$ value is just a lower limit.
The $\dot{M}_{jet}$ values derived from eqs. 3.19 and 3.22 are affected by several uncertainties

mainly concerning the errors on the extinction and distance of the jet, that affect the line luminosities. In addition, the derived $\dot{M}_{jet}$ could be either an upper limit (if there is entrainment material from the molecular cloud into the jet beam) or a lower limit (if, e.g., some of the material of the jet is too cool to emit.).

It is interesting to compare the mass flux rate estimates for the same jet done by means of different tracers. This has been done by, e.g., Podio et al. (2006) who show that the mass flux derived directly from [Fe II] line luminosity, using the measured tangential velocity, is always equal of larger than the $\dot{M}_{jet}$ value derived from the luminosity of other optical atomic tracers, such as [S II] and [O I], in spite of the possibility that part of the iron is still locked on dust grains. This is probably due to the fact that [Fe II] traces a larger fraction of the total flowing mass than the optical lines, as discussed in Nisini et al. (2005b). At the same time, it was found that in these jets the mass flux traced by the H_2 molecular component is negligible with respect to the mass flux due to the atomic component.

Chapter 4

Observations

In this thesis, NIR observations taken with ISAAC at VLT of two different set of objects are presented. The first sample includes several Class 0/I jets located in the Orion molecular cloud and in the Gum Nebula. This sample has been chosen in order to study the jets of embedded sources and probe their physical properties as close to the central source as possible. The second set of objects consists of ten Class I sources from the ρ Oph molecular cloud. They have been observed in order to study the accretion properties of poor evolved objects and compare the results with those of more evolved CTTS.

This Chapter begins with a brief introduction on the advantages and limitations of NIR observations (Sect. 4.1) with respect to optical ones. A list of the objects and the main selection criteria for the samples are reported in Sect. 4.2. NIR observations requires specific acquisition techniques and a careful reduction and calibration. The basic of these techniques and a description of the specific observations and main instrument setup are reported in Sect. 4.3.

4.1 Advantages and limitations of NIR observations

The first observations of protostellar jets through NIR wavelengths date from the 80's decade. They mainly consisted in extensive surveys of Herbig-Haro objects through the H_2 2.12 μm line (e.g., Bally & Lane 1982; Reipurth & Wamsteker 1983; Zinnecker et al. 1989). The development of much more sensitive IR detectors and the increase in dimensions and resolution of the arrays have led to a huge progress in IR observations. A combination of ground and aircraft observations allowed a better interpretation of the physics of protostellar jets and the development of more sophisticated models to explain these properties. These progresses are expected to be further improved by the recent developments in higher angular resolution instrumentation at IR wavelengths, as adaptive optics and interferometry techniques.

NIR observations present important advantages, but also several limitations that should be considered. One of the most immediate advantage is the limited extinction present at NIR wavelengths, with respect to the optical and UV ranges. Indeed, the extinction in the K-band is ten times smaller than at optical wavelengths. This makes NIR a very useful

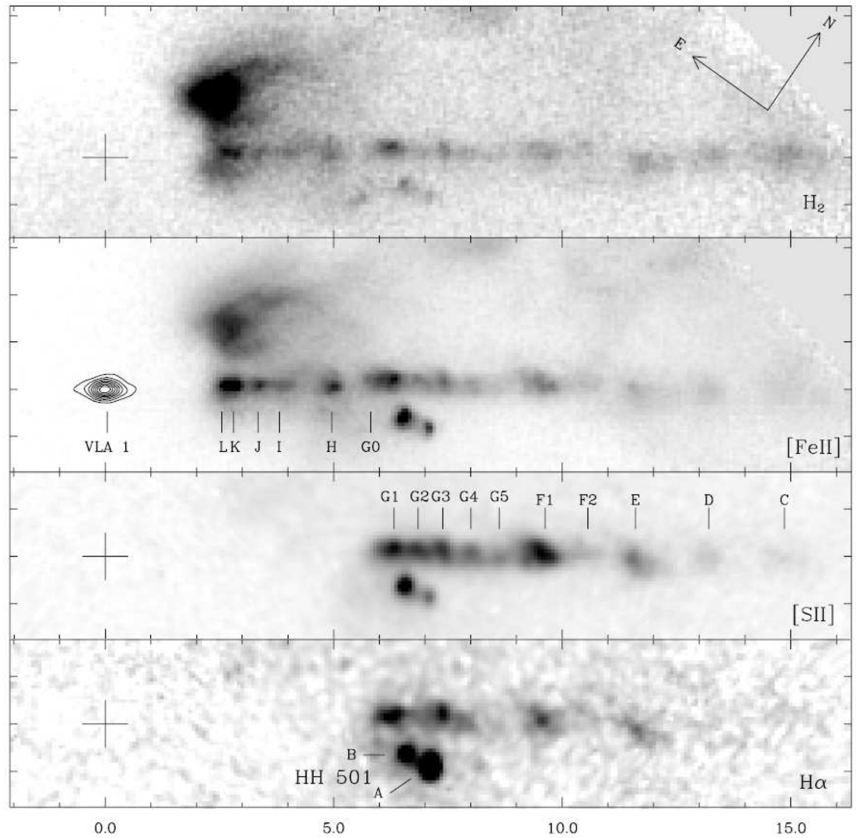

Figure 4.1: Image of the HH1 jet taken by HST at four different wavelengths: NIR images in [Fe II] 1.644μm and H_2 2.122μm lines, and optical images in [S II] 0.6717/0.6731μm and H_α lines. HH1 is a Class 0 protostellar jet, thus, a very embedded object. The position of the source, VLA1 (only detected at radio wavelengths), is indicated for all the panels. In the x- and y-axis the distance from the source is represented in arcseconds. The NIR lines trace regions closer to the driven source (down to ∼2″) with respect to the optical ones that only trace gas down to ∼6″ from the source. Figure taken from Reipurth et al. (2000a).

tool to study the inner regions of protostellar jets, especially in embedded sources such as the Class 0/I (Fig. 4.1).

Several atoms and molecules have a very rich NIR spectrum. Ions as [Fe II] , [P II] and [S II] show several transitions falling in the NIR, allowing to trace different physical conditions of jets (see Chap. 3 for more details). Moreover, gas with temperatures lower than 5 000 K and densities larger than 10^4 cm^{-3} only cool down through NIR atomic and molecular lines. Thus, NIR studies of protostellar jets are indispensable to understand the properties of young jets propagating in a dense environment. In contrast, NIR observations also present several limitations. First of all, the atmosphere emits also at NIR masking part of the signal from the object. Thus, a very accurate subtractions of the background emission is needed. The OH lines are the main sky emission below 2.2 μm. They are very bright lines whose fluxes varies both spatially and temporarily. Another problem comes from the atmospheric transmission (Fig. 4.2). At NIR wavelengths, only few atmo-

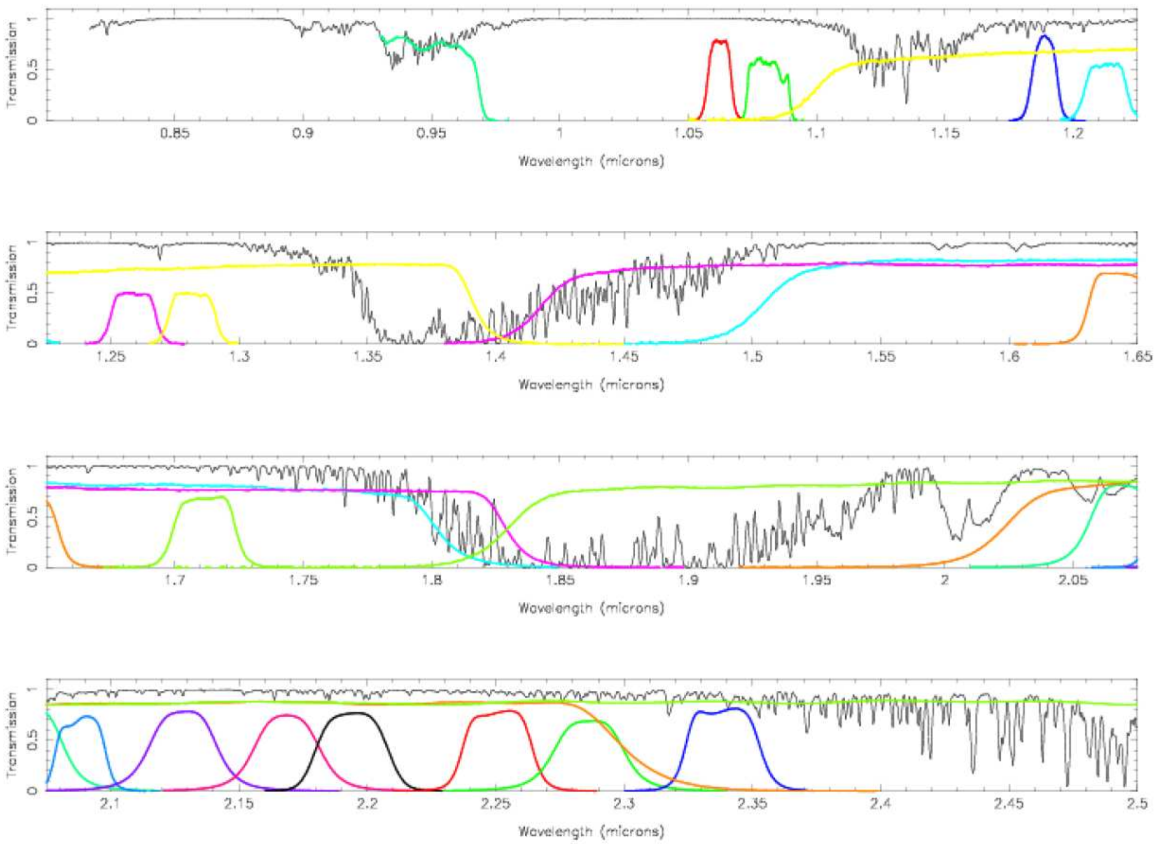

Figure 4.2: Model of the atmospheric transmission spectra of the J, H and K band for Paranal. The response curve of the narrow band filters available at ISAAC are also plotted. In green is represented part of the Z filter and in yellow the J filter. The SH and H filters are indicated in magenta and blue, respectively, while, green and orange represent the SK and Ks filters.

spheric "windows" are accessible from ground, corresponding to the wavelength bands J, H and K between 1 and 2.4 μm. At longer wavelengths the transmission decreases till ~50% at 20 μm while above this limit only satellite or balloon observations are possible.

In addition to the atmospheric limitations, the main limitation on the spatial resolution that can be reached in the IR come from diffraction. The diffraction disc corresponds to an angular diameter of,

$$\theta'' = \frac{1}{2}\frac{\lambda_{\mu m}}{D_m} \tag{4.1}$$

where $\lambda_{\mu m}$ is the wavelength in μm and D is the diameter of the telescope in meters. Assuming a 8-m telescope at a wavelength of 2 μm, the angular diameter of the diffraction disc is roughly 0.12″. On the other hand, the diffraction disc at 0.6 μm equals ~0.04″. Thus, the angular resolution that can be reached with diffraction limited instruments is always smaller at IR wavelengths than at optical ones. The angular resolution of IR instruments can be, however, improved through Adaptive Optics (AO) systems[1]. The

[1]Details on AO systems can be found on Esposito & Pinna (2008)

Table 4.1: The observed sample: HH objects

HH object	Source	α(2000.0) (^{h} ^{m} ^{s})	δ(2000.0) ($^\circ$ $'$ $''$)	Class	D (pc)
HH 34	HH34-IRS	05 35 31.0	-06 28 36	I	450
HH 46-47	HH46-IRS	08 25 44.8	-51 03 27	I	450
HH 111	IRAS05491+0247	05 51 44.2	+02 48 34	0	450
HH 212	HH212-MM	05 43 51.5	-01 02 52	0	400
HH1	VLA1	05 36 20.8	-06 45 13	0	460

size of a seeing disc can be expressed as λ/r_0, being $r_0 \propto \lambda^{6/5}$ the Fried parameter that represents the length over which the incoming wavefront is not perturbed by motions in the atmosphere. The seeing at 2 μm under good atmospheric conditions is around 0.4-0.5″. Thus, the resolution of a 8 m diffraction limited telescope is a factor 4 better than a seeing limited instrument.

4.2 The sample

The observed sample consists of two set of objects: five protostellar jets and ten Class I sources. In Tables 4.1 and 4.2, a list of the HH objects and Class I sources is reported, respectively. The selection criteria for each set of objects are discussed separately below.

HH objects

One of the principal objectives of this thesis is the study of the physical properties and kinematics of Class 0/I jets. With this aim, we have chosen HH objects known to be strong emitters in the NIR in order to perform medium-resolution (MR) observations at high signal-to-noise. This allows us to velocity resolve the line profiles and perform an accurate analysis of the kinematics and physical properties as a function of the jet velocity. In addition, the Class I sources were selected in such a way that emission down to the central source can be detected. The study of jets near to the source (where the jet properties have not been modified by the interaction with the surrounding material) is very important to understand the excitation conditions at the jet base and constrain ejection models. In particular, the sample is constituted by two Class I and three Class 0 jets located in the Orion and Gum nebulae. They all have been studied through different wavelengths by several authors (e.g., Reipurth et al. 2000a; Eislöffel & Mundt 1994; Nisini et al. 2005b; Podio et al. 2006) and are known as “archetypal” jets. A description of the individual objects will be done in Chap. 5. Since our main tracers are the [Fe II] lines at 1.644 μm and 1.600 μm, and the H_2 transition at 2.122 μm, observations in both the H and K bands have been performed.

Class I sources

Table 4.2: The observed sample: Class I sources

Source	α(2000.0) ($^{h\ m\ s}$)	δ(2000.0) ($^{\circ}\ '\ ''$)	α^a	L_{bol} ($L_{\odot}$)
WL12	16 24 44.3	-24 34 47.5	2.49	0.8
GSS26	16 26 10.3	-24 20 56.6	-0.46	0.3
WL18	16 26 49.2	-24 38 23.7	-0.93	0.1
WL16	16 27 02.3	-24 37 26.5	1.53	3.4
WL17	16 27 06.8	-24 38 14.6	0.61	0.4
WL15	16 27 09.4	-24 37 18.5	1.69	5.9
IRS43	16 27 26.9	-24 40 51.5	1.17	1.7
YLW16A	16 27 28.0	-24 39 34.3	2.29	1.8
YLW16B	16 27 29.4	-24 39 17	0.18	0.2
IRS54	16 27 51.9	-24 31 45.8	0.03	0.6

[a]Spectral index α=dLog(λF_{λ})/dLog(λ) from Spitzer (2-24 μm)

A sample of Class I sources have been chosen to probe the accretion properties of very embedded objects and compare the derived mass accretion rates to those of more evolved CTTS. The accretion in embedded objects can be estimated from the luminosity of the Brγ line (see, Chap. 2), located at 2.166 μm. Then, NIR spectra in the K band have been taken for a set of stars selected on the basis of detection of Brγ emission. In addition, H and J band spectroscopy has been performed to cover the forbidden emission lines as the [Fe II] 1.644 μm line (tracing the jet component) to probe the presence of protostellar jets associated with these sources and extend the number of Class I jets traced down to the central source. All the sources have been selected to belong to the ρ Oph molecular cloud from a study of Greene & Lada (1996). This ensures they form a homogeneous set of objects at the same distance avoiding possible correlations among quantities having the same dependence with the cloud distance, as e.g. the luminosity of the lines.

In Table 4.2, the list of the selected sources is presented, together with their coordinates, bolometric luminosities and spectra index of their energy distribution between 2-24 μm. This parameter is related, as described in Chap. 1, to the evolutionary state of the star. All the sources but GSS26 have $\alpha \gtrsim 0$, characteristic of the Class I sources.

4.3 VLT observations

The observations were performed at the ESO VLT telescope on Cerro Paranal, Chile, using the infrared spectrograph and camera ISAAC (Infrared Spectrometer And Array Camera) at medium- and low-resolution.

ISAAC is a spectrograph and imager with a wavelength range covering from 1 to

Table 4.3: Observations: HH objects

Object	Date	Filter	P.A. (°)	Resolution[a]	Total integration time (s)
HH34	29/12/2004	SH	-15	MR	6900
	29/12/2004	SK	-15	MR	3300
HH1	28/12/2004	SH	145	MR	5100
	28/12/2004	SK	145	MR	3300
HH46-47	29/12/2004	J	57	LR	600
	30-29/12/2004	SH	57	MR, LR	7200, 600
	29/12/2004	SK	57	MR, LR	3600, 600
HH111	28/12/2004	SH	96	MR	7200
	28/12/2004	SK	96	MR	3600
HH212	30/12/2004	SH	22	MR	900
	30/12/2004	SK	22	MR	900

[a]MR and LR observations were performed using a $0\farcs3$ and $0\farcs6$ slit width, respectively.

5 μm. It is located at the Nasmith focus of UT1 of the very large telescope (VLT) on Cerro Paranal (Chile). The pixel scale of the camera is 0.147″/pixel. ISAAC has two arms, the short wavelength arm (SW) with wavelength range from 0.98 μm to 2.5 μm and the long wavelength arm (LW) with wavelength range from 3.0 μm to 5.1 μm, both able to perform imaging and spectroscopy. It is possible to take spectra at low- and medium-resolution, with slit widths from 2″ to $0\farcs3$ and length of 120″(long slit). In Table 4.5 the wavelength range and nominal resolution for a 0.6″ and $0\farcs3$ slits at LR and MR resolution modes, respectively, are indicated. In Fig. 4.2 the response of the narrow band filters available for ISAAC is plotted. ISAAC is equipped with an Argon and a Xenon lamps, used for wavelength calibration and flat-fielding of the spectra.

Observations of the two set of objects have been carried out in two different runs. The HH objects were observed on the 28-29-30 December 2004, while the Class I sources were observed on 15-16-17 June 2006. Tables 4.3 and 4.4 report the list of the observed objects and main instrument setup.

The data were reduced using standard IRAF[2] tasks following the procedure described in Sect. 4.3.1.

4.3.1 NIR spectra acquisition and analysis techniques

Long slit spectra in the NIR are usually acquired at two positions along the slit. This technique is known as nodding and allows to subtract the sky contribution to the spectra (see Sect. 4.1). The standard procedure is to take ABBAAB. . . series of spectra, where A

[2]IRAF (Image Reduction and Analysis Facility) is distributed by the National Optical Astronomy Observatories, which are operated by AURA, Inc., cooperative agreement with the National Science Foundation.

Table 4.4: Observations: Class I sources

Object	Date	Filter	Total integration time (s)
WL12	15/06/2005	SH	2400
		SK	1920
WL15	15/06/2005	SK	240
		SH	840
IRS54	16/06/2005	SH	2400
		SK	2880
		J	2400
WL16/17	16/06/2005	SK	1920
		J	2400
		SH	2400
IRS43	16/06/2005	SH	2400
		SK	1440
YLW16A/B	17/06/2005	SH	2750
		SK	2700
GSS26	17/06/2005	SH	1440
		SK	900
		J	2400
WL18	17/06/2005	SH	1680
		SK	1600
		J	2400

All the observations correspond to MR spectroscopy performed with a slit width of $0\farcs3$.

and B indicate the two different acquisition positions along the slit. The exposure time of each image should be smaller than 5 min to avoid huge variations of the OH lines fluxes. Then, consecutive images are subtracted one from another creating couples of A-B, B-A images. In this way, the sky, bias and dark are subtracted and the result consists in a image with two spectra, one positive and one negative. Then, all the spectra are combined by multiplying each image by -1 and adding it back to itself after shifting.

Before combining the images it is necessary to remove the bad pixels and cosmic rays, flat-field and wavelength calibrate the images and correct for the slit distortion. The wavelength calibration can be done using either lamp lines or OH lines already present in the spectra. The calibration using OH lines gives more accuracy than the lamp, since lamp and object spectra are taken separately. This means that the grating position could be different at the time the target has been observed and the time the lamp spectrum has been taken. In the case of LR spectra most of the OH lines overlap each other and then the use of a lamp spectrum is needed. This is also the case of spectra where the number of OH lines is not enough to cover properly the frame. The MR spectra presented in this

Table 4.5: Wavelength range and nominal resolution for the J, SH and SK filters of ISAAC at LR for a 0.″6 slit and at MR for a 0.″3 slit.

Wavelength range (μm)	Filter	R(0.″6) (LR)	R(0.″3) (MR)
1.1-1.4	J	860	10500
1.4-1.82	SH	840	10000
1.82-2.5	SK	750	8900

thesis have been wavelength calibrated using the atmospheric OH emission lines, while an Argon-Xenon lamp was employed to calibrate the LR spectra.

Once all the images have been combined into a single spectral image, the next step is to extract the spectra of the region of interest and correct it for the telluric absorption lines. This is done by dividing the target spectrum by that of a telluric standard star previously normalised to the black-body function (at the temperature of the standard star). The standard star should be taken at the same airmass and instrument setup of the object and ideally consecutively. The spectral type of the standard should be known in order to remove its own intrinsic spectral features and obtain spectra of only telluric lines. In particular, the IR spectra presented in this thesis were corrected by a telluric standard star of spectral type B.

The last step in the reduction concerns the flux calibration of the spectra. In this case, observations of a spectrophotometric standard of known magnitude is needed. As in the case of the telluric standard, the spectrophotometric standard should be observed with the same instrument configuration and airmass as the target. Then a conversion factor between counts and flux units is derived by measuring the flux density of the standard.

Position-velocity diagrams (PVDs)

From spectral images of resolved lines it is possible to construct position-velocity diagrams. PVDs are a very useful tool to study the velocity variations and structure along extended objects, as the case of protostellar jets. These diagrams are constructed by transforming the wavelength in velocity measurements and reporting the distance of each of the features along the object with respect to a reference coordinate.

One of the axis of the PVDs of protostellar jets usually represents the distance from the driving source, while in the other axis is the velocity (Fig. 4.3).

The distance from the source is easily derived from the pixel scale of the instrument by just converting pixels into arcseconds. The velocity calibration of the spectra is done considering that, $R = c\,/\,\Delta v$, where R is the resolution of the instrument, c is the light velocity and Δv is the line velocity spread. The effective resolution have been derived from Gaussian fits to the sky OH emission lines around the interested line. The measured radial velocities are finally corrected with respect to the LSR taking into account the proper motions of the jet parent cloud.

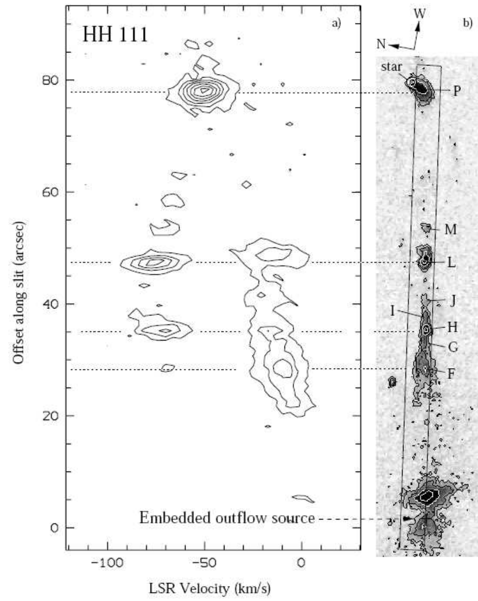

Figure 4.3: PVD for the H_2 2.122 μm line along the HH111 jet (on the left). On the x-axis the velocity with respect to the LSR is represented, while on the y-axis the distance from the source is reported. For comparison a narrow band H_2 image of the jet is presented on the right. Figure taken from Davis et al. (2001a).

In particular, PVDs of the [Fe II] 1.644 μm and H_2 2.122 μm lines have been constructed for each object assuming a vacuum wavelength of 16439.981Å (Johansson 1978) and 21218.3 Å (Bragg et al. 1982), respectively. The results are presented in Chap. 5.

Chapter 5

Velocity resolved diagnostics of Class 0/I jets.

In this chapter I will describe the analysis performed on the ISAAC spectra of the sample of jets, comprising two Class I (HH34 and HH46-47) and three Class 0 sources (HH1, HH111 and HH212), as described in Chap. 4.

HH34 and HH46-47 are two classical jets where the region close to the source is, however, optically not visible. The kinematics and physical properties of this inner jet region can be studied in detail through NIR diagnostic lines, as described in Chap. 3. In particular, the analysis in this thesis has been focused on the derivation of physical properties in the different velocity components of the jet. This diagnostic will be then used to compare the physical parameters of Class I and CTTS jets, and to constrain existing jet ejection models.

On the other hand, the observed Class 0 jets are so embedded that the central region is obscured even at NIR wavelengths. The jet is, however, seen when it emerges from the dense circumstellar envelope, usually few hundreds of AU away from the driving source. It is therefore possible to apply the same analysis performed on the Class I jets: the high sensitivity of the ISAAC instrument, in particular, have allowed to probe inner knots not previously detected and thus to derive the physical properties as close as possible to the jet basis.

In the following the results on the different observed objects are presented separately in Sections from 5.1 to 5.5. Finally in Sect. 5.6 a summary of the Class I jet properties near the source and a general discussion about the properties of Class 0/I objects are reported..

5.1 HH34

The HH34 jet is a well-known protostellar jet located in the L1641 cloud near the Orion nebulae at a distance of ~460 pc. It is known to be a parsec-scale flow (Eislöffel & Mundt 1997) being studied at optical (e.g., Reipurth et al. 2002) and IR wavelengths (e.g., Podio et al. 2006). The driving source, HH34IRS, is an embedded Class I protostar detected by

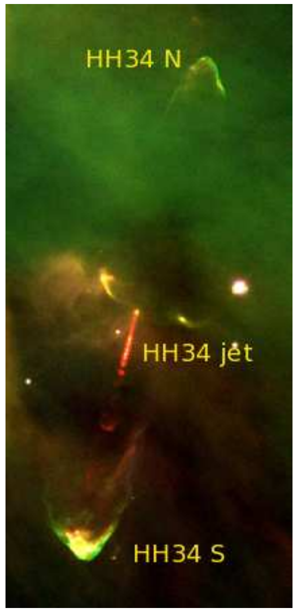

Figure 5.1: Three-colour composite image of the HH34 jet based on CCD frames taken with the ESO instrument FORS2 at VLT. The composite was taken through three different filters: B (here rendered as blue), H_α (green) and [S II] (red). North is up and East is left. The two bow-shocks HH34 N and HH34 S are indicated in the figure, together with the HH34 jet. Figure taken from Eso Press Release 17/99.

IRAS and at submm/mm wavelengths (Cohen & Schwartz 1987; Reipurth et al. 1993). This source is actively accreting, having a mass accretion rate of $\sim 4\times10^{-6}$ $M_\odot\,yr^{-1}$ (Antoniucci et al. 2008). Only the blue-shifted jet has been observed in the optical. It consists in a chain of knots ending with a spectacular bow-shock, HH34S, at a distance of 100″ from the source. The counter bow-shock is also observed at a similar distance from the source (Fig. 5.1). At NIR wavelengths the [Fe II] and H_2 emission lines trace a fast, collimated and high-excited jet and a slow, low-excitation molecular wind, respectively (Davis et al. 2001b, 2003; Takami et al. 2006). Optical IFU 2D spectra of the knots far from the central source have been performed by Beck et al. (2007), while Podio et al. (2006) combine optical and NIR spectra to derive several physical parameters along the jet beam. Finally the HH34 jet interact with the ambient medium forming a weak CO outflow mapped by Chernin & Masson (1995).

In the following, a list of the main detected lines, and the kinematics and physical properties along the flow are presented.

5.1.1 Detected lines

Figure 5.2 reports the continuum-subtracted K-band spectral images showing the different emission lines found in the HH34 jet from the ISAAC observations (see Chap. 4), while the most prominent identified lines are listed in Table 5.1. In the H-band spectral segments, only the [Fe II] 1.5999 and 1.6440 μm lines have been detected. Only the lines that are spatially resolved along the jet direction are reported: additional transitions,such as

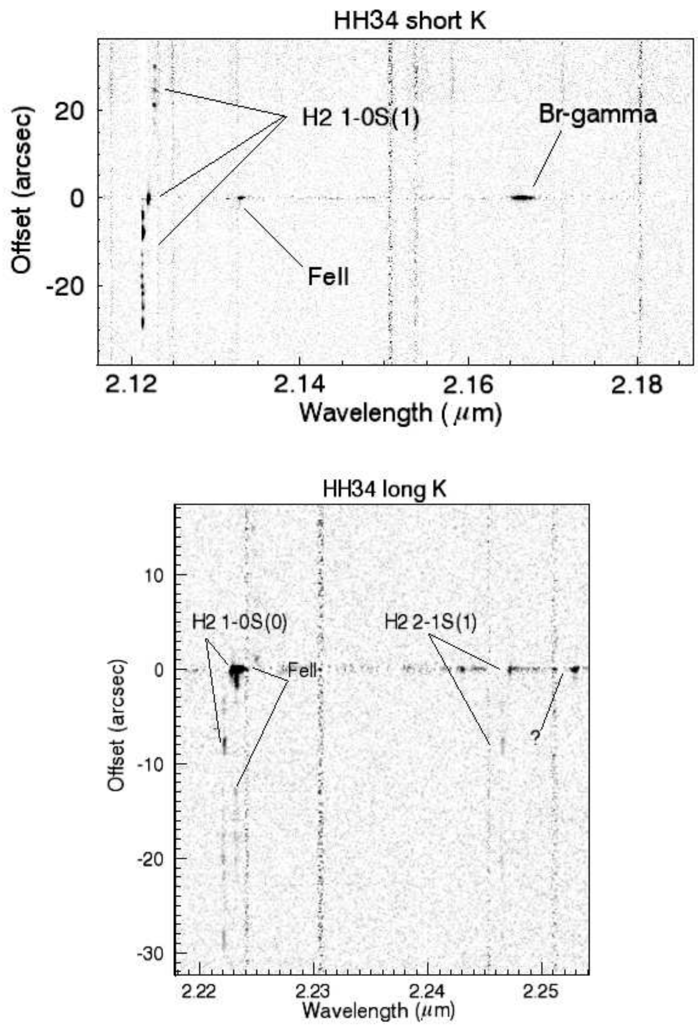

Figure 5.2: Continuum-subtracted K-band spectral images of the HH34 jet. Offsets in arcsec are with respect to the HH34-IRS driving source.

HI lines and CO transitions mostly from permitted species, such as HI lines and CO transitions, have been detected (Antoniucci et al. 2008). Along the HH34 jet, several [Fe II] lines have been detected. In addition to the 1.600 μm and 1.644 μm lines, also transitions at higher excitation energies, i.e., the 2.133 μm line connecting the ^2P and ^4P terms (see Fig. 3.2) and the 2.224 μm line (detected for the first time), originating from the ^2H term, have been observed. These transitions, with excitation energies in excess of 25 000 K probe high-excitation regions, such as those found at the jet base or in high-velocity shock interaction (see also Takami et al. 2006).

Table 5.1: List of detected lines

Line id.	λ^a
[Fe II]$a^4D_{3/2} - a^4F_{7/2}$	1.5999
[Fe II]$a^4D_{7/2} - a^4F_{9/2}$	1.6440
[Fe II]$a^2P_{3/2} - a^4P_{3/2}$	2.1333
[Fe II]$a^2H_{11/2} - a^2G_{9/2}$	2.2244
H_2 1-0 S(1)	2.1218
H_2 1-0 S(0)	2.2235
H_2 2-1 S(1)	2.2477
Brγ	2.1661

[a]Vacuum wavelengths in microns.

5.1.2 [Fe II] and H_2 kinematics: large scale properties

In order to study the kinematics of the jet in both the atomic and molecular components, position-velocity diagrams (PVDs, see Chap. 4.3.1) of the [Fe II] 1.644 μm and H_2 2.122 μm emission lines have been constructed (Fig. 5.4). The velocity is expressed with respect to the local standard of rest for both PVD. A parental cloud velocity of 8 km s^{-1} has been adopted (Anglada et al. 1995), and subtracted in the final PV velocity scale. Distance scales (in arcsec) have been measured with respect to HH34 IRS.

The intensity scale is different in the PVDs of the blue and red-shifted lobes as evidenced by the relatively weak red-shifted emission. The redshifted counterpart of the HH34 jet is clearly detected in the spectral images. The blue-shifted emission knots have been named from A to L, following the nomenclature of Eislöffel & Mundt (1992) and Reipurth et al. (2002) (Fig. 5.3). There is not emission detected, however, from the knot B, since this knot is not aligned with the main jet axis, as evidenced in Reipurth et al. (2002). The next knots observed are the knots C and D, which are grouped together as knot C. The red-shifted knots which are located at approximately symmetric positions with respect to the corresponding blue-shifted knot have been detected for the first time here and name from rA to rH.

The values of the [Fe II] and H_2 1-0S(1) peak velocities have been computed applying a Gaussian fit to the line profile of every blue and red-shifted knot emission, and listed them in Table 5.2. In the knots closer to the star, where two velocity components have been identified, their peak velocity has been measured separately considering a two-Gaussian fit. The [Fe II] radial velocities in the blue lobe cover a range from -92 to -108 km s^{-1}, which is consistent with the values measured by Takami et al. (2006) and Davis et al. (2003), who found a range in radial velocities for the blue lobe from -90 to -100 km s^{-1}, corrected for a cloud velocity of 8 km s^{-1}. From knots A6 to I the blueshifted radial velocity increases from ~-92 to ~-100 km s^{-1}, passing through a maximum at ~ -108 km s^{-1}, then decreases again down to ~-92 km s^{-1}at knot K. Finally, it increases in knot L to ~-98 km s^{-1}. Errors in relative velocities are estimated to be of the order of 2 km s^{-1}, since

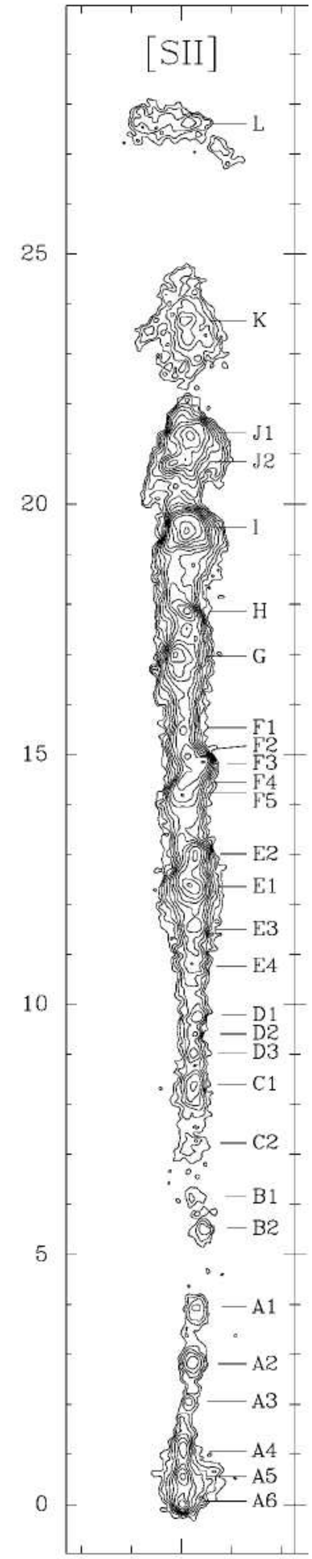

Figure 5.3: Contours plot of the HH34 jet as seen in [S II] from the WFPC2 camera on HST. The knots along the jet are identified. Figure taken from Reipurth et al. (2002).

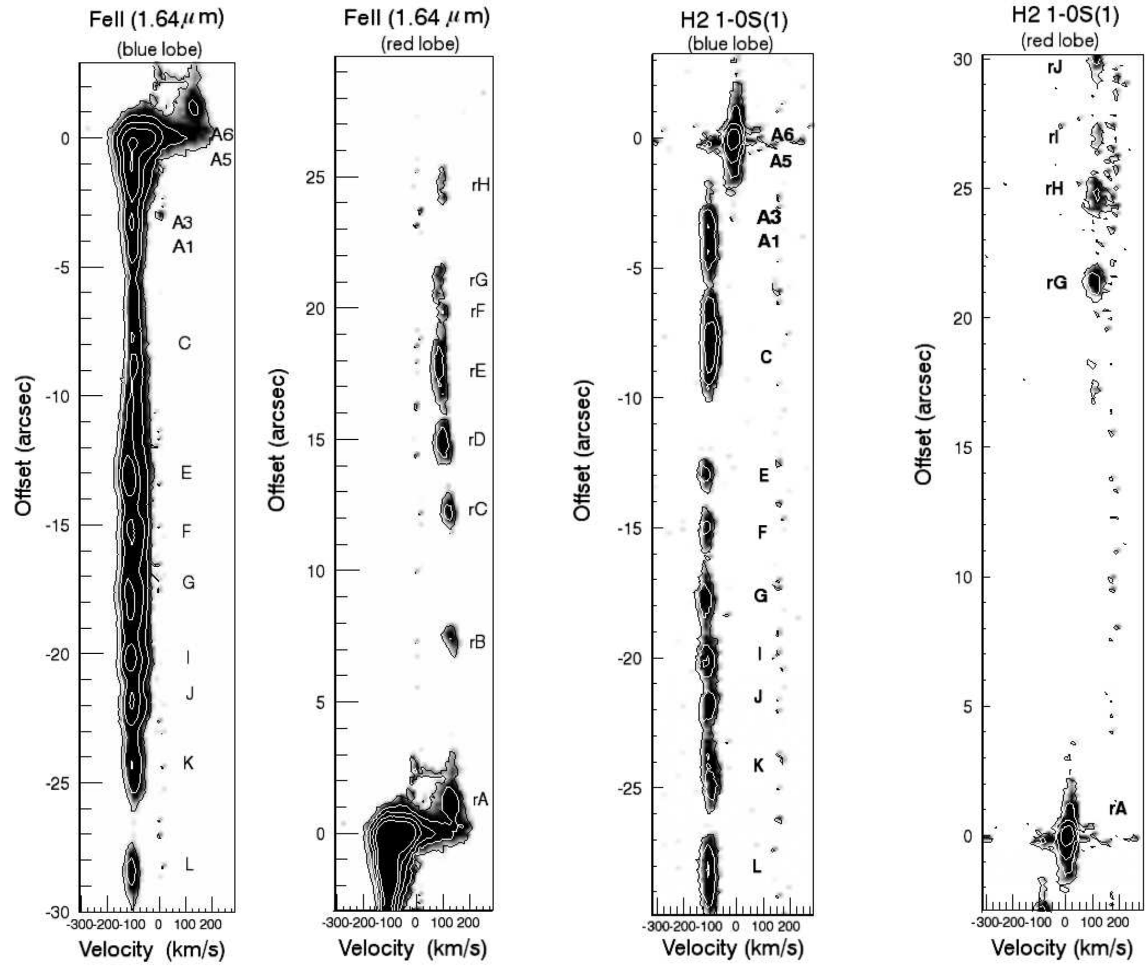

Figure 5.4: Continuum-subtracted PV diagrams of the [Fe II] 1.644 μm and H_2 1-0S(1) emission lines for the blue and red lobe of the HH34 jet. A P.A. of -15° was adopted. Contours show [Fe II] 1.644 μm intensity values of 5, 15, 45, 135, 405 σ for the blue lobe, and 5, 10, 20, 40, 80 σ for the red lobe. The contours plotted on the H_2 1-0S(1) PVDs show values of 5, 15, 45, 135, 405 σ for both lobes. On the Y-axis the distance from HH34 IRS is reported.

our wavelength calibration has an uncertainty of 0.1Å. The [Fe II] radial velocity along the red lobe shows a similar behaviour. The velocity roughly increases from the knot closest to the source, rA, to the knot rB, from ~130 km s^{-1} to ~140 km s^{-1}, then decreases down to a value of ~96 km s^{-1}. Table 2 reports the velocity dispersion of the [Fe II] emission, measured from the FWHM of the Gaussian fit, deconvolved for the instrumental profile. In knots A6-A3-A1, where different velocity components are evident (see Sect. 5.1.3) the reported velocity dispersion refers to the brightest component at high velocity. Intrinsic line widths of the order of 35-40km s^{-1} are observed all along the jet. Under the assumption that the line emission arises from unresolved shock working surfaces, the shock velocity is roughly given by $V_s \sim \Delta V$(FWZI)$\sim 2 \times \Delta V$(FWHM), following Hartigan et al.

(1987). This implies shock velocities of the order of 70-80km s^{-1}, thus much higher than the value of ~30km s^{-1} estimated by Hartigan et al. (1994) on the basis of the comparison of optical line ratios with shock models. Indeed, shocks with speeds as high as 80km s^{-1} are expected to produce a strong ionisation, on the order of $x_e \sim 0.3 - 0.4$ (Hartigan et al. 1994), while Podio et al. (2006) measured an average ionisation along the HH34 jet of only 0.04. Therefore, it seems that the line widening is determined not only by the shock, but also by, e.g., a lateral expansion of the jet.

The H_2 radial velocities have a range from -89 to -110 km s^{-1} for the blue lobe and an average value of ~+115 km s^{-1} for the red lobe. The H_2 line profile is resolved all along the jet, with ΔV values of the order of 10-30 km s^{-1} .

Also, the H_2 radial velocities show cyclic variations on small scales along the jet with an increase of roughly 20 km s^{-1} from knot A6 to knot E and a subsequent decrease of the same order at knot K.

It is known that the HH34 jet presents velocity variability on large and small spatial scales. Raga & Noriega-Crespo (1998) and Raga et al. (2002) have shown that to reproduce the velocity pattern observed at different epochs, a model of variable ejection velocity including three modes with different periods is needed. The fastest of these modes can be represented with a sinusoid having a period of 27 yrs and an amplitude of ~15 km s^{-1}. This is roughly consistent with the observed velocity pattern, that is reproduced quite closely by both [Fe II] and H_2 and by the red-shifted and blue-shifted gas, clearly indicating its origin from ejection velocity variability. The velocity pattern observed at large distance may, however, be biased by the change in the jet axis direction that occurs at d~5″ from the source, coupled with the widening of the jet diameter (up to ~0.″6 at ~20 arcsec from the source, Reipurth et al. 2002). Adopting an instrumental slit of only 0.″3, part of the kinematical components of the jet may not be properly probed by this observations.

5.1.3 [Fe II] and H_2 kinematics: Small scale properties

Close to the central source, the [Fe II] lines broaden and emission at lower velocities, down to 0 km s^{-1}, appears within ~3″ from the central source (Fig. 5.5). Inside ~1″ emission also at positive velocities is detected, reconnecting with the spatially resolved red-shifted knot rA. This central region was already observed in [Fe II] and H_2 by Davis et al. (2001b, 2003) and Takami et al. (2006). Our observations have, however, a better spatial resolution than Davis et al. (2001b, 2003) and are much deeper than those of Takami et al. (2006), who did not detect the [Fe II] redshifted component at the jet base. We name the high blue-shifted velocity corresponding to the large scale jet as the high velocity component (HVC) and the emission component from 0 to ~50 km s^{-1} as the low velocity component (LVC), in analogy with the HVC and LVC observed in the forbidden emission line (FEL) regions of T Tauri stars (see Sect. 2.1.3).

Table 5.2: Observed radial velocities along the HH34 jet.

Blue lobe						Red lobe				
		[Fe II] 1.64 μm		H_2 2.12 μm				[Fe II] 1.64 μm	H_2 2.12 μm	
Knot	r_t^a	HVC^b	LVC^b	HVC^b	LVC^b	Knot	r_t^a		HVC^b	LVC^b
A6	0.0	-92 (46)	-52	-89 (30)	-4	rA	+1.0	+133 (43)		+10
A3	-3.0	-98 (37)	-67	-98 (17)	-15	rB	+7.3	+141 (51)		
A1	-4.5	-93 (37)	-68	-95 (12)	-7	rC	+12.3	+128 (58)		
C	-9.0	-92 (43)		-94 (12)	-7	rD	+15.0	+108 (35)		
E	-12.5	-108 (44)		-110 (8)		rE	+17.4	+96 (43)		
F	-15.2	-100 (43)		-107 (12)		rFG	+21.0	+96 (46)	+113 (26)	
G	-17.2	-106 (43)		-111 (8)		rH	+25.4	+100 (35)	+115 (21)	
I	-20.0	-100 (43)		-105 (24)						
J	-22.1	-96 (43)		-99 (19)						
K	-24.8	-92 (44)		-92 (26)						
L	-28.9	-98 (26)		-99 (19)						

[a]Distance from the source in arcsec given by the mean value in the adopted aperture. Negative values correspond to the southeastern, blue-shifted jet axis.

[b]Radial velocities (in km s^{-1}) with respect to the local standard of rest and corrected for a cloud velocity of 8 km s^{-1}. The radial velocity error is 2 km s^{-1}. The velocity dispersion (in km s^{-1}), measured from the line FWHM deconvolved for the instrumental profile, is reported in brackets for the HVC.

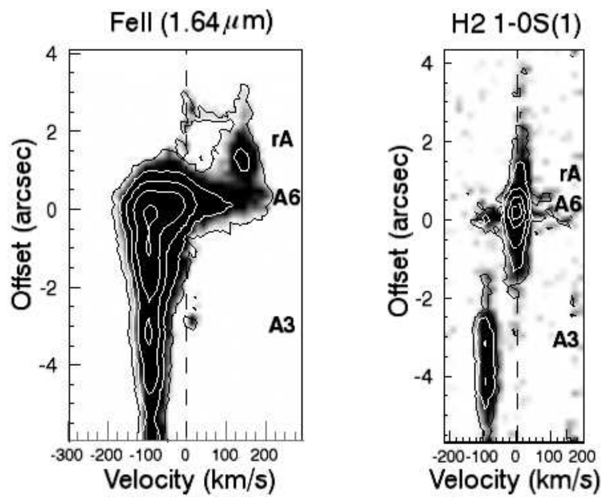

Figure 5.5: Continuum-subtracted PV diagrams for the [Fe II] 1.644 μm and H_2 1-0S(1) emission lines of the HH34 jet in the region nearest to the source. A P.A. of -15° was adopted. Contours show values of 5, 15, 45, 135, 260 σ for both lines. On the Y-axis the distance from HH34 IRS is reported.

At variance with [Fe II], the H_2 PVD shows spatially- and kinematically-separated LVC and HVC, and only the LVC is visible down to the central source. This component is close to 0 km s^{-1} LSR velocity and the blue-shifted and red-shifted jets differ by less than 10 km s^{-1}. The HVC appears at a distance of 2″ from the central source, at the position of the knots A6 and rA. At intermediate velocities between these two components, no emission is seen in the H_2 PVD. This suggests that the two components correspond to physically distinct regions. The origin of the H_2 HVC and LVC will be further discussed in Sect. 5.6.1.

5.1.4 Diagnostics of physical parameters

Electron density

The electron density in the atomic jet component can be derived from the ratio of the [Fe II] 1.600/1.644 μm lines as explained in Chap. 3. This ratio is sensitive to n_e values between ~10^3 and 10^5 cm^{-3}, while it depends only weakly on the temperature (e.g. Nisini et al. 2002). Taking advantage of the velocity resolved profiles in both the [Fe II] 1.644 and 1.600 μm lines, the electron density has been measured in the different velocity components. To do that, the spectra of the two lines at different positions along the flows have been extracted. Then, the 1.600 μm/1.644 μm intensity ratio in each pixel along the spectral profile has been measured. Figure 5.6 shows the normalised profiles of the two [Fe II] 1.644 μm and 1.600 μm lines and their ratio as a function of velocity for four knots along the HH34 jet, while in Appendix– plots of the other knots are reported. The spatial intervals used to extract the spectra of the individual knots are given in Table 5.3. The

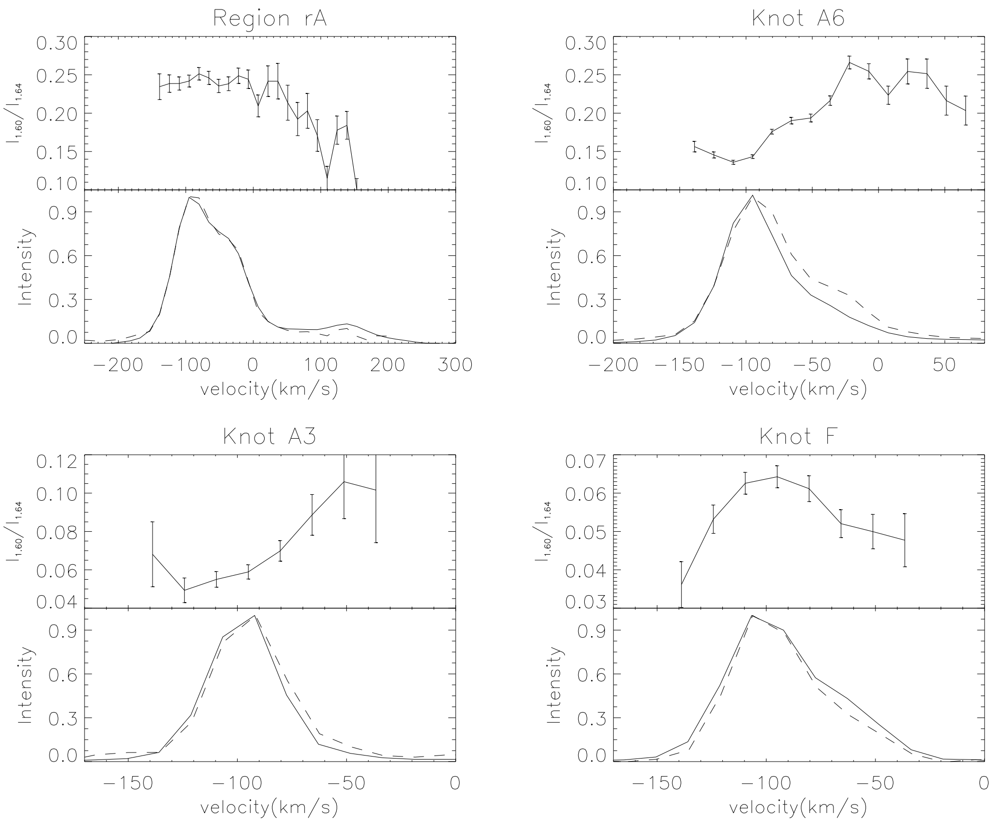

Figure 5.6: Normalised line profiles (lower panels) of the [Fe II] lines 1.644 μm (solid line) and 1.600 μm (dotted line), and their ratio in each velocity channel (upper panel) for different extracted knots along the HH34 jet. Note that rA is a region that includes the knot rA.

[Fe II] line ratio has been computed only for the velocity points where the intensity in both the lines has been measured with a S/N larger than three. This ratio gives a qualitative indication on how n_e varies in the different velocity components, that is, a higher ratio indicates a higher electron density. In the internal knots of HH34 (from A6 to A3) the 1.600 μm/1.644 μm ratio decreases by ~70% going from ~-50 km s^{-1} to -100 km s^{-1}. In the knots farther from the central source (e.g., knot F), on the other hand, the maximum 1.600 μm/1.644 μm ratio is observed at the radial velocity peak, with some evidence that the ratio decreases in the line wings at both higher and lower velocities.

In addition, the contribution from the HVC and LVC of the jet has been separated in the line profile to have a quantitative determination of the electron density in the different velocity components. The ratio values have been converted into n_e values applying a 16 level Fe^+ statistical equilibrium model (Nisini et al. 2002). In HH34, HVC and LVC velocity ranges have been defined from the profile of the 1.600 μm line of knot A6, where the two components have been fitted with a two-Gaussian fit. The line ratios have been then measured considering the intensities integrated in the FWHM ranges of these two Gaussian also for all the other knots. The considered velocity bins are from ~-120 km s^{-1}

to ~-66 km s^{-1} (HVC) and from ~-66 km s^{-1} to ~-7 km s^{-1} (LVC). The adopted A_v and T_e values are given in Table 5.3, together with the derived electron densities in the two components. Figure 5.7 plots the derived values of n$_e$ as a function of the distance from the source. The first trend that can be noticed is a sharp decrease of the HVC electron density (from ~10^4 to ~ 2×10^3 cm^{-3}) from the knot A6 to the other knots at distances farther than 2″.5 from the source. Such a decrease in n_e has also been observed in Podio et al. (2006) and the values they derived, scaled for the different considered spatial regions observed through slits of slightly different width, are consistent with our measured values for n_e. In the red-shifted knot rA, which is the only knot where significant [Fe II] 1.600 μm emission has been detected in the red-lobe, a value for $n_e \sim 1.2 \times 10^4$ cm^{-3} is found, i.e., comparable to the value derived in knot A6. Secondly, as shown in Fig. 5.7, the values for n_e in the LVC are higher than in the HVC: in knot A6, the LVC electron density is 2.2×10^4 cm^{-3}, i.e., 70% higher than in the HVC. About the same percentage is measured in knots A1 and A3. From the information in our data, we are unable to disentangle whether the larger electron density in the LVC with respect to the HVC is due to a higher total density or to a higher ionisation fraction.

In the outer knots, i.e., from C outwards, high and low velocity components cannot be distinguished any more. Instead, the density here seems to have the opposite behaviour, with the higher density at the velocity peak and the lower densities in the line wings. The analysis performed in these knots located far from the source could, however, be affected by a not-perfect alignment of the slit with the jet axis and by the intrinsic jet width larger than the slit, as discussed in Sect. 5.1.2. Nevertheless, such a pattern agrees with the results obtained by Beck et al. (2007) using integral field spectroscopy of this part of the jet. They found that both the velocity and the electron density decrease with distance from the jet axis. Such behaviour is consistent with models for jet internal working surfaces.

Mass loss rate

The mass loss rate in the different velocity components has been also derived to examine which of them is transporting more mass in the jet. The derived $\dot{M}_{jet}$ values together with the parameters adopted are reported in Table 5.3, while in Fig. 5.7, the HH34 $\dot{M}_{jet}$ is plotted for the HVC and LVC as a function of the distance from the central source.

The $\dot{M}_{jet}$ value was obtained from the luminosity of the [Fe II] 1.644 μm line, adopting the relationship derived for forbidden emission lines described in Sect. 3.4. In addition, all iron has been supposed to be ionised, and with a solar abundance of 2.8×10^{-5} (Asplund et al. 2005) implying that iron is all in gas phase. To compute the fractional population, the n$_e$ values derived separately for the LVC and HVC have been used, while a single temperature for both components has been assumed equal to 7000 K for HH34. This temperature is given by the average value derived by Podio et al. (2006) in knots from E to I . Tangential velocity values have been derived from the radial velocities assuming an inclination angle instead of taken the proper motions values already computed in literature. For HH34, an inclination angle with respect to the plane of the sky of i=22°.7±5° (Eislöffel & Mundt 1992) has been assumed. The inclination angle derived by Eislöffel

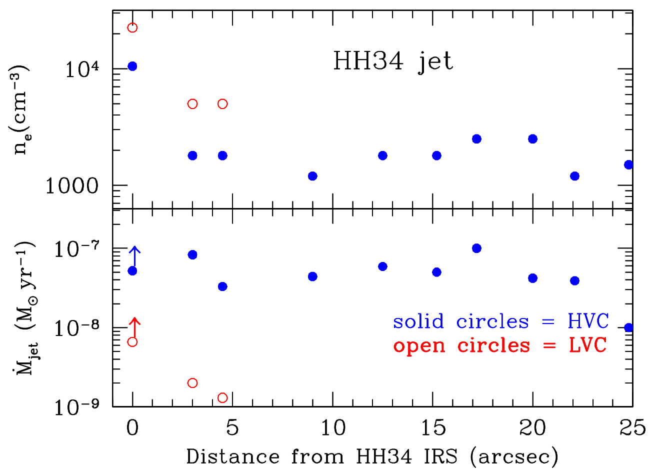

Figure 5.7: The electron density (upper panel) and mass flux (bottom panel) are represented as a function of the distance from the source for the HH34 jet. Solid circles indicate the the electron density and mass flux for the HVC, while open circles refer to the values of the LVC.

& Mundt (1992) is preferred to the value of i=30° estimated by Heathcote & Reipurth (1992), who did not consider the pattern motion of the jet knots. The resulting tangential velocities of the HVC derived here are listed in Table 5.3. The velocities derived for the internal knots are smaller (by ∼20-50 km s^{-1} in knots A6-A3) and larger in the more distant knots than the values derived by the proper motion analysis of the [S II] emission by Reipurth et al. (2002). In particular, no evidence for a deceleration of the jet is detected as shown by Reipurth et al. (2002), and the velocity remains higher than 200km s^{-1} along the jet length. This could be an indication either that the inclination angle does not remain constant along the jet, or that the [Fe II] line has a kinematical behaviour different from [S II]. Finally, the luminosity of the [Fe II] 1.644 μm line has been computed by integrating the extinction corrected flux of the knot in the same range of velocity used to calculate the electronic density.

The mass flux rate in the LVC ($\dot{M}_{jet}$ (LVC)) is lower than $\dot{M}_{jet}$ (HVC) by a factor of about 10. The $\dot{M}_{jet}$ (HVC)/ $\dot{M}_{jet}$ (LVC) ratio does not reflect the derived n_e ratio in the two components, indicating that the $(n_H V) \times v_t$ product is significantly smaller in the LVC (around 8 times) than in the HVC. Since the difference in tangential velocity between each component is not enough to justify such a result, the larger $\dot{M}_{jet}$ (HVC) indicates a significant higher $(n_H V)$ product in the HVC, i.e, the HVC has either an emission volume or a total density larger than the LVC, or both. This result could be biased by the finite slit width with respect to the jet diameter. In fact, the jet width measured only by HST in the optical lines is less than 0.″3 up to a distance of 5″from the source (Reipurth et al. 2002). In addition, the jet emission in the LVC could be broader than the jet width derived from velocity-integrated emission maps, as observed, e.g., in DG Tau (Bacciotti et al. 2000). This effect probably does not account for the difference of nearly two orders of magnitude in derived mass-loss rates for the LVC and HVC in the inner regions of HH34, but the derived mass-loss rates for the LVC are likely lower limits. It has to be also noted that the reported values of $\dot{M}_{jet}$(HVC) remain roughly constant ($\sim 5 \times 10^{-8}$ M$_{\odot}$/yr) along the whole jet as expected in steady jet flows. This fact excludes significant flux losses as the jet opening angle increases.

The mass flux derived for the internal knot A6 is very low, much smaller than the $\dot{M}_{jet}$ value in knot A3. This is likely due to the fact that the same extinction value of 7.1 mag has been assumed for both knots, as estimated by Podio et al. (2006) as an average over the entire knot A, i.e., over 4″. The extinction value on-source has been estimated to be about 45 mag (Antoniucci et al. 2008): therefore, a large dust column density gradient is expected in the inner jet region. Assuming an A$_V$ lower limit of 7.1 mag also in the red-shifted component rA, a lower limit for $\dot{M}_{jet}$ of $\sim 1 \times 10^{-9}$ M$_{\odot}$ yr^{-1} is found. It should be finally noted that the $\dot{M}_{jet}$ determined here for the HH34 jet agrees fairly well with the velocity integrated values estimated in Podio et al. (2006). The same authors derived an iron gas phase abundance from the [Fe II][P II]ratio (see, Chap. 3) along the HH34 jet of (Fe/H)$_{g}as$ $\sim$3.67$\times$10^{-6}. This means that around a 87% of the iron is located in grains along the jet and implies that the values presented in Table 5.3 are lower limits of the actual $\dot{M}_{jet}$. If this new iron gas-phase abundance is used in instead of the solar one, an average $\dot{M}_{jet}$ value of $\sim$2$\times$10^{-7} M$_{\odot}$ yr^{-1}is found, almost a factor 4 larger than the previous estimation.

It is interesting to compare the derived mass flux rates with the source mass accretion rate, to estimate the $\dot{M}_{jet}/\dot{M}_{acc}$ efficiency in embedded young sources. Antoniucci et al. (2008) have derived a mass accretion rate of the order of 4.1$\times$10^{-6} M$_{\odot}$ yr^{-1} for HH34 IRS. This would imply $\dot{M}_{jet}/\dot{M}_{acc} \geq 0.01$ if assuming no dust depletion or $\dot{M}_{jet}/\dot{M}_{acc} \sim 0.03$ assuming the iron gas abundance from Podio et al. (2006). These values are in agreement with what is found in T Tauri stars and predicted by MHD jet launching models (e.g., Ferreira et al. 2006).

Table 5.3: $\dot{M}_{jet}$ along the HH34 jet.

Knot	r_t [a] ($''$)	A_V [b] mag	V_t(HVC) [c] (km s^{-1})	n_e(HVC) [d] (10^3 cm^{-3})	$\dot{M}_{jet}$(HVC) [e] ($M_\odot$ yr^{-1})	V_t(LVC) [c] (km s^{-1})	n_e(LVC) [d] (10^3 cm^{-3})	$\dot{M}_{jet}$(LVC) [e] ($M_\odot$ yr^{-1})
A6	(-2.6,+0.9)	7.1	218	10.5	5.2×10^{-8}	124	22.5	6.6×10^{-9}
A3	(-3.8,-2.6)	7.1	232	1.8	8.3×10^{-8}	159	5.0	2.0×10^{-9}
A1	(-5.4,-3.8)	7.1	220	1.8	3.3×10^{-8}	162	5.0	1.3×10^{-9}
C	(-9.9,-8.0)	7.1	218	1.2	4.4×10^{-8}			
E	(-14.1,-11.0)	1.3	255	1.8	5.9×10^{-8}			
F	(-16.6,-14.1)	1.3	236	1.8	5.0×10^{-8}			
G	(-17.8,-16.6)	1.3	251	2.5	1.0×10^{-7}			
I	(-21.0,-19.2)	1.3	236	2.5	4.2×10^{-8}			
J	(-23.3,-21.0)	1.3	227	1.2	3.9×10^{-8}			
K	(-26.1,-23.5)	1.3	217	1.5	1.0×10^{-8}			
L	(-30.3,-27.5)		232					
rA	(0, +2.0)	7.1	218	12.0	2.2×10^{-9}			

[a] Distance from the source in arcsec. Negative values correspond to the southeastern, blue-shifted jet axis.
[b] Visual extinction from Podio et al. (2006).
[c] Tangential velocity assuming an inclination of the jet i=22°.7 to the plane of the sky (Eislöffel & Mundt 1992).
[d] Electron density for the HV and LV components.
[e] $\dot{M}_{jet}$ for the HV and LV components assuming an electron temperature of 7000 K, and all Fe is in gas phase.

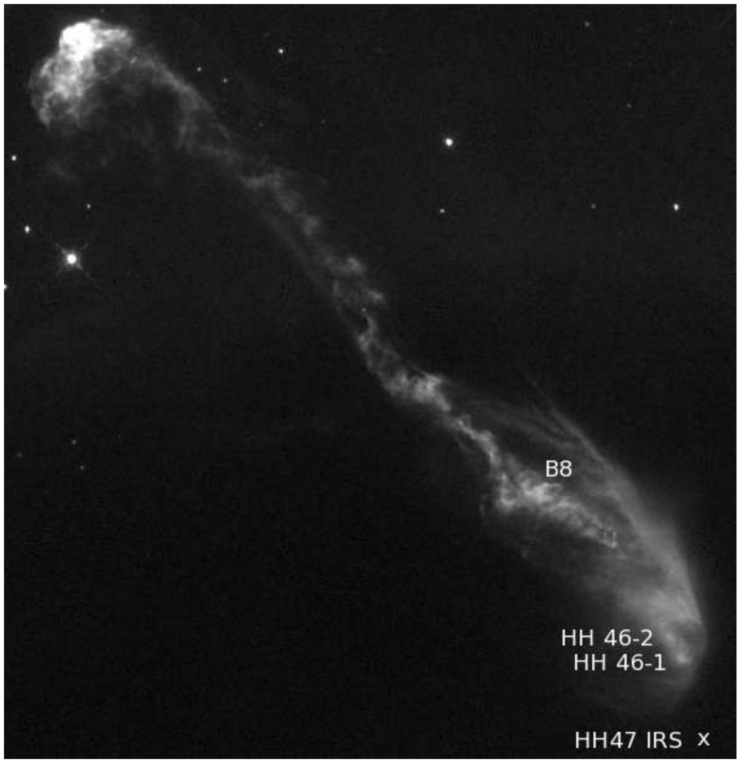

Figure 5.8: HST image of the HH46-47 jet combining two WFPC2 images at [S II] and H_α wavelengths. Only the blue-shifted lobe of the jet is detected. The position of the source HH47 IRS is indicated together with some bright knots. North is up and East is left.

5.2 HH46-47

5.2.1 Object description

The HH46-47 jet is located in a Bok globule close to the Gum nebulae at a distance of ~450 pc. It consist in a blue- and red-shifted jet, the latter detected at IR wavelengths down to the central source, that emerges from a reflection nebulae. The source, HH47IRS is a Class I object that actually consists in a binary system separated by 0.″26 (Reipurth et al. 2000b). The present of a close binary system makes HH46-47 a precessing jet with a well-defined wiggling structure clearly seen at optical wavelengths (Fig. 5.8). The two lobes of HH46-47 end in two bow-shock structures, the HH47A and HH47C. In Fig. 5.9 a H_2 2.12 μm continuum-subtracted image of the HH46-47 jet is represented. The ISAAC slit position is depicted over the image, where only the knots covered by the slit are indicated. At the source position a negative residual from the continuum subtraction is present. The HH46-47 jet is at the border of the Bok globule and powers an atomic and molecular bipolar flow. The north-eastern (blue-shifted) portion of the flow is detected at optical wavelengths while the counterjet is better detected in the infrared since it moves into the globule. In fact, we have identified the red-shifted knots Z1, Z2, X, Y1, Y2 and Y3 and the blue-shifted knots HH46-1, HH46-2 and B8. We have named the knots

Table 5.4: Lines observed in the knot Z1 of the HH46-47 jet.

Line id.	λ	F	ΔF	Line id.	λ	F	ΔF
		10^{-16} erg cm^{-2} s^{-1}				10^{-16} erg cm^{-2} s^{-1}	
[Ti II] $^{2}G_{7/2}$-$^{4}F_{7/2}$	1.140	8.3	3.5	[Fe II] $a^{4}D_{3/2}$-$a^{4}F_{3/2}$	1.797	9.8	1.1
H_2 2-0 S(1)	1.162	5.8	2.2	[Fe II] $a^{4}D_{5/2}$-$a^{4}F_{5/2}$	1.800	7.1	0.8
[P II] $^{3}P_{2}$-$^{1}D_{2}$	1.188	3.5	1.0	[Fe II] $a^{4}D_{7/2}$-$a^{4}F_{7/2}$	1.810	38.2	2.1
H_2 4-2 S(5)	1.226			[Ni II] $a^{2}F_{7/2}$-$a^{4}F_{9/2}$	1.939	11.6	1.0
H_2 3-1 S(1)	1.233			H_2 2-1 S(5)	1.945	11.0	1.5
H_2 2-0 Q(1)	1.238			[Fe II] $a^{4}D_{7/2}$-$a^{4}F^{*}_{5/2}$	1.954		
[Fe II] $a^{4}D_{7/2}$-$a^{6}D_{9/2}$	1.257	106.0	0.8	H_2 1-0 S(3)*	1.958		
[Fe II] $a^{4}D_{1/2}$-$a^{6}D_{1/2}$	1.271	5.9	1.0	H_2 2-1 S(4)	2.004	2.7	0.3
[Fe II] $a^{4}D_{3/2}$-$a^{6}D_{3/2}$	1.279	7.8	0.1	H_2 1-0 S(2)	2.034	26.1	0.6
[Fe II] $a^{4}D_{5/2}$-$a^{6}D_{5/2}$	1.295	11.9	0.9	H_2 2-1 S(3)	2.074	8.1	0.5
[Fe II] $a^{4}D_{3/2}$-$a^{6}D_{1/2}$	1.298	6.7	0.12	H_2 1-0 S(1)	2.122	68.5	0.3
[Fe II] $a^{4}D_{7/2}$-$a^{6}D_{7/2}$	1.321	306	0.8	H_2 2-1 S(2)	2.154	3.9	0.3
[Fe II] $a^{4}D_{5/2}$-$a^{6}D_{3/2}$	1.328	8.4	0.9	[Fe II] $b^{2}F_{5/2}$-$a^{2}F^{*}_{7/2}$	2.224		
[Fe II] $a^{4}D_{7/2}$-$a^{6}D_{5/2}$	1.372	71.7	1.0	H_2 1-0 S(0)*			
[Fe II] $a^{4}D_{5/2}$-$a^{4}F_{9/2}$	1.534	173.0	0.7	H_2 2-1 S(1)	2.248	8.5	0.5
[Fe II] $a^{4}D_{3/2}$-$a^{4}F_{7/2}$	1.600	10.6	0.5	H_2 3-2 S(1)	2.386	1.6	0.4
[Fe II] $a^{4}D_{7/2}$-$a^{4}F_{9/2}$	1.644	160.0	0.6	H_2 1-0 Q(1)	2.407	50.0	0.8
[Fe II] $a^{4}D_{1/2}$-$a^{4}F_{5/2}$	1.664	7.0	0.7	H_2 1-0 Q(2)	2.413	18.3	0.9
[Fe II] $a^{4}D_{5/2}$-$a^{4}F_{7/2}$	1.677	142.0	0.3	H_2 1-0 Q(3)	2.424	47.4	0.9
H_2 1-0 S(9)	1.687	4.2	0.5	H_2 1-0 Q(4)	2.437	18.9	1.3
[Fe II] $a^{4}D_{3/2}$-$a^{4}F_{5/2}$	1.712	2.1	0.4	H_2 1-0 Q(5)	2.455	42.9	1.5
[Fe II] $a^{4}D_{1/2}$-$a^{4}F^{*}_{3/2}$	1.745	6.3	0.8	H_2 1-0 Q(6)	2.476	16.0	1.7
H_2 1-0 S(7)*	1.748	150.0	0.6	H_2 1-0 Q(7)	2.500	47.4	3.7
H_2 1-0 S(6)	1.788	9.4	0.5				

Vacuum wavelengths in microns.

* Blend of the two indicated lines.

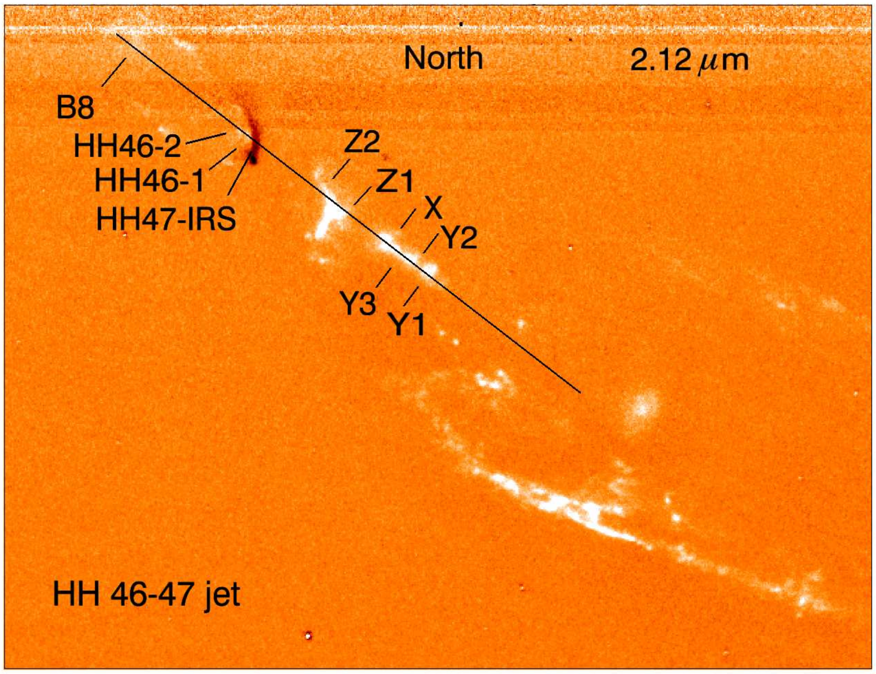

Figure 5.9: Position of the ISAAC slit superimposed on the H_2 2.12 μm image of the HH46-47 jet. Individual knots along the jet are identified following the nomenclature of Eislöffel & Mundt (1994).

following the nomenclature of Eislöffel & Mundt (1994). The redshifted knots Z and Y in Eislöffel & Mundt (1994) have been divided here in knots Z1 and Z2, and Y1, Y2 and Y3.

In the following sections, I will present separately the results and analysis on the HH46-47 jet found from LR and MR spectroscopic data.

5.2.2 Observed lines

Figure 5.10 shows the intercalibrated ISAAC LR spectra of knot Z1. This knot is among the brightest ones along the HH46-47 jet showing both molecular and atomic transitions. A list of the observed lines in knot Z1 together with their fluxes are reported in Table 5.4, while in the Appendix we list all the lines detected in the other knots. The principal observed lines are [Fe II] and H_2 lines. The H_2 emission is mainly located at positions far from the source, while near the protostar several atomic lines are present. The observed H_2 transitions come mainly from the two first vibrational levels. In addition to [Fe II] and H_2 emission, other elements as [P II] and [Ti II] are also detected in the knot S and Z1. In the MR spectra only the [Fe II] 1.600 and 1.644 μm lines are detected in the H-band, while for the K-band the H_2 1-0S(1), 3-2S(4) and 2-1S(2), the [Fe II] 2.1349 and 2.1609 μm and the Brγ lines are detected (see Fig. 5.11). The presence of the Brγ near the source

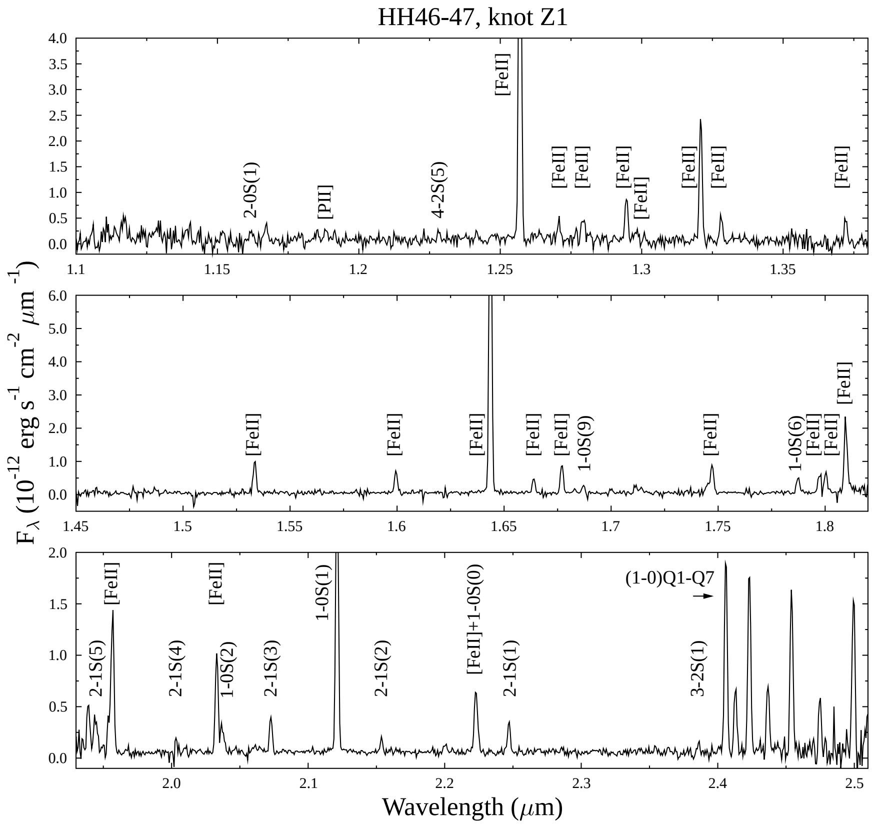

Figure 5.10: LR spectrum from 1.00 to 2.50 μm of the knot Z1 in the HH46-47 jet. The stronger lines are identified.

and the H_2 3-2S(4) line from a distance of 10″ to 25″ from HH46-IRS testifies the high excitation conditions in these regions. In the on-source spectra for the H- and K-band other features are present, as the Br14 and Br12 and some CO transitions (Antoniucci et al. 2008).

5.2.3 Kinematics

The PVDs of the [Fe II] 1.644 μm and H_2 2.122 μm lines constructed from the analysis of the MR spectroscopic data are presented in Fig. 5.12. The velocity is expressed with respect to the Local Standard of Rest (LSR) and corrected from a parental cloud velocity of +20 km s^{-1} (Hartigan et al. 1993). In the Y-axis the distance from the driving source HH46-IRS, in arcsec, is represented. The continuum of the source has been subtracted in both the PVDs to more clearly see the structure of the lines near to HH46-IRS. The intensity scale is different in the two PVDs in order to evidence the different condensations in the atomic and molecular gas.

In both PVDs the red- and blue-shifted lobes of the HH46-47 jet are evidenced. Emis-

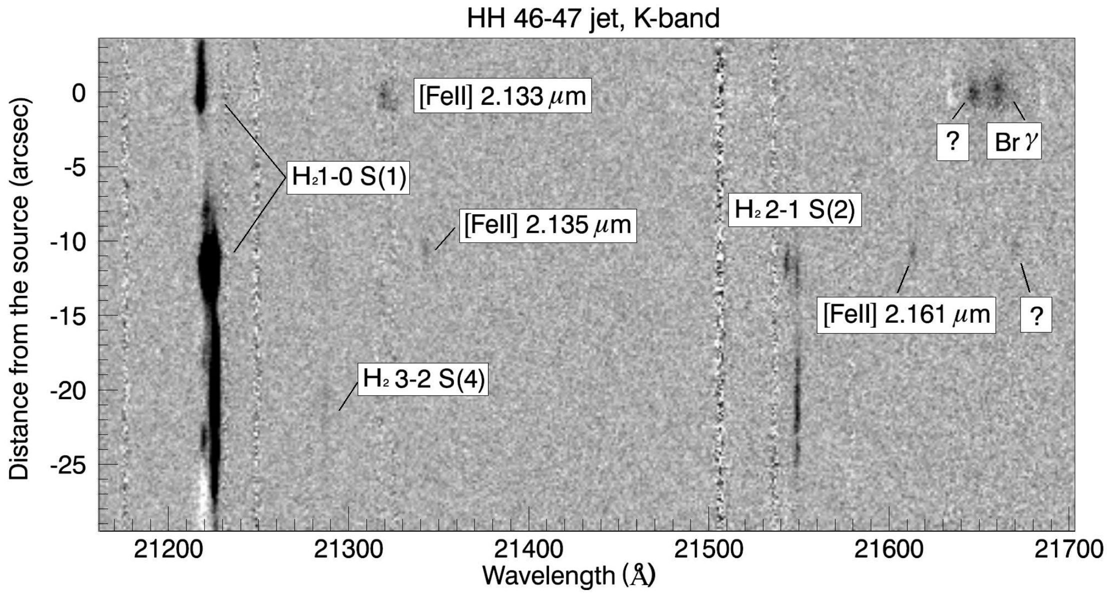

Figure 5.11: MR continuum subtracted spectral image of the HH46-47 jet in the K-band.

sion down to the central source is detected in both the atomic and molecular components, forming a new knot named here as knot S. The [Fe II] emission broaden as it approaches the source position and reaches velocities down to 0 km s^{-1} within 2$''$ from the source. Inside 1$''$ there is also emission at redshifted velocities up to $\sim$ +100 km s^{-1}. The large scale blue-shifted high velocity component is identified as the high velocity component (HVC) and the emission component from -100 to $\sim$100 km s^{-1} as the low velocity component (LVC). At variance with the atomic emission, the H_2 emission shows only one velocity component well represented by a single Gaussian peaked at $\sim$20 km s^{-1}.

The radial velocities measured with respect to the LSR and corrected from the cloud velocity are reported in Table 5.5 for the [Fe II] 1.644 μm and H_2 2.122 μm lines. The radial velocities have been computed by a Gaussian-fit to the line profile of every knot. The velocities of the [Fe II] emission range from -177 km s^{-1} to -235 km s^{-1} and from +94 km s^{-1} to +144 km s^{-1} in the blue- and red-lobe, respectively. The HVC and LVC in knot S peak at -213 km s^{-1} and around -138 km s^{-1}. The knot Z2 presents, as well, a double velocity component peaked at +144 km s^{-1} and +92 km s^{-1}. Due to the large distance of knot Z2 with respect to the source position ($\sim$8$''$),the double peaked line profile is not interpreted here as associated with a FEL region but instead with the presence of a bow-shock.

In the case of the H_2 emission, the radial velocities vary from -15 km s^{-1} to -48 km s^{-1} in the blue-lobe an from +26 km s^{-1} to +94 km s^{-1} in the red-lobe. At variance with the [Fe II] emission, knot S only shows a single velocity component at -15km s^{-1}, while knot Z1 is clearly formed by two velocity components at +89 km s^{-1} and +10 km s^{-1}. This fact supports the presence of a bow-shock structure in the vicinity of this knot. The same argument can be applied to knot X that shows a double peaked velocity at +93 km s^{-1} and

$+14\,\mathrm{km\,s^{-1}}$, as well.

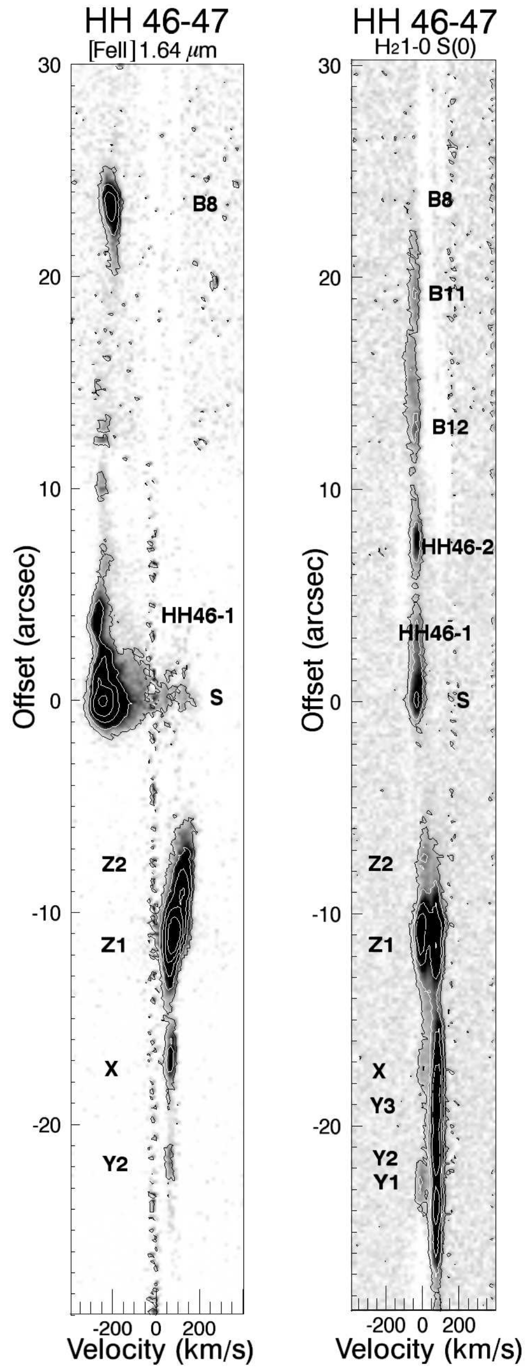

Figure 5.12: Continuum-subtracted PVDs for the [Fe II] $1.644\,\mu$m and H_2 $2.122\,\mu$m lines along the HH46-47 jet. Contours show values of 3, 9, … , $243\,\sigma$ for the [Fe II] line and 4.5, 13.5,…,$364.5\,\sigma$ for the H_2. On the Y axis distance from the source HH46-IRS in arcsec is reported.

Table 5.5: Observed radial velocities along the HH46-47 jet.

Knot	[Fe II] 1.644 μm V(km s^{-1})	H_2 2.122 μm V(km s^{-1})
B8	-177(46.0)	
HH46-1	-235(49.2)	-20
S	-213(63.2)),~-138	-15
Z2	+144(44.2), +92	+26
Z1	+112(43.5)	+89, +10
X	+94(36.6)	+93, +14
Y3		+94
Y2		+92
Y1		+92

Note: Radial velocities (km s^{-1}) corrected from a cloud velocity of +20 km s^{-1} (Hartigan et al. 1993) and with respect to the LSR.

Table 5.6: A_V along the HH46-47 jet.

Knot	$A_V \pm \triangle A_V$ [a] (mag)
S	6.6±0.2
Z2	12.5±1.6
Z1	6.1±0.1

[a] Visual extinction measured from the ratio [Fe II] 1.64/1.25 μm

5.2.4 Low resolution spectral analysis

Extinction

From the [Fe II] 1.644/1.257 μm ratio the visual extinction for different knots along the HH46-47 jet has been derived (see Chap. 3) and reported in Table 5.6. Only lines with S/N greater than three have been used to computed the intensity ratio.

To convert the observed ratios in A_v values, we have adopted the radiative transition probabilities given by Quinet et al. (1996) as they seem to better reproduce the intrinsic line ratio (see e.g., Giannini et al. 2008). The extinction errors have been estimated directly from the flux error of each line. We have to keep in mind, however, that the extinction is affected, as well, by the uncertainty in the transition probabilities of the lines involved (see e.g., Nisini et al. 2005b; Giannini et al. 2008).

Analysing in more detail the extinction values derived from the [Fe II] 1.644/ 1.257 μm ratio, it can be noticed that A_V varies from ~6 in the knots Z1 and S to ~12 in knot

Table 5.7: T, $\dot{M}_{jet}$ (H_2) along the HH46-47 jet.

Knot	T (K)	$\dot{M}_{jet}$ (H_2) ($M_\odot$ yr^{-1})
Z1	2580 ± 50	3.7×10^{-9}
X	2078 ± 42	7.3×10^{-10}
Y3	2564 ± 53	4.6×10^{-9}
Y2	2330 ± 50	6.4×10^{-9}
Y1	2093 ± 42	3.0×10^{-9}

Z2. Fernandes (2000) found a value of $A_V = 9.38 \pm 1.49$ in a region that covers our knots HH46 and S. He employed, however, the theoretical ratio given by the Einstein spontaneous probabilities of Nussbaumer & Storey (1988) that has been shown to predict too high A_V values. On the other hand, Antoniucci et al. (2008) found an A_V ~40 mag on-source, indicating a large density gradient towards the source position. The extinction in the knot Z2 is roughly twice the extinction of the knots S and Z1. This fact could be due to a collision of the jet with stationary material of a side of the cavity. Heathcote et al. (1996) note the presence of an oblique shock due to the impact of the blue-shifted lobe of the jet with the cavity at ~6″from the source. The same process may occur at the opposite position giving rise to an increase of the extinction.

H_2 temperature and mass flux

Along the HH46-47 jet, several H_2 lines have been observed, mainly coming from the v=1-2 vibrational levels. Using the different H_2 detected transitions, excitation diagrams for several knots along the jet have been constructed (see Chap. 3). As an example, Fig. 5.13 shows the excitation diagram of the knot Z1, the brightest knot observed in HH46-47, while the excitation diagrams for the rest of the knots are reported in the Appendix—. The different symbols indicate lines coming from different vibrational levels, while the straight line represents the best fit through our data. In the knot Z1 a temperature value of $T = 2797 \pm 100\ K$ is found, assuming $A_V \sim 6$ as estimated by the [Fe II] lines. This extinction value is consistent with that inferred from the ratio of the H_2 lines 1-0 S(1) and 1-0 Q(3), that have same energy values (see Sect. 3.3).

The mass flux carried out by the warm molecular component has been also estimated from the observed H_2 transitions. In Chap. 3.4 a description on how derive $\dot{M}_{jet}$ from H_2 transitions can be found. $\dot{M}_{H_2}$ has been derived in the same spatial region extracted for the [Fe II] line analysis. The dv_t has been taken from Eislöffel & Mundt (1994) and the $N(H_2)$ value for each knot, has been found from the interception to zero of the straight line fitted to the H_2 transitions in the Boltzmann diagram. The average $\dot{M}_{jet}$ value along the jet is $\sim 3.7\times10^{-9}$ $M_\odot$ yr^{-1}. The derived results for each knot are reported in Table 5.7.

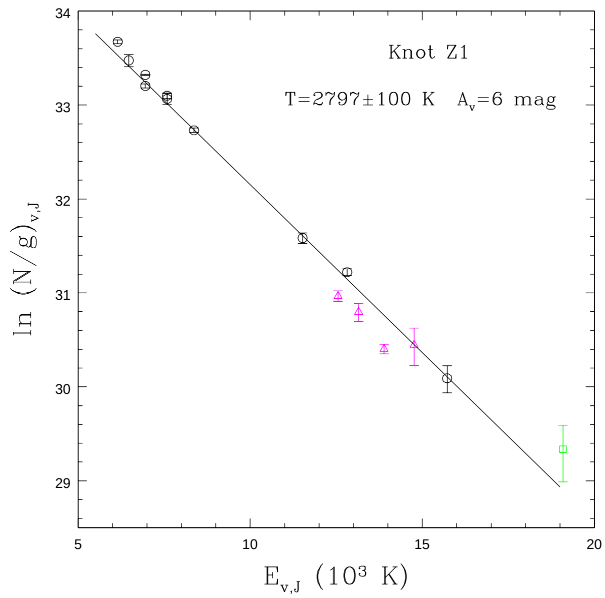

Figure 5.13: H_2 rotational diagram for the different lines in the knot Z1 of HH46-47. Different symbols indicate lines coming from different vibrational levels. The straight line represents the best fit through the data. The corresponding temperature and the adopted extinction value is indicated.

Electron density

The electron density (n_e) has been derived from the [Fe II] 1.600/1.644 μm line ratio. From the LR spectra (R~800, i.e., Δv~370km s^{-1}) is not possible to resolve the different velocity components. Thus, the electron density has been derived integrating the total flux of the line profile of every extracted knot for both the lines. The n_e values and the intervals used to extract the knots are reported in Table 5.8. The electron density decreases with the distance from the source, from a value of 9400 cm^{-3} in knot S to a value of 1500 cm^{-3} in knot Z1. The same behaviour has been observed previously in other IR jets like HH1, HH111 and HH34 (see Nisini et al. 2005b; Podio et al. 2006).

[Fe II] depletion

The [Fe II] / [P II] line ratio can be used to estimate the iron gas-phase abundance (see Chap 3.2). In particular, the iron abundance has been derived for the knots S and Z1, where both the [Fe II] 1.257 μm and the [P II] 1.188 μm lines have been detected. A [Fe II] / [P II] ratio of ~7.3 and ~25.6 have been found in the knots S and Z1. These values indicate that around 88% and 58% of iron is located in dust grains in knots S and Z1, respectively. This lead to a $(Fe/H)_{gas} \sim 3.92 \times 10^{-6}$ in the knot S and a $(Fe/H)_{gas} \sim 1.18 \times 10^{-5}$ in the knot Z1.

Table 5.8: Electron density along the HH46-47 jet.

Knot	r_t[a] ($''$)	$n_e \pm \triangle n_e$[b] (cm^{-3})	n_e(HVC)[c] (cm^{-3})	n_e(LVC)[b] (cm^{-3})
S	(-3.4,+2.8)	6300^{+1700}_{-1300}	5400	7650
Z2	(-9.3,-5)	1300^{+1800}_{-1200}	2350	4600
Z1	(-14.8,-9.3)	3200^{+700}_{-850}	3100	

[a]Distance from the source in arcsec. Negative values correspond to the southeastern, redshifted jet axis.
[b]Electron density measured from the ratio [Fe II] 1.60/1.64μm .
[c]Electron density measured from the ratio [Fe II] 1.60/1.64μm for the HVC and LVC.

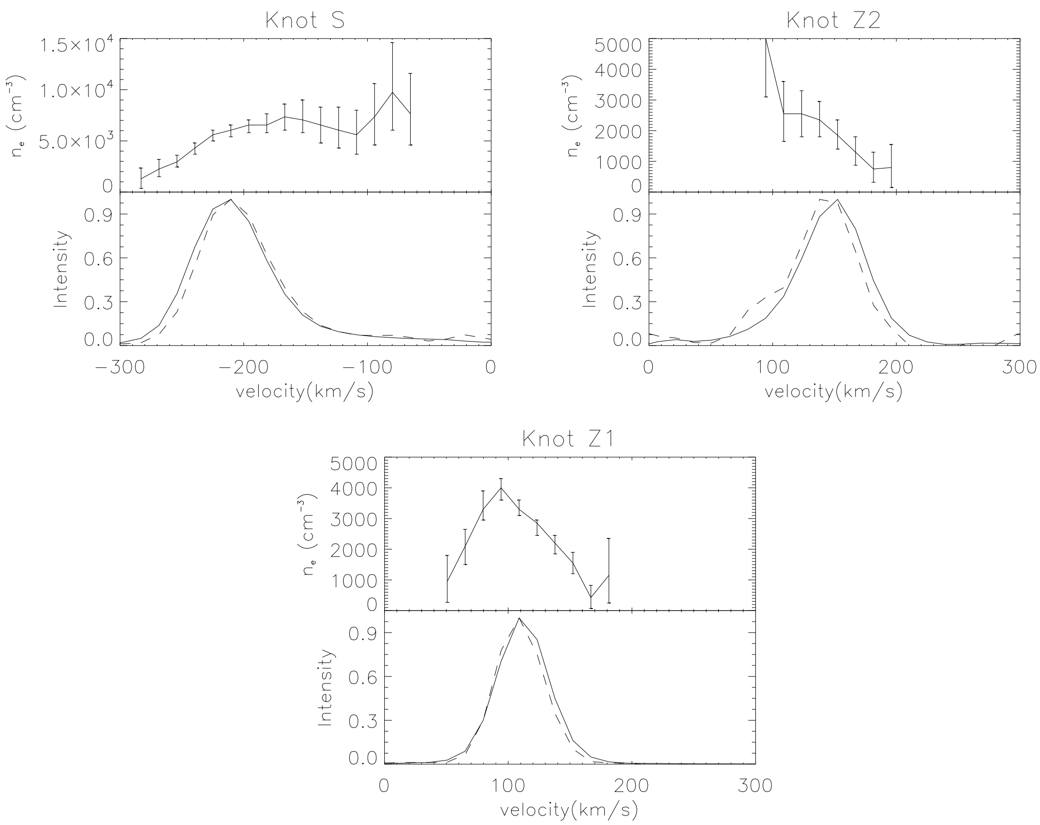

Figure 5.14: Normalised line profiles (lower panels) of the [Fe II] lines 1.644μm (solid line) and 1.600μm (dotted line), and their ratio in each velocity channel (upper panels) for different extracted knots along the HH46-47 jet.

5.2.5 Medium resolution spectral analysis

Electron density and Mass flux

The [Fe II] 1.600 and 1.644μm lines have been also detected in the knots S, Z1 and Z2 at medium resolution. In this case, we have derived the electron density as a function of the

Table 5.9: $\dot{M}_{jet}$ along the HH46-47 jet.

Knot	v_t(HVC)[a] (km s^{-1})	$\dot{M}_{jet}$ (HVC)[b] (10^{-7} M$_\odot$ yr^{-1})	v_t(LVC)[b] (km s^{-1})	$\dot{M}_{jet}$ (LVC)[c] (10^{-8} M$_\odot$ yr^{-1})
S	316	0.3-1.9	205	0.5-3.6[b]
Z2	213	0.4-0.9[b]	136	0.2-0.4[b]
Z1	166	0.4-1.0[b]		

[a]Tangential velocity assuming an orientation angle of the jet with respect to the plane of the sky of 34° (Eislöffel & Mundt 1994).

[b]$\dot{M}_{jet}$ measured from the luminosity of the [Fe II] 1.64 μm for the HVC and LVC. The lower value has been derived assuming an iron solar abundance, while the upper value has been inferred assuming the iron gas-phase abundance derived from the [Fe II][P II] ratio.

radial velocity in the same way as described for the case of HH34 Sect. 5.1.4. Figure 5.14 represents the electron density in each pixel along the MR spectral profile of the knots S, Z1 and Z2 (upper panel) together with the normalised line profile of the [Fe II] 1.600 μm and 1.644 μm lines (bottom panel). From this figure we can infer that n_e increases as the velocity decreases in all the detected knots. It should be noticed that while knot S clearly is formed in a FEL region, knots Z2 and Z1 located far from the driving source, are the result of the shock interaction of the jet with the cavity.

Near to the source (knot S) a HVC ranging from ∼-239 km s^{-1} to ∼-181 km s^{-1} has been defined by a Gaussian-fit to the line profile of the [Fe II] 1.644 μm line. It was, however, not possible to define a LVC by a Gaussian-fit in this knot. Instead, a velocity range from ∼-181 km s^{-1} to ∼-50 km s^{-1} has been defined consistent with the velocity distribution of the PVD of the [Fe II] 1.644 μm line. For the knots far from the source, the HVC intervals of the knots Z1 and Z2 have been defined from ∼88 km s^{-1} to 136 ∼ km s^{-1}, and from ∼110 km s^{-1} to ∼167 km s^{-1}. The knot Z2 shows a LVC, as well. In this case, it was possible to adjust a Gaussian-fit to the LVC from the [Fe II] 1.600 μm line profile, resulting in a LVC range from ∼80 km s^{-1} to ∼110 km s^{-1}.

The n_e values for the two velocity components are reported in Table 5.8. As already pointed out from the analysis of the LR data, there is a decrease in the electron density from the inner to the more external knots in both velocity components. Secondly, as evidenced by Figure 5.14, the electron density of the LVC (n_e(LVC)∼4600-7600) is larger than the electron density of the HVC (n_e(HVC)∼3000-5000).

In order to compute the contribution to the mass flux of the atomic component, we have derived $\dot{M}_{jet}$ from the luminosity of the [Fe II] 1.644 μm line, following the approach described in Chap. 3.4 and Sect.5.1.4. An inclination angle of the jet with respect to the plane of the sky, $i \sim 34°$ (Eislöffel & Mundt 1994), has been assumed and used to infer the velocity of the knots projected perpendicular to the line of sight, through our measurements of the radial velocity. A list of the length of the knots projected perpendicular to the line of sight used to derive $\dot{M}_{jet}$ is reported in Table 5.8. The [Fe II] 1.644 μm line flux

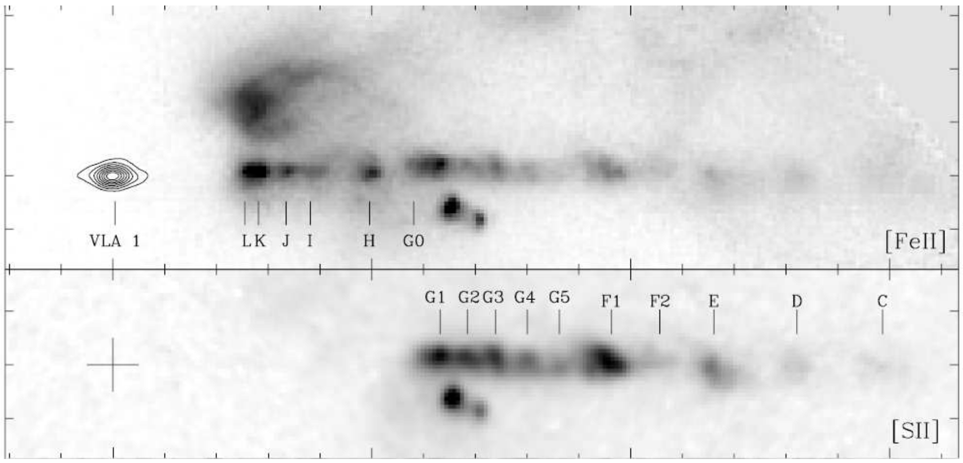

Figure 5.15: HST image of the HH1 jet. (Top) NICMOS image in [Fe II] at 1.644 μm. (Bottom) WFPC2 image in [S II] at 6717/6731 Å. The position of the source, VLA1, is indicated in both panels. Tick marks represents intervals of 1″(~460 pc at the distance of HH1). The detected knots along the flow are labelled. Figure taken from Reipurth et al. (2000a).

has been dereddened using the extinction derived from the ratio [Fe II] 1.644/1.257 and reported in Table 5.6. The resulting values found for $\dot{M}_{jet}$ are listed in Table 5.9, assuming a solar abundance of iron and thus, represent a lower limit. In the same table, the $\dot{M}_{jet}$ values derived considering the gas-phase Fe abundance measured from the Fe/P analysis are also reported, in the assumption that the same dust depletion factor is valid for both the HVC and LVC. In any case, the mass flux rate is ~ 16 times larger in the HVC than in the LVC, while in both the velocity components $\dot{M}_{jet}$ decreases with the distance from the driving source. As discussed for the HH34 jet, this means that the HVC has either a n_H or V larger than the LVC, or both.

Finally, it is interesting to compare the derived mass ejection flux with the mass accretion rate in the source. Antoniucci et al. (2008) have derived a $\dot{M}_{acc}$ for HH46-IRS of the order of 2.2×10^{-7}. Assuming $\dot{M}_{jet}$ranging between 0.3×10^{-7} and 2×10^{-7} $M_\odot$ yr^{-1}, this implies a $\dot{M}_{jet}/\dot{M}_{acc}$ ~0.1-0.9 still in agreement with predicted by MHD jet models (Ferreira 1997).

5.3 HH1

The HH1 jet is an archetypal flow, that has been analysed spectroscopically by several authors at optical (Eislöffel et al. 1994) and infrared (Davis et al. 2000b; Eislöffel et al. 2000) wavelengths. This jet is located in the L1641 cloud in Orion at a distance of ~460 pc and only its blue-shifted component is detected. The jet consists in a chain of knots observed down to ~6″ and ~3″ at optical and infrared wavelengths (Fig. 5.15). Two well-known bow-shocks at approximated 70″ from the source are observed at red-shifted and blue-shifted velocities showing a complex structure that have been studied in detail through optical, infrared and millimetre wavelengths (Eislöffel et al. 1994; Moro-Martín

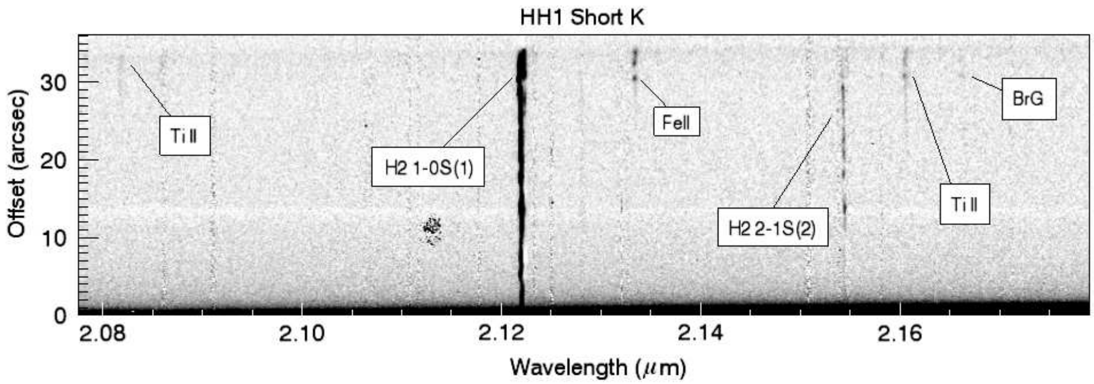

Figure 5.16: Continuum-subtracted K-band spectral image of the HH1 jet. Offset is with respect to the CS star.

et al. 1999; Davis et al. 2000b). The HH1 jet source, VLA1, is a Class 0 object not visible neither at optical or infrared wavelengths, being first detected through cm wavelengths by Pravdo et al. (1985). Nisini et al. (2005b) presented a combined optical/infrared study of this jet revealing different excitation conditions along the flow.

In the following, a list of the main detected lines, and the kinematics and physical properties along the HH1 jet are presented.

5.3.1 Detected lines

Figure 5.16 report the ISAAC K-band spectral image showing the different emission lines detected along the HH1 jet, while the most prominent identified lines are listed in Table 5.10. In addition to the two H_2 lines 1-0S(1) and 2-1S(1), the [Fe II] 2.133 μm line, connecting the ^2P and ^4P terms, and two transitions from [Ti II](characterised by excitation temperature of the order of 7000 K) have been also detected. These lines have been detected here for the first time in shocks environments. Weak Brγ emission has been also observed localised in a single knot H, testifying for the high-excitation conditions in this knot. In the H-band spectral segment, only the [Fe II] 1.5999 and 1.6440 μm lines have been detected.

5.3.2 [Fe II] and H_2 kinematics

Figures 5.17 and 5.19 show the PVDs of the H_2 2.122 μm and [Fe II] 1.644 μm lines of the HH1 jet. The PVDs of the [Fe II] 2.133 μm and [Ti II] 2.160 μm lines are also presented in Fig. 5.19. The velocity is expressed with respect to the local standard of rest in all the PVDs and subtracted by a parental cloud velocity of 10.6 km s^{-1} (Choi & Zhou 1997). Distance scales (in arcsec) have been measured with respect to the jet driving source VLA1. Since VLA1 is not visible in the near-IR, we have used the bright Cohen-Schwartz (CS) star as the positional reference, adopting for it an angular separation of 35.″9 from the

Table 5.10: List of detected lines

Line id.	λ^a
[Fe II]$a^4D_{3/2} - a^4F_{7/2}$	1.5999
[Fe II]$a^4D_{7/2} - a^4F_{9/2}$	1.6440
[Fe II]$a^2P_{3/2} - a^4P_{3/2}$	2.1333
[Ti II]$a^2F_{5/2} - a^4F_{3/2}$	2.1605
[Ti II]$a^2F_{7/2} - a^4F_{5/2}$	2.0818
H_2 1-0 S(1)	2.1218
H_2 2-1S(2)	2.1542
Brγ	2.1661

[a]Vacuum wavelengths in microns.

source VLA1. The observed knots are named from KL to P, following the nomenclature by Eislöffel et al. (1994) and Bally et al. (2002). [Fe II] is detected only in the knots closer to the star, from KL to E, while H_2 can be traced all along the jet; as already shown by Davis et al. (2000b) and Nisini et al. (2005b), the ratio [Fe II] /H_2 sharply decreases with the distance from VLA1. Such a decrease is accompanied by a decrease of the H_2 and [Fe II] radial velocities. Also the velocity dispersion diminishes from the internal to the external knots, as shown in Table 5.11. In particular, the measured intrinsic FWHM (i.e., deconvolved by the instrumental width) decrease from $\sim 64\,\mathrm{km\,s^{-1}}$ in knots KL to $\sim 20\,\mathrm{km\,s^{-1}}$ in knots G-F. These values imply high shock speeds (from $\sim 120\,\mathrm{km\,s^{-1}}$ in knot KL to $\sim 40\,\mathrm{km\,s^{-1}}$ in knot G), progressively decreasing outwards. Indications of high shock velocities in the internal knots of HH1 are given by the detection of the Brγ and [Fe II] 2.133μm lines in knot H. These lines are not detected in knots KL and JI probably due to the larger extinction. The [Fe II] and H_2 radial velocities appear double-peaked from knot KL to H in [Fe II] and from knot KL to F in H_2. Both, [Fe II] and H_2 present one of the two components red-shifted with respect to the LSR.

The [Fe II] blue-shifted radial velocity increases from knot KL to knot JI from a value of $\sim$-28 $\mathrm{km\,s^{-1}}$ to $\sim$-46 $\mathrm{km\,s^{-1}}$ and then decreases again to a velocity of $\sim$-24 $\mathrm{km\,s^{-1}}$ in knot E. The red-shifted component is, however, too faint to be fitted with a Gaussian profile. Nevertheless, we can estimate an average value of $\sim$+30 $\mathrm{km\,s^{-1}}$ from knot KL to H.

On the other hand, in the H_2 blue-shifted component the velocity increases from knot KL to knot JI, as in the case of [Fe II] and then roughly decreases to $\sim$-3 $\mathrm{km\,s^{-1}}$ in knot A. After that, the radial velocity increases again to a value of around $-12\,\mathrm{km\,s^{-1}}$ in knot N. The red-shifted component covers a velocity range from +6 to +23 $\mathrm{km\,s^{-1}}$. The H_2 line profiles are represented in Fig. 5.17 for several knots in the region closest to the source. The measured H_2 velocities are consistent with the velocities reported in Davis et al. (2000b) for the knots F and A. The H_2 lines are non-resolved implying an intrinsic line width less than 39 $\mathrm{km\,s^{-1}}$.

The origin of the double velocity component can be due either to the presence of

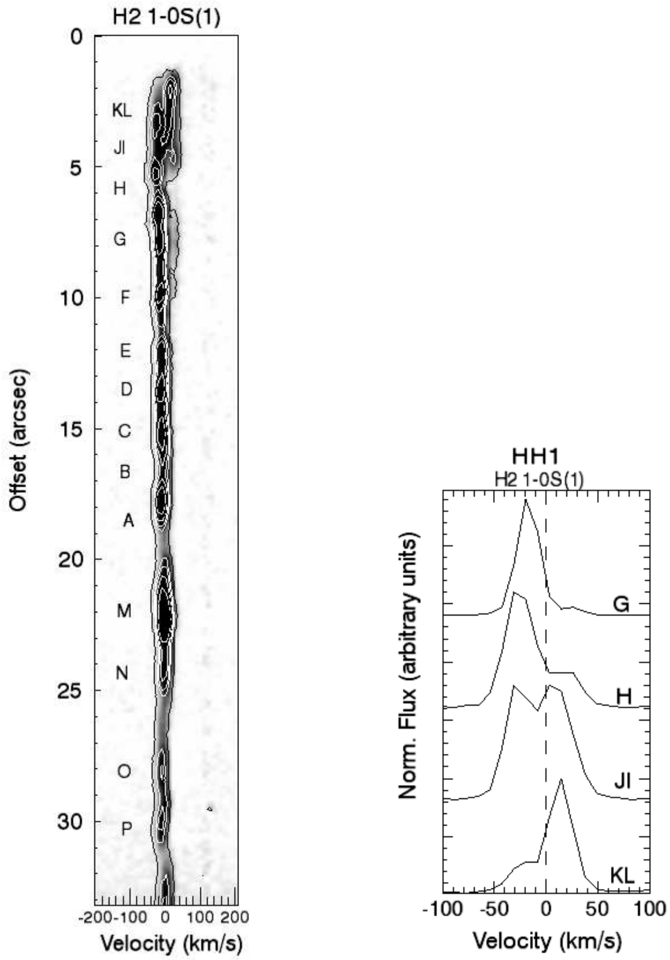

Figure 5.17: (left) Continuum-subtracted PVD for the H_2 1-0 S(1) line along the HH1 jet. A position angle of 145° was adopted. Contours show values of 10, 40, 60, 100 σ. On the Y-axis the distance from the driving source VLA1 is reported.(right) Normalised line profiles of the H_2 1-0S(1) for different knots near the source.

another jet (e.g., the one driving the HH501 object Reipurth et al. 2000a; Bally et al. 2002) or to the emission along the wings of a bow shock seen almost perpendicular to the line of sight. These two possibilities will be further discussed in the next section.

5.3.3 Diagnostics of physical parameters

Electron density

The electron density as a function of velocity in the atomic jet component has been derived from the ratio of the [Fe II] 1.600/1.644 μm lines following the same procedure applied to the HH34 jet and described in Chap. 5.1.4. Electron densities of the [Fe II] emission line region as a function of the distance from the driving source have been measured by Nisini

Table 5.11: Observed radial velocities along the HH1 jet.

Knot	$r_t{}^a$ ($''$)	[Fe II] 1.64 μm $V_r{}^b$	H_2 2.12 μm V_r^b Blue	H_2 2.12 μm V_r^b Red
KL	1.6	-28 (64)	-16	+13
JI	3.4	-46 (53)	-27	+6
H	5.1	-43 (47)	-24	+14
G	7.5	-35 (22)	-17	+23
F	9.8	-31 (20)	-14	+17
E	11.6	-24 (29)	-11	
D	13.6		-12	
C	15.0		-10	
B	17.0		-11	
A	18.2		-3	
M	22.1		-4	
N	23.5		-12	

[a]Distance from the source in arcsec given by the mean value in the adopted aperture.
[b]Radial velocities (in km s^{-1}) with respect to the LSR and corrected for a cloud velocity of 10.6 km s^{-1}. The radial velocity error is 2 km s^{-1}. The velocity dispersion (in km s^{-1}), measured from the line FWHM deconvolved for the instrumental profile, is reported in brackets for the HVC.

et al. (2005b). They found that n_e decreases from a value of ~2000 cm^{-3} in the internal knots LK to ~700 cm^{-3} in the external section of the jet.

Figure 5.18 shows the normalised profiles of the [Fe II] 1.600 and 1.644 μm lines and their ratio as a function of velocity. The spatial intervals used to extract the spectra of the individual knots are given in Table 5.12.

In HH1, the 1.600 μm line has been detected with a S/N larger than three only in the internal knots, from JI to F. Here, the 1.600 μm/1.644 μm ratio has a minimum close to 0 km s^{-1} velocity and increases, up to a factor of two in knot KL, toward high velocities. In HH1, the inner jet region is not detected due to the high extinction and therefore here we are not observing regions at the jet base, contrary to HH34 and HH46-47. It seems indeed that the velocity dependence of the electron density is different between the FEL regions close to the star and the knots along the jet beam.

A LVC and a HVC from the [Fe II] 1.644 μm line profile of knot KL have been defined. Velocity ranges from ~-80 to ~-22 km s^{-1} and from ~-22 to ~36 km s^{-1} have been selected for the HVC and LVC, respectively. Visual extinction and electron temperature values in each knot were taken from Nisini et al. (2005b). The n_e in the LVC is lower than in the HVC. In the HVC, n_e decreases knot by knot from a value of 10^4 cm^{-3} in knot KL, to 3.8×10^3 cm^{-3} in knot F. On the other hand, in the LVC n_e decreases from 9.8×10^3 cm^{-3} to 8.3×10^3 cm^{-3} in knot KL and JI, respectively. These n_e-values are in agreement with

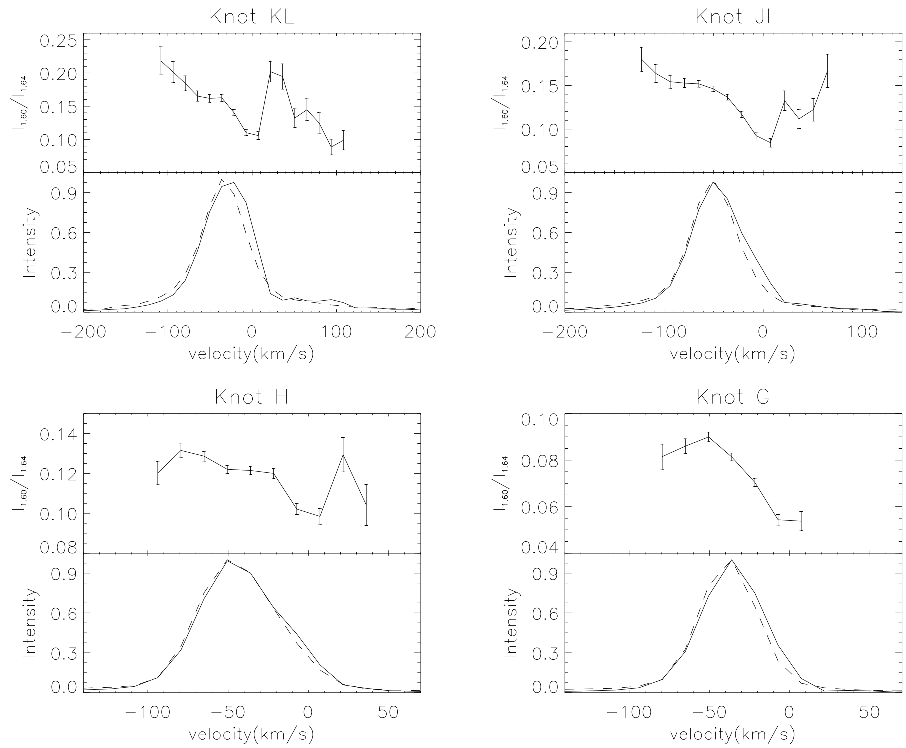

Figure 5.18: Normalised line profiles (lower panels) of the [Fe II] lines 1.644 μm (solid line) and 1.600 μm (dotted line), and their ratio in each velocity channel (upper panel) for different extracted knots along the HH1 jet.

those derived by Nisini et al. (2005b) in velocity integrated spectra.

The presence of two velocity components and the corresponding velocity dependence on electron density, was already found by Solf et al. (1991), who produced a PVD of the electron density in the HH1 jet using the optical [S II] λ 6716/6731 line ratio. They found a blue-shifted component with an electron density of ~4000 cm^{-3} and a slightly red-shifted component having a lower density of ~1000-2000 cm^{-3}. They interpreted the blue-shifted high-density component as due to scattered light originating from a jet region closer to the star, where the density and excitation are higher. This interpretation is, however, not consistent with the IR observations presented here. Indeed, the blue-shifted line component is clearly identifiable as the main jet component, extending at large distances from the exciting source. Moreover, the H_2 PVD (Fig. 5.17) clearly shows the presence of two separate components that cannot be attributed to scattered light contribution. The red-shifted component peaks at the KL position and decreases in intensity further out, while the second blue-shifted component gradually increases its intensity with distance. One possible interpretation is that the red-shifted component belongs to a different jet that intersects the HH1 jet at the KL position. Such a jet could be responsible for the two bright knots designated as HH501 objects by Reipurth et al. (2000a), which are moving away from VLA1 with a proper motion vector inclined with respect to the HH1 jet by ~10°. If we assume the axis of this separate jet equal to the direction of the proper motion vector, the HH501 jet should intersect the HH1 jet at the position of the KL knots.

Mass loss rate

The mass flux rate, $\dot{M}_{jet}$, along the beam of the HH1 jet was recently measured in Nisini et al. (2005b) using different tracers, both optical ([S II], [O I]) and infrared ([Fe II], H_2). This work shows that the mass flux derived directly from the [Fe II] line luminosity, using the measured tangential velocity, is always equal or larger than the $\dot{M}_{jet}$ value derived from the luminosity of the optical atomic tracers in spite of the possibility that part of the iron is still locked on dust grains. This is probably due to the fact that [Fe II] traces a larger fraction of the total flowing mass than the optical lines, as discussed in Nisini et al. (2005b). At the same time, it was found that in this jet the mass flux traced by the H_2 molecular component is negligible with respect to the mass flux due to the atomic component. Taking advantage of the velocity resolved observations available, we now want to measure $\dot{M}_{jet}$ in the different velocity components and examine which of them is transporting more mass in the jet.

The $\dot{M}_{jet}$ value was obtained here from the luminosity of the [Fe II] 1.644 μm line, adopting the relationship $\dot{M} = \mu m_H \times (n_H V) \times v_t / l_t$ (see, Chap. 3 for more details). We have assumed that all iron is ionised, and has a solar abundance of 2.8×10^{-5} (Asplund et al. 2005, i.e., no dust depletion). This latter hypothesis leads to a lower limit of the actual mass flux, since it has been shown that the velocity-averaged, gas-phase iron abundance in the HH1 jet might be only between 20% and 70% of the solar value (Nisini et al. 2005b). The Fe abundance estimate provided in this paper is not used, since the depletion pattern could be different among the LVC and HVC.

To compute the fractional population, we have used the n_e values derived separately for the LV and HV components, while we have assumed a single temperature for both components, equal to the values derived in Nisini et al. (2005b) for the HH1 jet. Tangential velocity values have been derived from the radial velocities assuming an inclination angle i=10° for HH1 (Bally et al. 2002). The resulting tangential velocities of the HVC derived here are listed in Table 5.12. In Table 5.12, the derived values, together with the parameters adopted, are reported

The $\dot{M}_{jet}$ (LVC) is lower than $\dot{M}_{jet}$ (HVC) by a factor of about 6. The mass flux derived for the knot KL is very low. This is likely due to a low estimation of the extinction in this knot, where the 8.3 mag of extinction are the average value in the whole jet region LI. There is some disagreement between the $\dot{M}_{jet}$ derived for HH1 here and in Nisini et al. (2005). The larger discrepancy is being found in the internal JI knots, where Nisini et al. (2005b) report a $\dot{M}_{jet}$ a factor of six larger. Part of the disagreement is due to the different adopted tangential velocity. The largest discrepancy is, however, due to a smaller flux (a factor of three) measured in the ISAAC $0\farcs3$ slit with respect to the $1''$ slit used in Nisini et al. (2005b). This latter measurement might have been contaminated by the presence of the second jet responsible for the redshifted velocity component or the HH1 jet itself might have a diameter wider than $0\farcs3$.

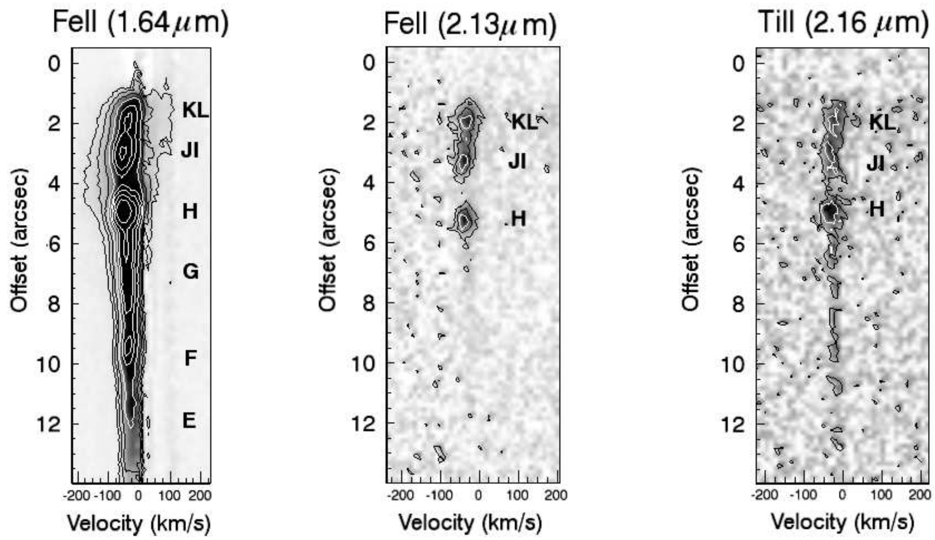

Figure 5.19: PV diagrams for the [Fe II] 1.64μm, 2.13μm and [Ti II] 2.16μm emission lines of the HH1 jet. A position angle of 145° was adopted. Contours show values of 11, 22,...,176σ; 4, 8, 12σ and 3, 6, 12σ, respectively. On the Y-axis the distance from the driving source VLA1 is reported.

It is interesting to compare the derived mass flux rates with the source mass accretion rate, to estimate the $\dot{M}_{jet}/\dot{M}_{acc}$ efficiency in very embedded young sources. There are, however, no measurements of the mass accretion rate in VLA1, the exciting source of the HH1 jet, available. Nevertheless, a rough estimate of this value can be computed by assuming that the source bolometric luminosity ($L_{bol} \sim 50$ L$_{\odot}$, Chini et al. 1997) is entirely due to accretion. Such an assumption is supported by the fact that VLA1 is a known class 0 source. If a stellar mass and radius of 1 M$_{\odot}$ and 3 R$_{\odot}$ is assumed, a $\dot{M}_{acc} \sim 6\,10^{-6}$ M$_{\odot}$ yr^{-1} can be found, which would imply $\dot{M}_{jet}/\dot{M}_{acc} \geq 0.007$. On the other hand, assuming the Fe gas-phase abundance derived by Nisini et al. (2005b) an average value over the brightest knots along HH1 of $\dot{M}_{jet}$~1.1×10^{-7}M$_{\odot}$ yr^{-1} can be estimated. This latter value will lead to $\dot{M}_{jet}/\dot{M}_{acc} \sim 0.02$.

The Ti^{+}/Fe^{+} ratio

Forbidden [Ti II] emission lines have been detected for the first time in HH1. Similar to iron, Ti has a low-ionisation potential, of only 6.82 eV, and thus is expected to be fully ionised in the jet plasma. The two detected lines have excitation energies of the order of 7000 K and critical densities, at 10 000 K, of $\sim 5 \times 10^{4}$ cm^{-3}. Therefore, they have similar excitations conditions with respect to [Fe II] IR lines. Titanium, as iron, is a highly-refractory element, thus the ratio of [Ti II] /[Fe II] lines can give some clue as to the relative gas-phase abundances of Ti and Fe, and, in turn, as to the selective depletion of these elements on dust grains still present in the jet beam. Nisini et al. (2005b) have indeed shown that the gas-phase abundance of Fe in HH1 is lower than the solar value, in particular in the inner jet regions where it is only between 20%-30% of the solar Fe abundance. This indicates that part of the iron is depleted on grains and, consequently, that a significant fraction of dust is present in the jet beam. We can check here if titanium follows the same depletion pattern by comparing the observed [Ti II] 2.160 μm/ [Fe II] 1.644 μm ratio with the value theoretically expected assuming solar abundance values given by Asplund et al. (2005), i.e., $[Fe/Ti]_{\odot} = 354$. For this analysis, a statistical equilibrium calculation have been performed taking the [Ti II] radiative transition rates and electron collisional rates calculated in Bautista et al. (2006, Bautista, private communication), and considering the temperature and density values measured in each HH1 knot in Nisini et al. (2005b). The [Ti II] 2.160 μm/[Fe II] 1.644 μm intensity ratio is rather insensitive to the adopted physical conditions, being of the order of ~ 500 in a temperature range from 9000 to 12 000 K, and density range from 5×10^3 to 1.2×10^4 cm^{-3}. The observed ratios range instead between 150 (knot JI) and 280 (knot G), implying a gas-phase Fe/Ti ratio 2-3 times lower than solar. Thus, there is an overabundance of Ti in the gas phase, with respect to Fe, relative to the solar value. This result indicates that the release of gas-phase elements from dust grains likely follows a selective pattern in which Ti-bearing condensates are more easily destroyed. A large Ti/Fe abundance ratio relative to solar abundances has been observed previously in the ejecta of η Carinae by Bautista et al. (2006) who suggest two different scenarios to explain this finding: either there is a spatial separation between Ti- and Fe-bearing condensates in the same dust grain, which makes the titanium more exposed to evaporation; or Ti-bearing grains are smaller than the Fe-bearing grains and thus more easily destroyed. Studies of this kind, employing a larger number of refractory species, seem therefore promising to constrain the composition and structure of dust grains in different environments.

Table 5.12: $\dot{M}_{jet}$ along the HH1 jet.

Knot	r_t[a] ($''$)	A_v[b] mag	T_e^b (10^3 K)	V_t(HVC)[c] (km s^{-1})	n_e(HVC)[d] (10^3 cm^{-3})	$\dot{M}_{jet}$(HVC)[e] ($M_\odot$ yr^{-1})	V_t(LVC)[c] (km s^{-1})	n_e(LVC))[d] (10^3 cm^{-3})	$\dot{M}_{jet}$(LVC)[e] ($M_\odot$ yr^{-1})
KL	(0.7,2.6)	8.3	11	159	10.6	1.3×10^{-8}	187	9.8	2.3×10^{-9}
JI	(2.6,4.3)	8.3	11	261	9.0	3.6×10^{-8}	187	8.3	3.1×10^{-9}
H	(4.2,6.1)	2.9	9.2	244	8.3	4.4×10^{-8}			
G	(6.1,8.9)	2.0	10.5	198	4.6	2.7×10^{-8}			
F	(8.9,10.7)	2.0	9.8	176	3.8	2.2×10^{-9}			

[a]Distance from VLA1 in arcsec.
[b]Visual extinction and electron temperature from Nisini et al. (2005b).
[c]Tangential velocity assuming an inclination of the jet i=10° to the plane of the sky (Bally et al. 2002).
[d]Electron density for the HV and LV components.
[e]$\dot{M}_{jet}$ for the HV and LV components.

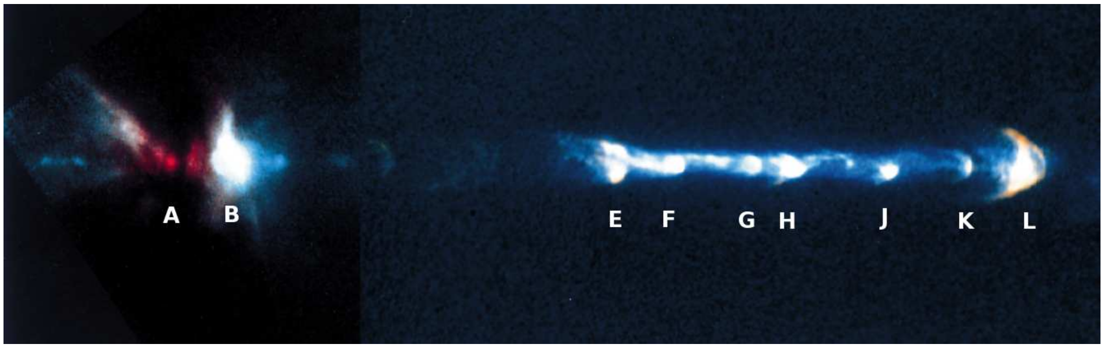

Figure 5.20: HST mosaic image based on NICMOS and WFPC2 images of the HH111 jet. The different knots along the jet are labelled. Figure adapted from Reipurth et al. (1999).

5.4 HH111

The HH111 jet is located in the L1617 cloud in Orion at a distance of ~460 pc, driven by the Class I source IRAS05491+0247. The jet is mainly blue-shifted consisting in a chain of knots showing mini bow-shocks morphology (fig. 5.20). The blue-shifted jet ended with a bow-shock structure at a distance of ~150″ from the source, while only a few knots are detected in the red-shifted jet where a final bow-shock structure is also observed.

Several authors have probed the properties of the outer knots of this flow (Morse et al. 93; Hartigan et al 94). The H_2 kinematics of the jet has been studied in detail by Davis et al. (2001a) by means of echelle spectroscopy, who interpreted the observed line profiles as the result of bow-shock structures along the jet. An analysis of the [Fe II] emission was reported in Nisini et al. (2002) that performed a comparative study with the molecular emission, while Podio et al. (2006) computed a combined optical/IR diagnostics along the jet. In this work, the analysis is mainly concentrated in the section of the jet within ~20″ from the driving source, that have been detected here for the first time. In particular, in the ISAAC H- and K-band spectra studied here, only the [Fe II] 1.600 and 1.644 μm and the H_2 2.122 μm lines have been detected.

5.4.1 [Fe II] and H_2 kinematics

Figure 5.21 shows the PVD of the [Fe II] 1.644 μm line and the normalised line profiles of the H_2 1-0S(1) line along the HH111 jet. The velocity is expressed with respect to the LSR and corrected for a cloud velocity of 8.5 km s^{-1} (Davis et al. 2001a). Distance scales have been measured from the driving source HH111-VLA. The PVD shows the blue-shifted and red-shifted knots along the jet, while only the blue-shifted H_2 line profiles have been reported. The blue-shifted knots from E to O have been named following the nomenclature of Reipurth et al. (1997), while the inner blue- and red-shifted knots that are detected here for the first time, have been named using my own nomenclature (i.e., from B1 to B3, and D1,D2).

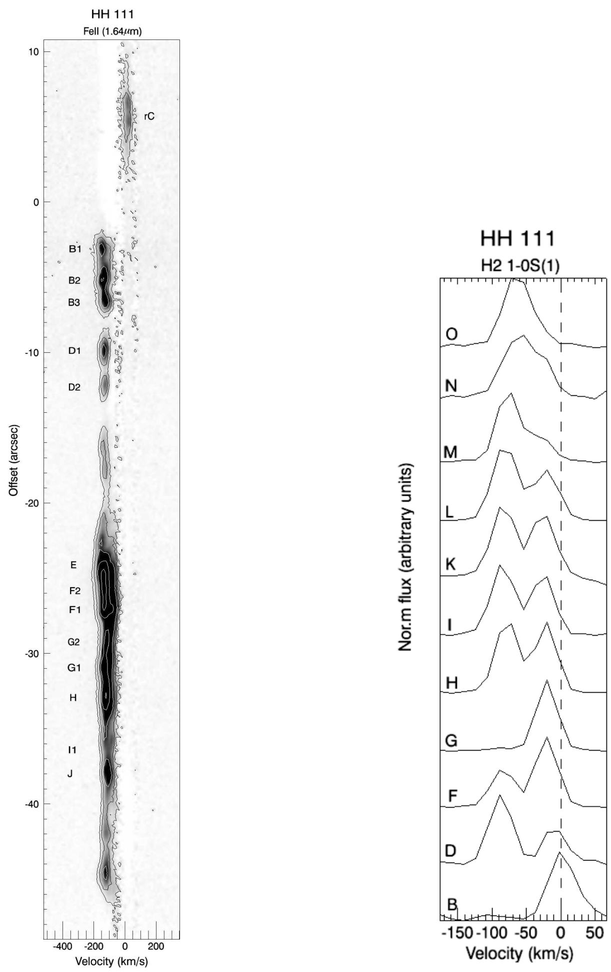

Figure 5.21: (left) PVD for the [Fe II] 1.644 μm line along the HH111 jet. A position angle of 22° was adopted. Contours show values of 5, 15, ..., 405 σ. On the Y-axis the distance from the driving source HH111-VLA is reported. The velocity is expressed with respect to the LSR and corrected for a cloud velocity of 8.5 km s^{-1} (Davis et al. 2001a).(right) Normalised line profiles of the H_2 2.122μm line for different knots along the jet.

The H_2 double-peaked line profiles confirmed the presence of bow-shock structures along the jet as previously reported in Davis et al. (2001a). The deeper images presented here indicate that bow-shocks are also present in knots as close to the source as 2″.

Also [Fe II] lines present double-peaked profiles in the internal knots, while far from the source (from knot E outwards) the lines are mostly single peaked (see, Fig. 5.23). The [Fe II] radial velocities (computed by a Gaussian fit to the line profile) for the inner knots are shown in Table 5.13 together with the line velocity dispersion. Only Gaussian fits to the higher velocity component have been computed. The [Fe II] dispersion velocity roughly decreases from the inner to the outer knots of the jet. In particular, the measured intrinsic FWHM (i.e. deconvolved by the instrumental width) decreases from 39 km s^{-1} in knot B1 to 25.2 km s^{-1} in knot B2. These values imply shocks velocity decreasing from

Table 5.13: Kinematical and physical parameters of the HH111 jet internal knots

Knot	Peak position ($''$)	V (km s^{-1})	ΔV (km s^{-1})	n_e (10^3 cm^{-3})	$\dot{M}_{jet}$ (10^{-9} M$_\odot$ yr^{-1})
B1	2.8	-99.5	39.0	11.0	5.4
B2	4.8	-90.3	40.8	6.6	20.4
B3	6.2	-79.4	39.8	5.0	13.7
D1	9.6	-84.9	35.2	2.8	14.4
D2	11.8	-81.2	25.2	5.8	4.4

~78 km s^{-1} to ~50.4 km s^{-1}.

The [Fe II] radial velocity decreases from knot B1 to knot B3, then increases toward knot D1 and finally decreases again in knot D2. It is known that the HH111 jet presents cyclic variations in velocity at both large and small scales. Raga et al. (2002) have shown that to reproduce the velocity pattern observed at different epochs, a model of variable ejection velocity is needed.

5.4.2 Diagnostics of physical parameters

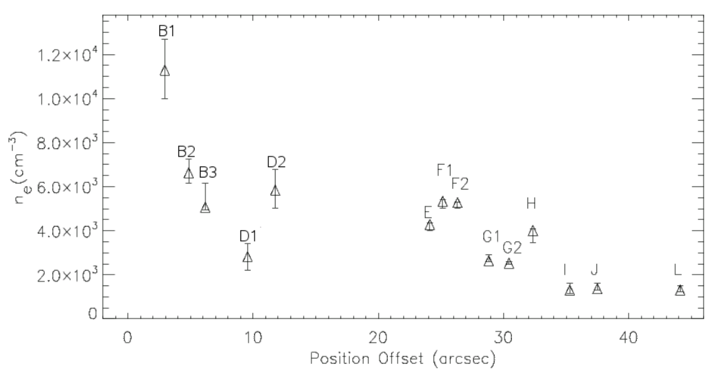

Figure 5.22: Variation of the derived electron density along the HH111 jet.

Electron density

The electron density along the jet was computed from the [Fe II] 1.600/1.644 μm line ratios. Figure 5.23 shows the normalised line profile of the [Fe II] 1.600 μm line and the [Fe II] 1.600/1.644 μm ratio as a function of velocity for the B1 and B2 knots. The line profiles and line ratios of the E and H knots (located far from the central source) have been also reported to be compared with those of the inner knots. Velocities below ~-50 km s^{-1}

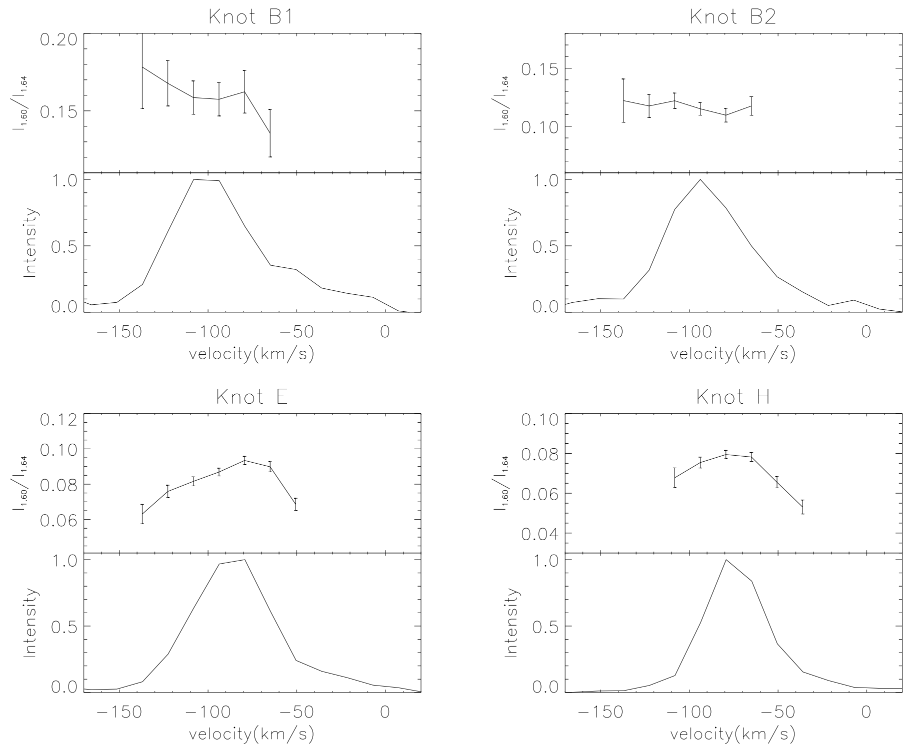

Figure 5.23: Normalised line profile (lower panels) of the [Fe II] 1.600 μm line, and the [Fe II] 1.600/1.644 μm line ratio in each velocity channel (upper panel) for different extracted knots along the HH111 jet.

have not been considered for the n_e analysis due to a strong OH atmospheric residual that contaminates the weak line wing of the [Fe II] 1.644 μm line.

The electron density in the internal knots (from B1 to B4) is approximately constant across the observed velocity channels, showing small increases toward higher velocities. On the contrary, in the external knots (e.g. E and H) the electron density has a maximum corresponding to the line peak and decreases toward the line wings. The n_e values roughly decreases from knot B1 to knot D2 from a value of 11 000 cm^{-3} in knot B1 to 5800 cm^{-3} in knot D2 (Table 5.13). The decrease of n_e as a function of the distance from the source in the HH111 jet was first noted by Podio et al. (2006). They showed that n_e decreases outward from a value of ~4000 cm^{-3} in knot E to 1300 cm^{-3} in knot L. Here this trend is also confirmed for the inner knots with a sharp n_e decrease from knot B1 to Knot B2 (Fig. 5.22).

Mass loss rate

The mass loss rate has been computed from the [Fe II] 1.644 μm line luminosity as explained in Chap. 3 using the eq. 3.19. As in the case of n_e only the $\dot{M}_{jet}$ values for the HVC are reported (Table 5.13). The iron has been considered to be fully ionised and with a solar abundance of 2.8×10^{-5} (Asplund et al. 2005). To compute the fractional population, the n_e values derived in the previous section has been used while a temperature of 10 000 K has been assumed for all the knots. Only measurements for the extinction of the outer knots (from knot E outwards) are available in literature. A visual extinction of 9 mag for knots F and H has been measured by Nisini et al. (2002) and assumed for all the internal knots. The extinction towards the source is expected to be higher that in knot F, thus, the $\dot{M}_{jet}$ value derived here represents only a lower limit. Tangential velocities values have been taken from the study of Hartigan et al. (2001), assuming a constant $v_t \sim 300\,\mathrm{km\,s^{-1}}$ for all the internal knots.

The $\dot{M}_{jet}$ value roughly decreases from the inner to the outer knots from a value of $2.0\times10^{-8} M_\odot\,\mathrm{yr}^{-1}$ in knot B2 to $4.4\times10^{-9} M_\odot\,\mathrm{yr}^{-1}$ in knot D1. The lower value found in the knot B1 is probably due to an extinction higher than assumed. Podio et al. (2006) studied the variation of $\dot{M}_{jet}$ along the external knots (from knot E outwards) of HH111 from the luminosity of optical lines. They also found that $\dot{M}_{jet}$ decreases with the distance from the source. The values they derived are however larger than the ones presented here with a $\dot{M}_{jet}$ from $\sim3\times10^{-8} M_\odot\,\mathrm{yr}^{-1}$ in the knot E to $\sim1\times10^{-8} M_\odot\,\mathrm{yr}^{-1}$ in the knot L. As previously noted, the values reported here represent only lower limits of $\dot{M}_{jet}$: the assumed extinction value of 9 mag derived for knot E (Nisini et al. 2002) probably represents a lower estimation, since extinction is expected to increase towards the source. In addition, an iron gas-phase abundance of ~33% can be derived from the [Fe II]/Paβ line ratio measured by Nisini et al. (2002) for the HH111 jet and assuming that the internal knots have an ionisation fraction and electron temperature as the ones derived by Podio et al. (2006) for the knot E. Then these values are used,together with the n_e derived here, to estimate the iron depletion from the model presented in Nisini et al. (2002) which reproduces different expected [Fe II]/Paβ line ratios as a function of the iron gas-phase abundance. Taking into account the iron depletion a value of $\dot{M}_{jet}\sim2.2\times10^{-8} M_\odot\,\mathrm{yr}^{-1}$ can be found. Assuming an average value $\dot{M}_{acc}\sim6\times10^{-6}$ (Hartigan et al. 1994), a $\dot{M}_{jet}/\dot{M}_{acc}\sim0.002$-$0.003$ can be estimated.

5.5 HH212

The HH212 jet is located in the L1630 cloud in Orion at a distance of ~400 pc. It is driven by a deep embedded Class 0 protostar, IRAS 05413-0104. HH212 is a highly symmetric and collimated bipolar jet with bow-shocks structures at the end of each lobe. The blue-shifted and red-shifted lobes consist in a series of knots distributed at approximately the same distance from the IRAS source (Fig. 5.24). The jet interacts with the surrounding medium driving also a large scale collimated CO outflow (Lee et al. 2006). In the inner region of the jet water masers and SiO emission are also observed (Claussen et al. 1998; Codella et al. 2007). SiO trace an extremely collimated and dense molecular jet (width~500-1000 AU, $n(H_2)\sim10^7\,\mathrm{cm}^{-3}$) located within 1″ from the driving source, in a region of high obscuration where H_2 is not detected (Codella et al. 2007; Cabrit et al. 2007).

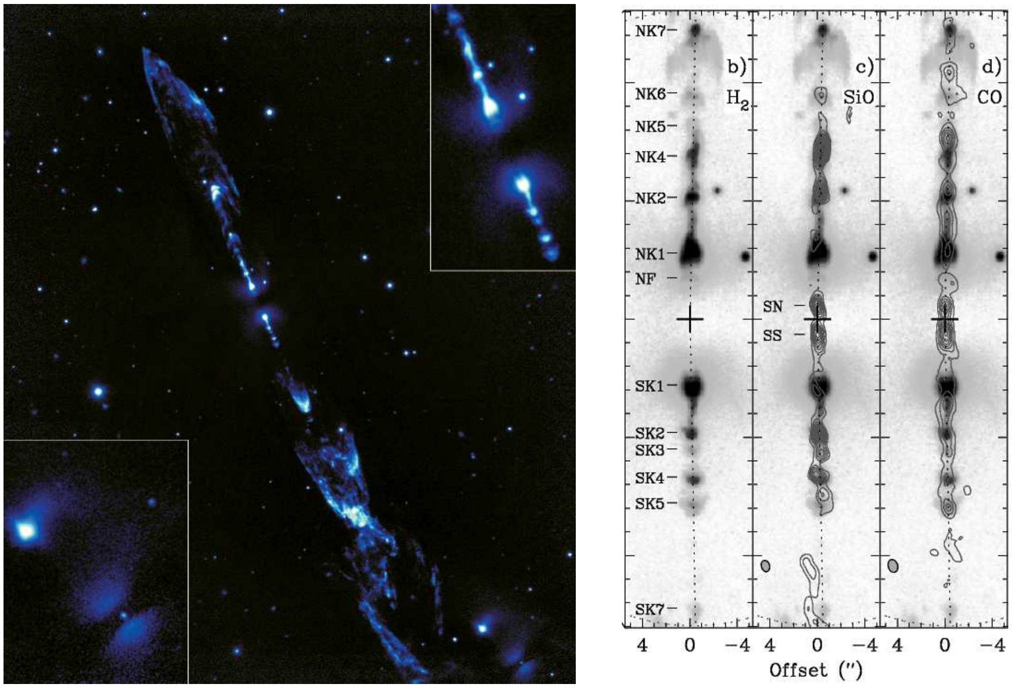

Figure 5.24: (Left) ISAAC H_2 image of the HH212 jet. North is up and left is East. The two insets in the corners show the details of the inner jet region and a south-west bipolar nebula. Figure taken from McCaughrean et al. (2002). (Right) The H_2 image of the inner jet where the knots have been labelled is shown together with the contours of the SiO (central panel) and CO (right panel) emission plotted on top of the H_2 image. Figure taken from (Codella et al. 2007).

5.5.1 Detected lines

A list of the lines detected in the H- and K-band spectral segments and their identification can be found in Table 5.14. Among the [Fe II] lines, only the 1.600 μm and 1.644 μm transitions have been detected in the knots closer to the source (named NK1 and SK1), testifying for the low excitation conditions of this jet. The [Si I] 1.646 μm line has been detected here as a first time in a jet environment, although it should be the brightest [Si I] transition in the NIR, with an excitation energy of E_{up}=6298 cm^{-1}. The ionisation potential of Si is relatively low (8.2 eV), although higher than that of the Fe (7.9 eV). [Si I] can be, therefore, expected in regions where the shock excitation is low, such as C-shocks where a small fraction of molecules can still be partially dissociated. The [Si I] emission appears brighter in the SK1 indicating lower excitation conditions in this knot. Finally, bright H_2 lines from the first three vibrational levels are detected all along the jet.

5.5.2 [Fe II] and H_2 kinematics

The PVDs of the H_2 2.122 μm and [Fe II] 1.644 μm lines are reported in Figs. 5.25 and 5.26 for the blue- and red-shifted lobes of the HH212 jet. The driving source IRAS05413-0104 is not detected in the spectral images, but it is located symmetrically in between the NK1

Table 5.14: List of detected lines along the HH212 jet

Line id.	λ^a
[Fe II]$a^4D_{3/2} - a^4F_{7/2}$	1.5999
[Fe II]$a^4D_{7/2} - a^4F_{9/2}$	1.6440
[Si I]$a^1D_2 - a^3P_2$	1.6459
H_2 1-0 S(1)	2.1218
H_2 2-1 S(2)	2.1542
H_2 3-2S(3)	2.2014
H_2 3-2S(4)	2.1280

[a]Vacuum wavelengths in microns.

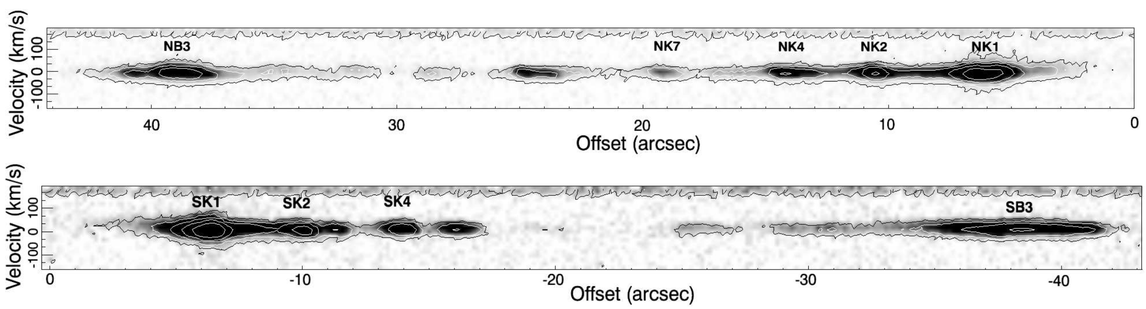

Figure 5.25: PVDs for the H_2 2.122 μm line along the blue-shifted (top) and red-shifted (bottom) lobes of the HH212 jet. A position angle of 22° was adopted. Contours show values of 10, 30,…, 810 σ in both lobes. On the x-axis the distance from the central source is reported.

and SK1 knots (Lee et al. 2006).

A detailed study of the H_2 kinematics of HH212 has been already performed by Davis et al. (2000a). Here, the analysis is limited to the internal knot NK1 and SK1, where the atomic emission has been detected.

The radial velocities and FWHM of the [Fe II], H_2 and [Si I] lines are reported in Table 5.15. The velocities and FWHM of each knot have been measured by a Gaussian fit to the line profiles and are expressed with respect to the LSR corrected by a cloud velocity of 1.6 km s^{-1} (Wiseman et al. 2001). All the profiles appear single-peaked and well reproduced by a single Gaussian component. The radial velocities in SK1 and NK1 are around 4 km s^{-1} and -18 km s^{-1}, in all the observed lines. Davis et al. (2000a) measured the H_2 2.122 μm line radial velocities of these knots through echelle spectroscopy using three different slits positions along the jet. They found H_2 velocities ranging from -5.5 km s^{-1} to -3.8 km s^{-1} in the knot NK1 and from +4.0 km s^{-1} to +6.3 km s^{-1} in the knot SK1. These values agrees fairly well with the radial velocities measured here for the knot SK1, while they are ~10 km s^{-1} lower than the measured values for the knot NK1. The differences between the radial velocities reported by Davis et al. (2000a) for this knot and

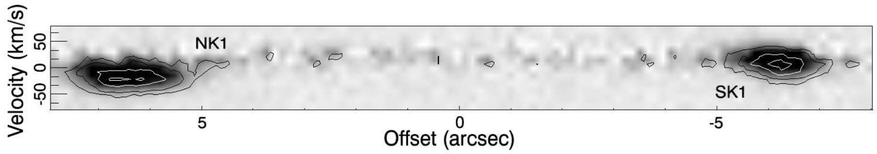

Figure 5.26: PVD for the [Fe II] 1.644 μm line along the HH212 jet. A position angle of 20° was adopted. Contours show values of 30, 60, 120 and 175 σ.

Table 5.15: Radial velocities along the HH212 jet.

Knot	[Fe II] 1.644 μm		H_2 2.122 μm		[Si I] 1.646 μm	
	V^a (km s^{-1})	FWHM (km s^{-1})	V^a (km s^{-1})	FWHM (km s^{-1})	V^a (km s^{-1})	FWHM (km s^{-1})
SK1	4	23	4.6	23	4	30
NK1	-18	34	-10(-5.6)	23	-18	

[a]Radial velocities with respect to the LSR and correct for a cloud velocity of 1.6 km s^{-1} (Wiseman et al. 2001)

the ones measured in this work may arise from a different orientation of the slit along the HH212. Indeed, measurements of the transverse H_2 line profiles of NK1 (i.e. with the slit located perpendicular to the jet axis) at high resolution (R~50 000~6 km s^{-1}) revealed that this knot is double peaked with radial velocities varying from ~-6 km s^{-1} to ~-11 km s^{-1} (cor 2009).

5.5.3 Diagnostics of physical parameters

Electron density

The electron density has been derived from the [Fe II] 1.600/1.644 μm line ratio. In Fig. 5.27 the normalised line profiles of the [Fe II] 1.644 and 1.600 μm are represented together with the 1.600/1.644 μm ratio. For both knots, a decrease in n_e from higher to lower velocities is observed. In the knot NK1, n_e roughly varies from a value of 8400^{+2600}_{-2000} cm^{-3} at -50.0 km s^{-1} to 3800^{+800}_{-700} cm^{-3} at -6.6 km s^{-1}, while in knot SK1 n_e varies from a value of 8400^{+2600}_{-2100} cm^{-3} at -21.1 km s^{-1} to 2400^{+700}_{-600} cm^{-3} at +36.8 km s^{-1}. The n_e behaviour observed is consistent with a model of bow-shock. In such a model assuming constant total density across the bow, the higher value of the electron density should be observed at the high velocity component where the most energetic shocks occur (Indebetouw & Noriega-Crespo 1995).

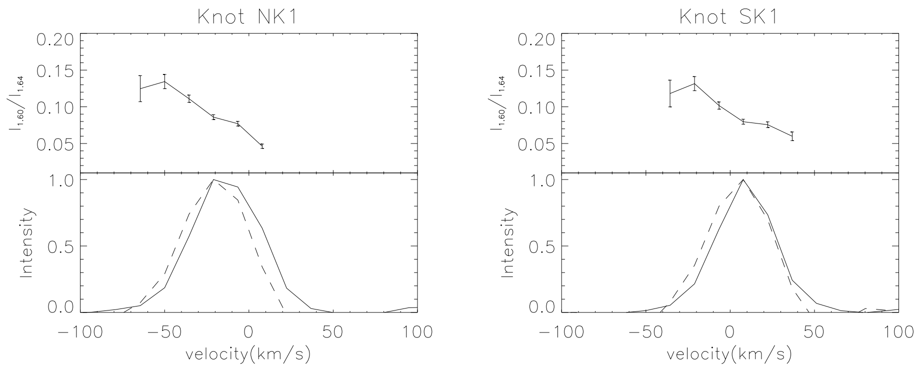

Figure 5.27: Normalised line profiles (lower panels) of the [Fe II] 1.644 μm (solid line) and 1.600 μm (dotted line) lines, and their ratio in each velocity channel (upper panel) for different extracted knots along the HH212 jet.

Table 5.16: $\dot{M}_{jet}$ values along the HH212 jet.

Knot	A_V (mag)	V_t (km s^{-1})	$\dot{M}_{jet}$([Fe II]) (10^{-9} M$_\odot$ yr^{-1})	T(H_2) (10^3 K)	V_t (km s^{-1})	$\dot{M}_{jet}$(H_2) (10^{-9} M$_\odot$ yr^{-1})
SK1	12[a]	46	0.6	2.9	46	6.5
NK1	11[a]	206	3.3	2.8	114	11.7

[a]Visual extinction from Caratti o Garatti et al. (2006)

Mass loss rate

The mass loss rate for the NK1 and SK1 knots of the HH212 jet has been derived from both [Fe II] 1.644 μm and H_2 1-0S(1) line luminosities according to the procedure described in Chap. 3 and reported in Table 5.16 together with the assumed parameters.

Tangential velocities in each knot have been derived from the observed H_2 and [Fe II] radial velocities assuming an inclination angle of the jet of ~5° (Claussen et al. 1998). Visual extinctions and H_2 temperatures have been taken from Caratti o Garatti et al. (2006), while for [Fe II] a temperature of 10 000 K and an average n_e~5000 cm^{-3} have been considered.

Contrary to the other investigated jets, in HH212 $\dot{M}_{H_2}$ is a factor between 3 and 10 higher than the mass loss rate of the atomic component. This result reinforces the evidence that the excitation conditions in this jet are very low and most of the mass is transported by the molecular component.

5.6 Discussion

5.6.1 The base of Class I jets: HH34 and HH46-47

Comparison between the properties of the HH34 and HH46-47 jets near the exciting source

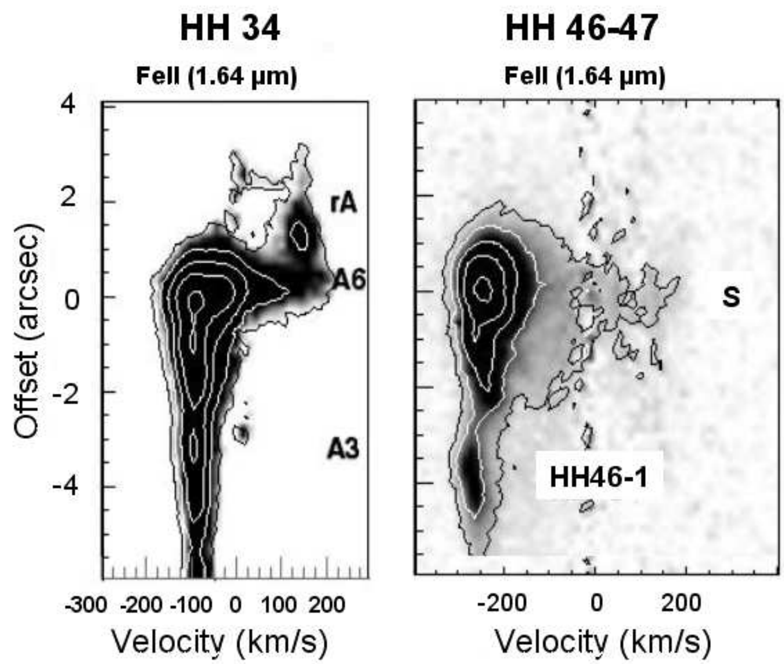

Figure 5.28: PVDs of the [Fe II] 1.644 μm line for the HH34 and HH46-47 jets.

The HH34 and HH46-47 jets present a similar behaviour as regards to their atomic component in the inner region, as shown in Fig. 5.28 where the PVDs of the [Fe II] 1.644 μm line for both jets are reported. Within $\sim$2″ from the central source, the [Fe II] lines broaden and emission at lower velocities, down to 0 km s^{-1} appears. Inside $\sim$1″ emission is also detected at positive velocities for both jets. In both the PVDs the LVC reaches distances up to $\sim$1000 AU.

At variance with [Fe II], the H_2 PVDs of the two objects show a different behaviour. In HH34 the H_2 PVD shows spatially- and kinematically-separated LVC and HVC, and only the LVC is visible down to the central source. In HH46-47,on the contrary, a single velocity component near the source is detected.

With respect to the physical properties, the variation of electron density and mass ejection flux as a function of the velocity is the same for both objects. Indeed, the electron density of the LVC is higher than the electron density of the HVC. The mass ejection flux is, however, mainly carried out by the HVC.

There is therefore a large similarity between the properties of the FEL region in these

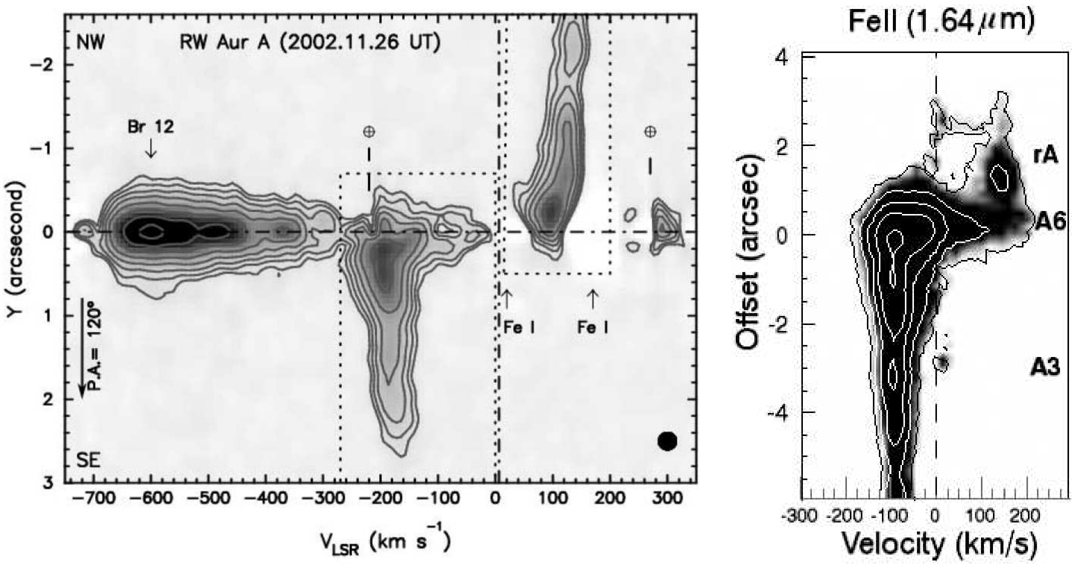

Figure 5.29: (left) Continuum-subtracted PVD of the [Fe II] 1.644 μm line for the RW Aur jet. The [Fe II] emission features are indicated by dotted lines. Figure taken from Pyo et al. (2006). (right) Continuum-subtracted PVD of the [Fe II] 1.644 μm line for the HH34 jet.

tow Class I objects: further observations on a larger sample of sources are, however, needed to see if these properties characterise all the Class I jets.

Comparison with TTauri jets

The [Fe II] PVDs for the HH34 and HH46-47 jets are also similar to the ones observed in some CTTSs, such as HL Tau and RW Aurigae (Pyo et al. 2006). As an example, Fig. 5.29 shows the [Fe II] 1.644 μm PVDs of the RW Aur and HH34 jets. In TTauri FELs one usually observes two separated peaks spatially located at different offsets from the central source, the HVC being commonly displaced further downstream (e.g. Hirth et al. 1997). In HH34 and HH46-47, at variance, the HVC has a peak in the on-source position. This behaviour could, however, be due to the lower spatial resolution of the observations presented here as a consequence of the larger distance of HH34 and HH46-47 with respect to other studied T Tauri stars. In CTT jets, the LVC is usually confined within $d \leq 200$ AU from the source. In HH34 and HH46-47, on the contrary, the LVC persists at larger distances, up to 1000-2000 AU, thus, the spatial scale between CTT jets and the Class I jets studied here are very different. Therefore, it may be that the LVC of the HH34 and HH46-47 jet has a different origin than in the CTTS case.

Differences in the excitation conditions of the various velocity components have been measured in jets from CTTSs. This kind of study has, however, never been attempted before for jets from Class I stars. The results found for the dependence of the electron density on velocity are in agreement with what is found in the FEL regions of T Tauri stars, where the emission component associated with the low-velocity gas is denser and less excited than the HVC (Hamann et al. 1994; Hartigan et al. 1995). In such studies, the LVC was not spatially resolved and the different values for n_e found between the HVC and LVC were interpreted assuming that the LVC originates from a dense compact region close to the disc surface, while the HVC is associated with a more extended high-velocity jet displaced further out. Such an interpretation was supported by the spatial offset from the central source often found between the two components of the forbidden lines detected in spatially-unresolved spectra of T Tauri stars. Spatially-resolved measurements of the electron density in the HVC and LVC have been performed in DG Tau by Bacciotti et al. (2000) and Lavalley-Fouquet et al. (2000). In this case, at variance with HH34 and HH46-47, the electron density has been found to increase with velocity, up to a distance of ~ 450 AU from the central source. On the other hand, in the DG Tau micro-jet the total density in the LVC is higher than in the HVC because of the much lower ionisation fraction. Therefore, the density structure in the Class I objects studied here and in the T Tauri stars might be similar, but they differ in the excitation conditions.

In jets from CTTSs, Hartigan et al. (1995) have already shown that the mass flux in the LVC should be lower than in the HVC: from the analysis of spatially not resolved optical spectra, they concluded that the LVC in jets from CTT stars could be responsible for carrying the majority of mass and momentum only if the emitting region were smaller than 1 AU.

Comparison with MHD models

Magneto-centrifugal jet launching models, such as the disc-wind and X-wind models (Ferreira 1997; Shang et al. 1998; Garcia et al. 2001a; Pudritz et al. 2007) predict the presence of a broad velocity range close to the source position, corresponding to the un-collimated outer streamlines. In both these models, the LVC is, however, confined to a relatively small region at $d \leq 200$ AU from the source. Thus, the LV gas observed farther away needs to be locally heated, probably by shocks. Within 400 AU from the HH34 IRS and HH47 IRS sources the velocity decreases almost continuously from its peak reaching redshifted velocities.

We can compare the observed kinematical signatures in this region with those in the synthetic PVDs available for the different jet models. Synthetic PV diagrams from X-wind models have been constructed for optical [S II] and [O I] lines (Shang et al. 1998), while [Fe II] PV plots have been presented by Pesenti et al. (2004) for the cold disc-wind model of Garcia et al. (2001b) (see, Fig. 5.30).

The cold disc-wind synthetic PVD presented in Pesenti et al. (2004) was constructed assuming a spatial sampling and spectral resolution similar to those of our observations. This diagram predicts [Fe II] 1.644 μm maximum (de-projected) velocities of the order of $-700\,\mathrm{km\,s^{-1}}$. In contrast, the maximum velocity measured in HH34 and HH46-47 from the FWZI in knot A6 and S is ~ -400 and $\sim -500\,\mathrm{km\,s^{-1}}$. However, the observed range of line of sight velocities predicted by disc-wind models significantly depends on the assumed range of launching radii and magnetic lever arm parameter ($\lambda = (r_A/r_0)^2$, with r_A and r_0, the Alfvén and launch radii, respectively). Ferreira et al. (2006) have shown that

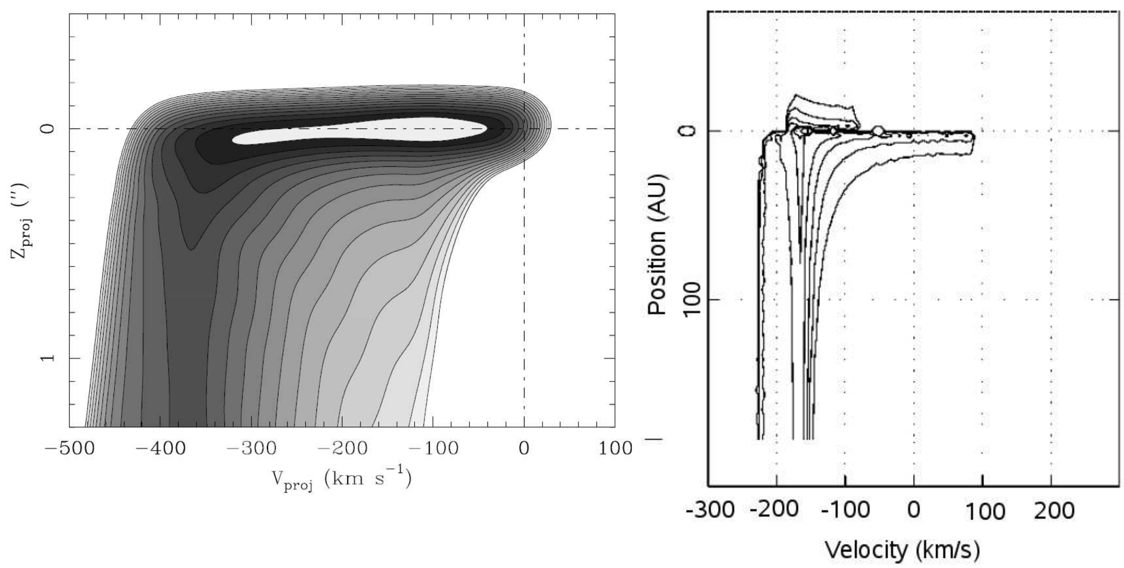

Figure 5.30: (left) Predicted PVD of the [Fe II] 1.644 μm line from the cold disc-wind model, assuming an inclination angle i=45°. Figure taken from Pesenti et al. (2003). (right) Predicted PVD of the [S II] λ 6731 emission line from the X-wind model assuming an inclination angle of i=30°. Figure adapted from from Shang et al. (1998).

cold disc-wind models in general predict overly large line of sight velocities with respect to the observations because they have overly large magnetic lever arms of the order of 50 or higher. On the other hand, warm disc wind solutions with magnetic lever arms in the range 2-25 predict lower poloidal velocities, in better agreement with observations (Ferreira et al. 2006). In particular, the measured poloidal velocities for HH34 and HH46-47 are of the order of 250 km s^{-1} and 350 km s^{-1}, estimated from the observed peak radial velocity corrected for the inclination angle, would imply a value of λ in the range 4-8, for launching radii in the range 0.07-0.15 AU (see, Fig. 5.31).

X-wind models predict a narrower spread in velocity, which agrees with our observed range, taking into account the inclination angle of 23° and 34° of the HH34 and HH46-47 flows. In such models the intermediate and low-velocity components are, however, predicted to be present only in the inner ~ 30 AU from the central source, in contrast with observations. In addition, the synthetic PVDs constructed by Shang et al. (1998) do not include heating processes in the calculation, but assume a uniform ionisation fraction and electron temperature.

Another interesting feature predicted by X-wind models is the presence of a significant redshifted emission at the stellar position similar to the one observed in HH34 and HH46-47. These are the first cases where such a feature is observed, and indeed the absence of the redshifted emission in the PVD of other CTT jets was taken as an indication to rule out the X-wind model for these sources (Takami et al. 2006). In HH34 and HH46-47, such redshifted emission was not detected in previous observations probably because of the lack of sensitivity.

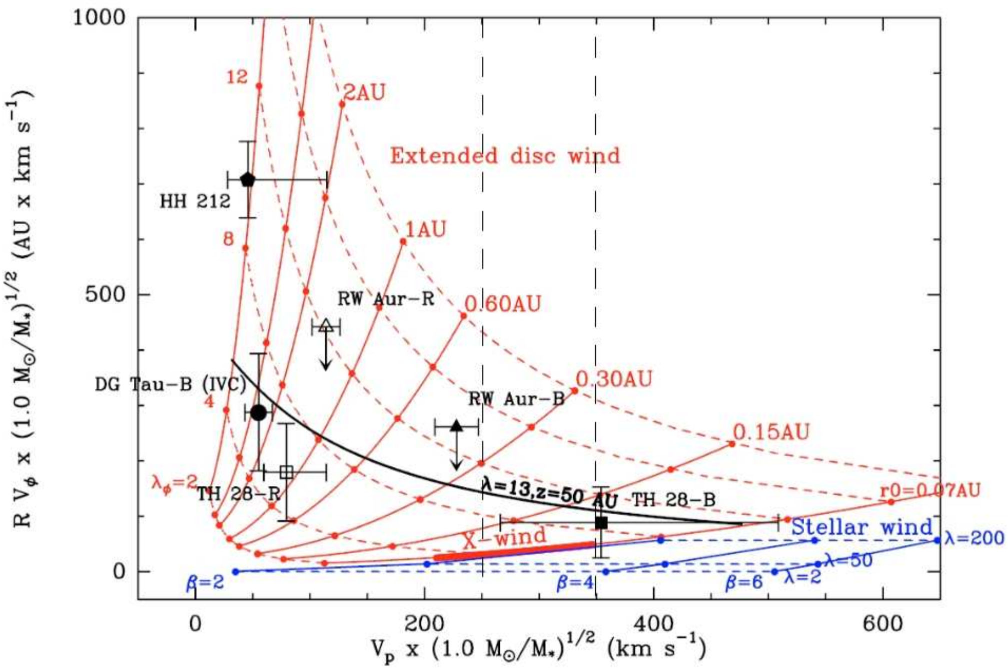

Figure 5.31: Comparison of predicted specific angular momentum vs. poloidal velocities for all types of stationary MHD models. Solid lines represent the relationship between rv_ϕ and v_p: in red for disc-winds assuming a fixed launching radius r_0, in blue for stellar winds. Dashed lines indicates curves of constant magnetic lever arm in the disc wind case. The position of the X-wind solution for a fixed $r_0 = 0.07$ AU is indicated by a thick red line. Observational points for several TTauri jets are reported.

In conclusion, a qualitative comparison based on the available synthetic PVDs indicates that both X-wind and disc-wind models reproduce the kinematics observed in the HH34 and HH46-47 jets at their base, while none of them can reproduce the large scale LVC observed at very large distances from the source. A more quantitative comparison would require the construction of [Fe II] synthetic PVDs exploring a larger range of parameters and heating mechanisms.

The other observational finding in this study that can be compared to model predictions is the dependence of the electron density and mass flux on velocity. The fact that the electron density in the LVC is higher than in the HVC is neither consistent with the available X-wind nor with disc-wind models. In disc-wind models, the high velocity and dense gas ejected in the inner streamlines is bracketed by the slower gas at lower density originating from more external and less excited regions of the disc. Cabrit et al. (1999) show, in fact, that the electron density increases toward the axis of the flow. Similarly, in X-wind models the electron density and ionisation decreases with the distance from the central axis (Shu et al. 1995). It should be pointed out that the main parameter predicted by different jet launching models is not the electron density, but the total density and its variation with velocity. Therefore, the found inconsistency may stem from an incorrect modelling of the excitation mechanism responsible for the gas ionisation, not necessarily from a wrong underlying MHD solution.

An alternative possibility is that the LVC represents gas not directly ejected in the jet, but dense ambient gas entrained by the high-velocity collimated jet. Observations at higher spatial resolution would be needed to perform an analysis similar to that presented here for the gas within 200 AU from the source. This would allow us to isolate as much as possible the component of gas ejected at low velocity in the jet itself.

H_2 HVC and LVC in HH34

MHEL regions (see Sect. 2.1.3) within a few hundred AU from the driving source has been detected in a dozen outflows (Davis et al. 2001b). With respect to FEL regions, the gas components associated with MHELs usually show lower radial velocities and velocity spreads.

In light of these previous findings, there are two scenarios that can explain the characteristics of the LVC in the H_2 lines of HH34. The first hypothesis is that such a low-velocity warm molecular gas is excited by oblique shocks occurring at the wall of a cavity created by the interaction of a wide angle wind with the ambient medium. Indeed, the large reflection nebulosity associated with HH34 IRS suggests the presence of a cavity illuminated by the central source. The second possibility is that the H_2 gas originates from the external layers of a disc-wind. Magneto-centrifugal wind models, in fact, predict that the fast collimated inner component coexists with a slow and wide external component at low excitation. In a previous study, the H_2 emission observed within 100 AU from DG Tau has been interpreted by Takami et al. (2004) in this scenario. Modelling of the H_2 molecule survival and excitation in disc-winds is, however, needed to support this interpretation.

The fact that the H_2 HVC is observed only from a distance of $\sim 2''$ from the star, at variance with [Fe II], may indicate that the molecular gas does not survive in conditions of highly-excited gas constituting the high-velocity inner jet region. In this inner region, the jet is probably travelling inside a low-density cavity and thus no molecular material is present to be entrained by the fast moving flow. Reformation of H_2 in the jet could be at the origin of the H_2 HVC seen further out: the dust in the jet is not fully destroyed (Podio et al. 2006) and thus the H_2 molecules can be formed again once the physical conditions become favourable for the molecule survival. Excitation in the wings of mini-bow shocks along the flow can be another possible explanation for the H_2 HVC, although the high radial velocity of H_2 close to the velocity of the atomic gas, is not supported by H_2 excitation models in bow-shocks (Flower et al. 2003).

Constraining MHD models from dust depletion measurements: HH46-47

The study of the presence of dust grains along the jet beams can be used, in addition to the study presented above, to constrain MHD models.

Dust grains of the ambient medium are expected to be completely destroyed by the passage of the initial bow-shock front which average velocity is higher than 100 km s^{-1} (Draine 2003). Subsequent shocks along the jet beam should therefore occur in a dust

Table 5.17: Summary of the average physical properties in the considered sample of Class 0/I objects.

Jet	Class	V_s (km s^{-1})	n_e[a] (cm^{-3})	$\dot{M}_{jet}$[b] (10^{-8} M$_\odot$ yr^{-1})	$\dot{M}_{jet}/\dot{M}_{acc}$
HH1	0	78	5600	2.4-11.0	0.007-0.02
HH111	0	66	6250	$\gtrsim$1.2-2.2[c]	$\gtrsim$0.003
HH212	0	57	5000	0.2 (0.9)[d]	$\gtrsim$0.0004 (0.001)[d]
HH34	I	82	2600	5.6-20.0	0.01-0.03
HH46-47	I	94	3610	3.7-13.0	0.1-0.9

[a]Electron density derived from [Fe II] line ratios.

[b]Range of mass flux rates derived from [Fe II] luminosities. Lower values are measured assuming an iron solar abundance, while upper values have been derived from the iron gas-phase abundance derived in Nisini et al. (2005b) and Podio et al. (2006).

[c]Upper value derived assuming that only ~33% of the iron is in gaseous form. This result represents a lower limit since the extinction towards the source is probably larger than the one assumed here, see Sect. 5.4.2

[d]In parenthesis, the average $\dot{M}_{H_2}$ and the $\dot{M}_{H_2}/\dot{M}_{acc}$ values are reported

free environment. I have, however, shown that in HH46-47 around 88% of iron within 450 pc from the source is still,l depleted on grains. This value decreases to ~58% in the external knots.

After the passage of the shock front the time required for grains to be reformed is larger than 10^6 yr. The jet employs, however, around 10^3-10^4 yr to travel from the central source to the final bow-shock. This means that grains cannot be formed along the jet beam. In addition, it is unlikely that they come from entrainment material from the surrounding media, since the depletion decreases from the inner to the external region of the jet. Therefore, the larger amount of grains near the source may suggest that they have been removed from the accretion disc and transported through the jet.

The inner region of accretion discs is expected to be composed only by optically thin gas: the radiation of the central protostar destroys the dust grains up to a distance named the dust evaporation radius. For Class 0/I objects this radius is expected to be around 0.1 AU from the protostar (Isella & Natta 2005). This means that a Class 0/I jet cannot transport dust from the disc if the jet is launched from a region closer than ~0.1 AU to the central object. This fact favours the presence of a disc-wind (alone or combined with other jet launching mechanism, see Chap. 2.1.1) as the mechanism responsible for the jet launching and the extraction of dust from the disc.

5.6.2 General properties of Class 0/I jets

Although the sample of Class 0/I objects studied in this thesis is too limited to represent a statistically significant sample, it can be used to evidence any general trend of the measured properties and probe any evolutionary effect in the jet excitation and dynamics. In Table 5.17 a summary of the main parameters derived in this thesis (averaged over the brightest knots of each jet) is reported.

All the objects presented here show both [Fe II] and H_2 emission and the ratio between atomic/molecular emission is independently of their evolutionary state. Observations of other Class I jets in the near-IR (e.g., Davis et al. 2003; Takami et al. 2006) confirm this trend and suggest that the jet excitation probably does not depend on the age of the source but more on the characteristics of the ambient medium in which jets propagates. In the observed Class 0 jets the electron density is higher than in the Class I. This fact probably reflect the higher total density in the environments of these very young objects. Shock velocities are always high, with values ranging between ~60-100 km s^{-1}. Such a high shock velocities justify the presence of strong Fe emission in all the investigated jets, since only shocks with speed $\gtrsim$50 km s^{-1} are able to dissociate molecules and ionise a significant fraction of gas.

For each of the objects the range of mass flux rate transported along the flow has been measured. This range has been inferred from the luminosity of [Fe II] lines assuming a solar iron abundance (lower limit) and an iron gas-phase abundance (upper limit). The $\dot{M}_{jet}$ values oscillated between 2×10^{-8} M$_\odot$ yr^{-1} and 2×10^{-7}M$_\odot$ yr^{-1}. These values are on average larger than the observed in CTTS, with the exception of highly active TTauri stars such as DGTau and RwAur. The HH212 jet shows, however, much lower values of the order of 2×10^{-9} M$_\odot$ yr^{-1}, and, at variance with the other studied objects, the molecular component transports the bulk of the mass with an average value of $\dot{M}_{H_2}$~9×10^{-9}. Therefore, either the jet is mainly molecular or most of the iron along the flow is located in grains. Nevertheless, the $\dot{M}_{H_2}$ value is smaller than the $\dot{M}_{jet}$ found in the other objects. This probably indicates that most of the mass is transported by the cold molecular component not traced in the NIR, such as SiO and CO. Indeed, Codella et al. (2007) derived a mass loss rate from sub-millimetric observations (thus tracing the coldest component of the jet) of ~1-2×10^{-6} M$_\odot$ yr^{-1}.

The mass accretion rates derived in literature for the driving sources of the sample give rise to $\dot{M}_{jet}/\dot{M}_{acc}$ ratios between 0.02-0.03, roughly the same value found in CTTS. This result suggests that the same launching mechanism is present over mass accretion rates ranging several magnitude orders. The large mass ejection to accretion ratio found in HH46-47 ($\dot{M}_{jet}/\dot{M}_{acc}$~0.9) is probably related to the fact that the driving source, HH46IRS, is actually a binary system. As discussed in Antoniucci et al. (2008), there is no certain on which the sources are driving the jet and the luminosity contribution of the companion to the real source is unknown. Therefore the estimation of $\dot{M}_{acc}$ for this system is probably affected by several uncertainties regarding the total luminosity of the source.

Chapter 6

Probing the mass accretion in Class I protostars

The mass accretion rate in young stellar objects represents a critical parameter to understand the star formation process. Although the accretion properties of optically visible CTTS have been widely studied using different methods (see Chap. 2), very few studies have been done so far about the accretion properties of the less evolved Class I sources. As discussed previously in Chap. 2, recent studies show that there is a large spread in the measured accretion luminosities of embedded objects, with values ranging from a few percentage to a 80% of the total bolometric luminosity. In this chapter, the accretion properties of our sample of Class I sources in Ophiucus are studied. This study allows us to verify the paradigm of the proposed evolutionary sequence for young stars according to which Class I are actively accreting objects less evolved than CTTS.

This chapter is organised as follows: in Sect. 6.1 and 6.1.1, I will present the ISAAC spectra obtained in the sample (see Chap. 4) discuss the different detected spectral features. In Sect. 6.2, the method to derive the mass accretion rate from the Brγ luminosity will be illustrated, and a discussion of the obtained results will be done.

6.1 Detected lines

The emission lines detected in the VLT-ISAAC spectra of the sample of Class I sources (see, Chap. 4) are reported in Table 6.2, while from Fig. 6.1 to Fig. 6.8 the spectra of the sources in different bands are shown, with the exception of IRS43 where only Brγ emission has been detected.

Five sources of the sample (WL12, IRS54, WL17 and YLW16A) show bright [Fe II] and H_2 emission lines (see, Figs. 6.1, 6.4, 6.5 and 6.8). The detection of [Fe II] and H_2 emission evidence the presence of an atomic/molecular jet at the base of these sources. In WL17 and WL15 only H_2 emission has been detected. This indicates that in these sources the line emission region is characterised by high densities and low excitation conditions.

In addition to H_2 and [Fe II] emission lines, also several HI permitted emission lines

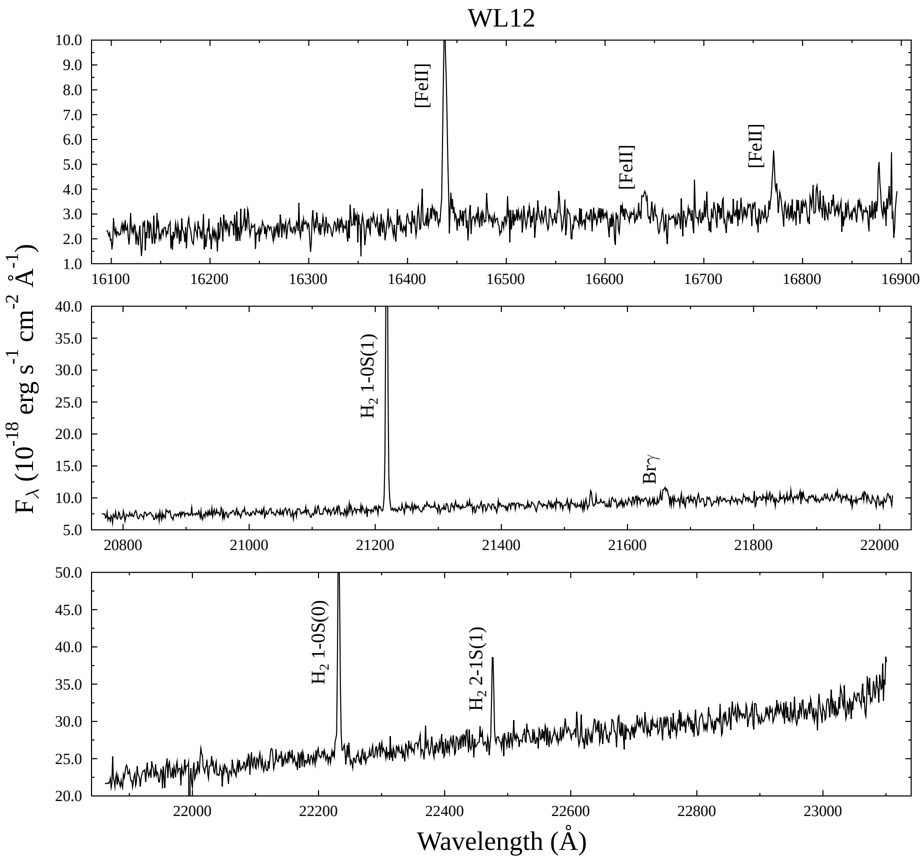

Figure 6.1: H- and K-band spectra of WL12.

have been detected. These lines are mainly observed at the source position and their origin is not clear. They trace high density gas excited at high temperatures either in the accretion region or at the base of protostellar jets. The main detected HI transitions are recombination lines of the Brackett series. In addition, in four of the sources (WL16, WL17, IRS54 and WL18) also emission from the Paβ line is detected. The line profiles of the Paβ and Brγ lines are symmetric in all the sources with the exception of WL16 (Fig. 6.1) where all the detected Brackett lines and the Paβ line show inverse P-Cygni profiles, indicative of matter in infall motion towards the object. In this source also bright CO emission from different vibrational band-heads in the 2.3 μm region is detected. The CO 2.3 μm feature is usually interpreted as coming from an inner gaseous disc, heated at temperatures of ~2000 K or more by accretion. All these evidences suggest that WL16 should be a source in a very active accretion phase.

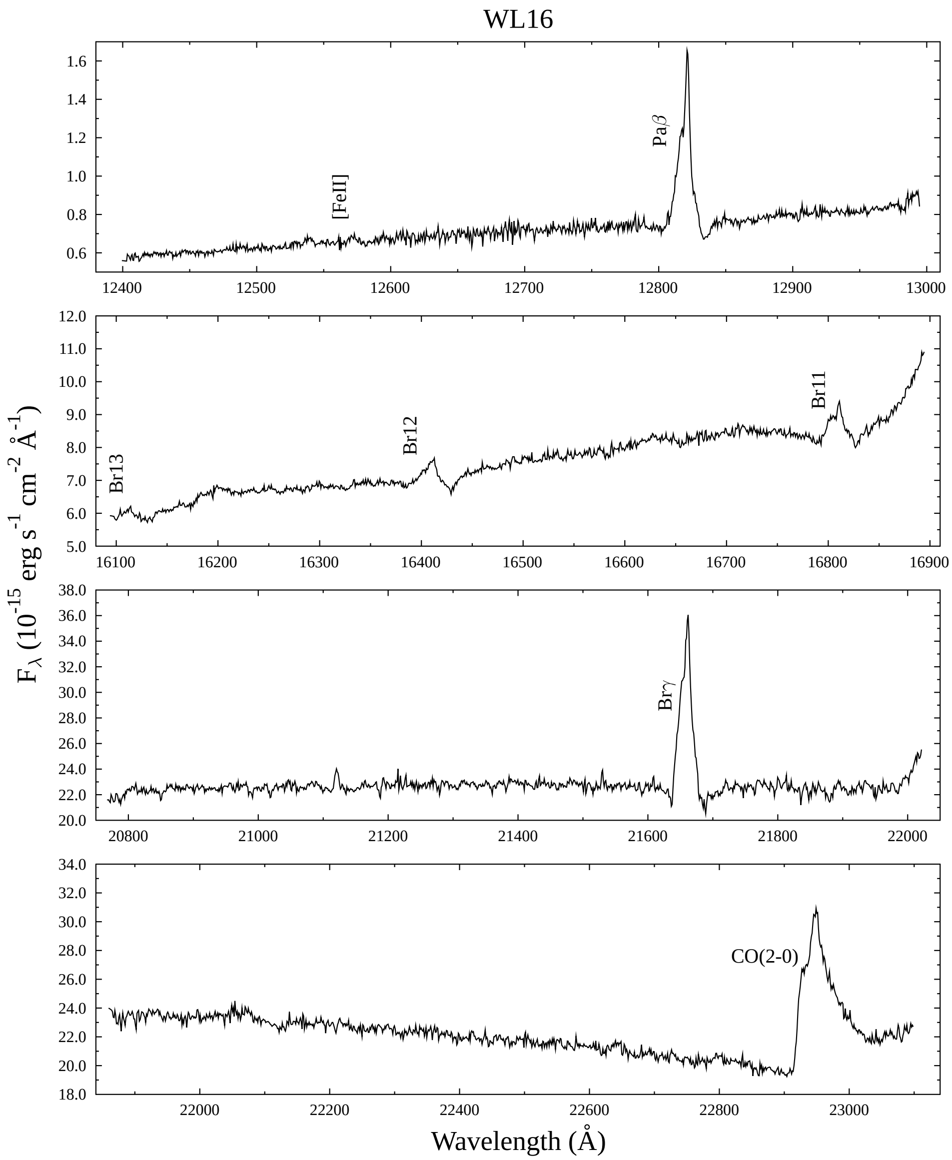

Figure 6.2: J-, H- and K-band spectra of WL16. Both Brγ and Paβ lines show inverse P-Cygni profiles.

6.1.1 Discussion on the observed spectral features

The ISAAC spectra of the set of Class I sources show different spectral features that vary from one object to another. The HI emission is the only feature in common in all the objects of the sample, while H_2 and [Fe II] emission is detected in the ~60% and 50% of the sources, with a ~37% of them showing both [Fe II] and H_2 emission. Only one of the sources, WL16, presents CO emission.

These features are commonly observed in embedded sources. Doppmann et al. (2005), who obtained K-band spectra of ~50 Class I sources, detected HI, H_2 and CO emission

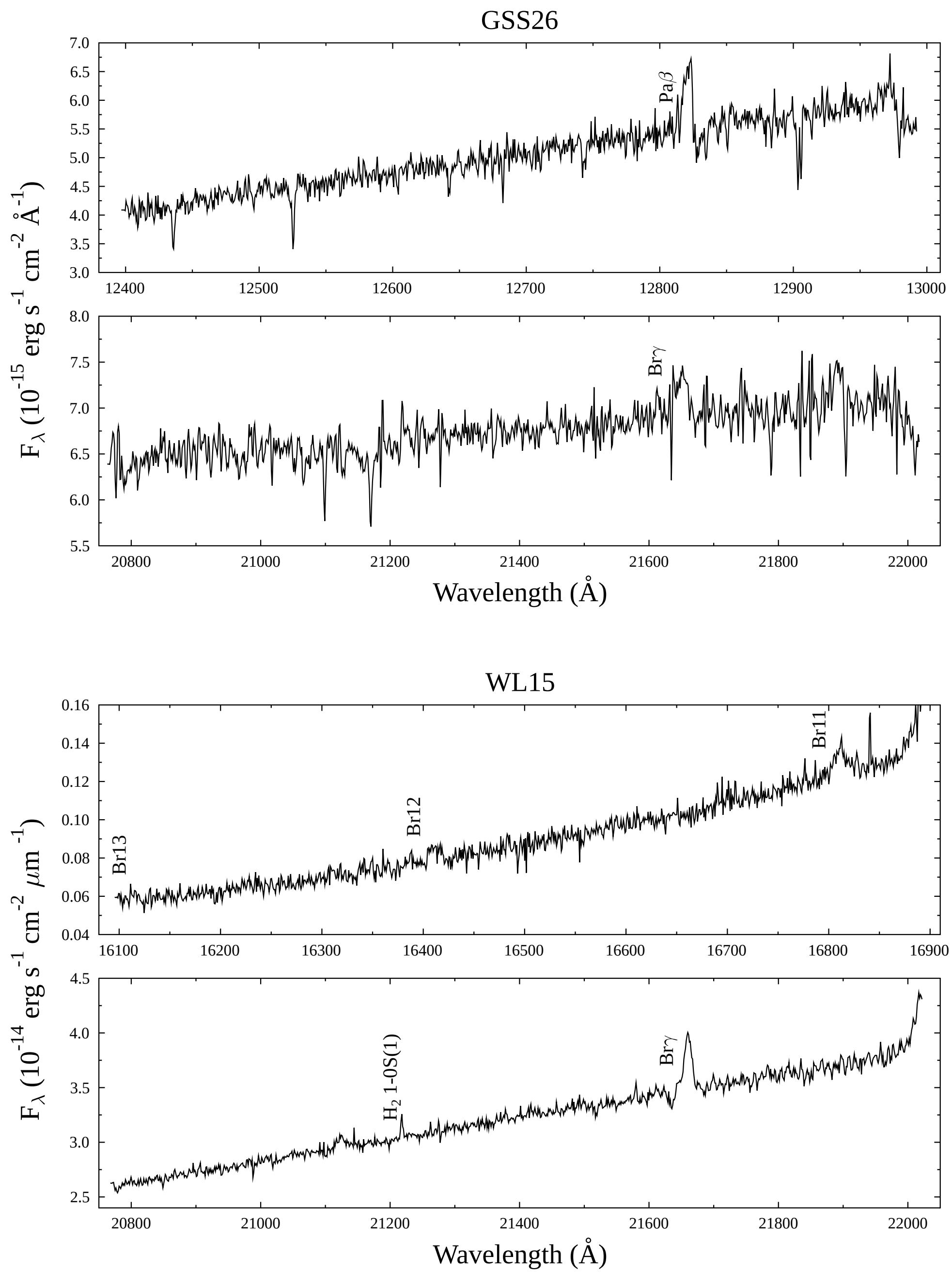

Figure 6.3: (Top) J- and K-band spectra of GSS26. (Bottom) H- and K-band spectra of WL15.

in a total of 65%, 44% and 15% of the objects of their sample. In addition they found that CO emission is always related with HI transitions. In the sample studied here there is no correlation between emission of permitted lines and [Fe II] and H_2 emission. That is, accretion features seems not to be directly related with the presence of jet lines from the

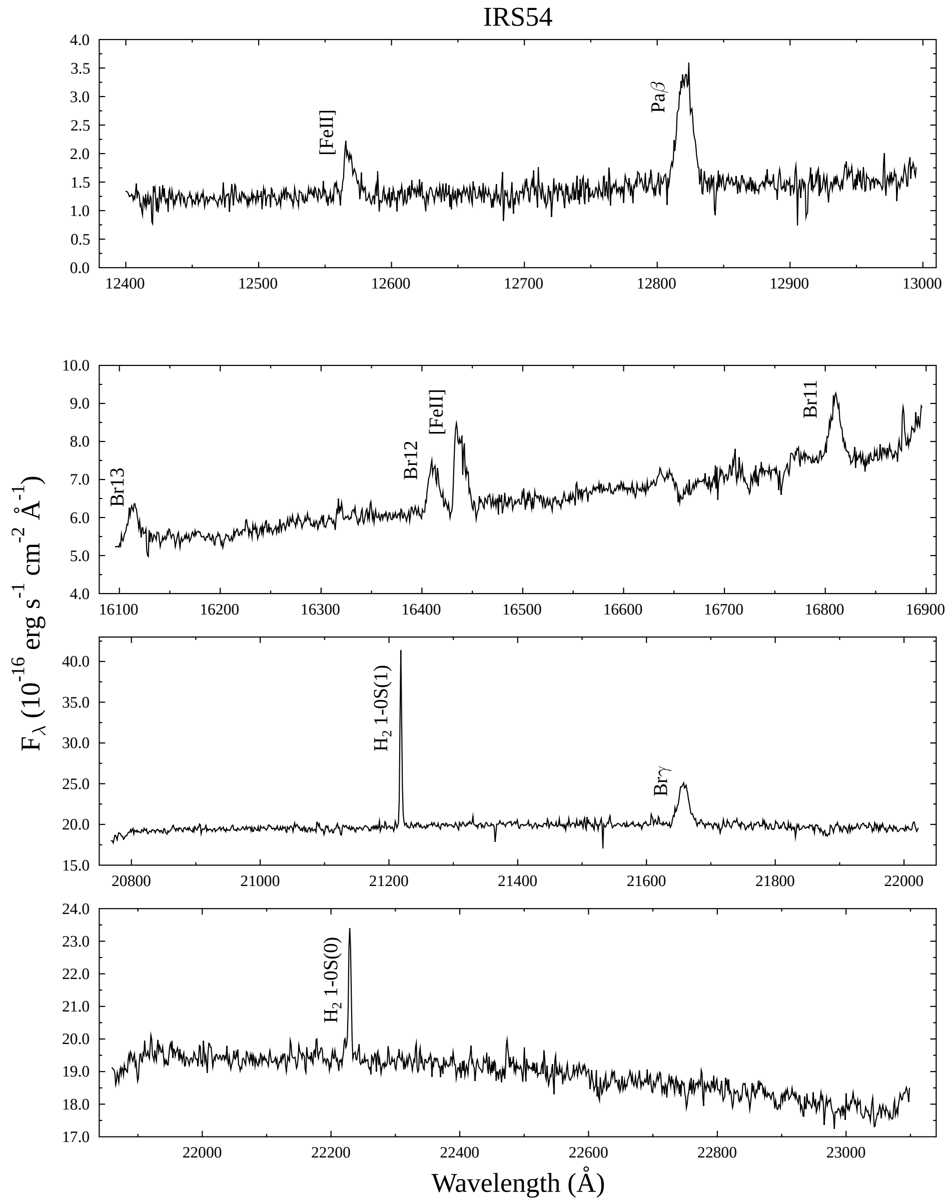

Figure 6.4: J-, H- and K-band spectra of IRS54.

region close to the driving source.

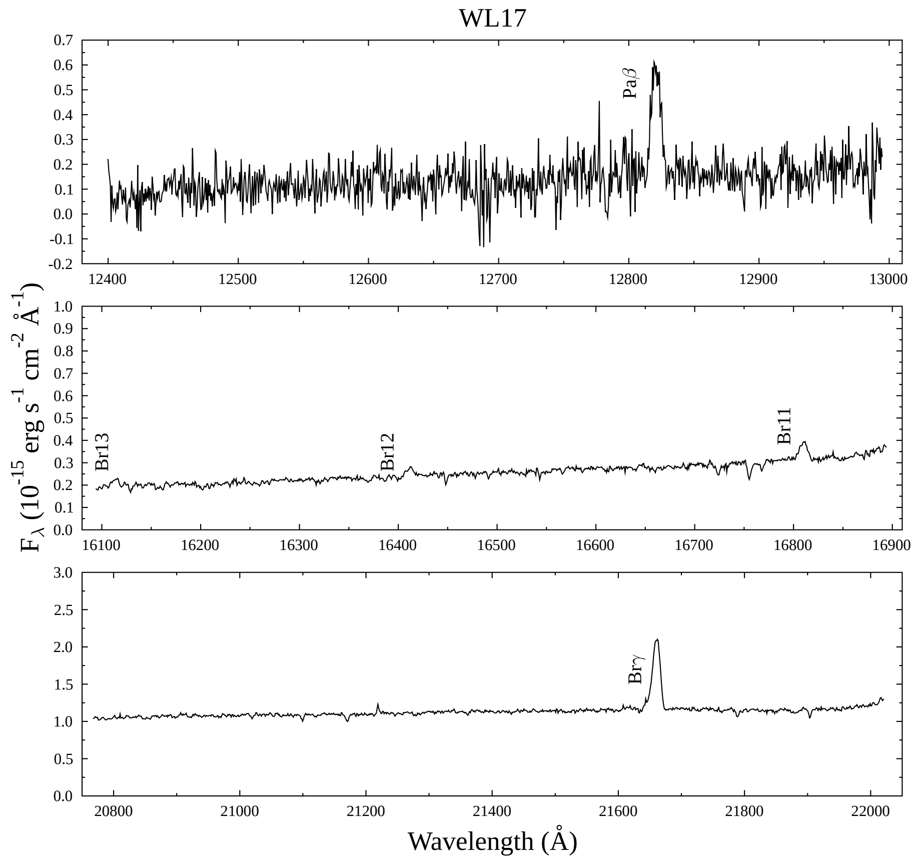

Figure 6.5: J-, H- and K-band spectra of WL17.

6.2 Accretion properties

The accretion luminosity (L_{acc}) for the set of Class I sources has been derived from Brγ luminosity applying the relationship found by Muzerolle et al. (1998) in a sample CTTS:

$$Log\frac{L_{acc}}{L_{\odot}} = (1.26)Log\frac{L_{Br\gamma}}{L_{\odot}} + 4.43 \tag{6.1}$$

We therefore assume that this relation is still valid for the more embedded sources studied here. Such an assumption has been validated by Nisini et al. (2005a) in a small sample of Class I sources of the RCra star forming region.

In order to derive the Brγ luminosity, the line flux has to be corrected for the extinction. As already discussed in Chap. 2.2.2, the extinction toward the source is a critical parameter that represents one of the highest sources of error in the computation of L_{acc}. Extinction values estimates based on NIR colours give usually very uncertain results for very embedded sources, as shown by Antoniucci et al. (2008). Given this problem, the method of computing self-consistent A_K values developed by Antoniucci et al. (2008) have been

Table 6.1: $\dot{M}_{acc}$ for the observed targets.

Source	A_V (mag)	L_{acc} ($L_\odot$)	L_* ($L_\odot$)	M_* ($M_\odot$)	R_* ($R_\odot$)	L_{acc}/L_{bol}	$\dot{M}_{acc}$ (10^{-8} $M_\odot$ yr^{-1})
GSS26	15.4	0.03	0.3	0.1	2.2	0.1	0.03
IRS43	48.9	0.01	1.5	0.4	3.1	<0.1	0.1
IRS54	34.7	0.4	0.3	0.1	2.2	0.7	3.1
WL12	47.8	0.2	0.6	0.2	2.5	0.2	1.3
WL15	27.1	1.9	4.1	0.6	4.2	0.3	20.8
WL16	16.6	3.0	0.7	0.2	2.4	0.8	14.3
WL17	30.1	0.3	0.3	0.1	2.2	0.8	2.6
WL18	8.0	0.1	0.3	0.1	2.2	0.8	0.6
YLW16A	36.1	0.3	1.5	0.4	3.1	0.2	1.7
YLW16B	18.6	0.1	0.3	0.1	2.2	0.3	0.5

employed instead of the available extinction values from literature. This method is based on the observed magnitude of the objects. Indeed, the intrinsic stellar luminosity is given by:

$$Log(L_*/L_\odot) = -0.4(M_{bol} - M_{bol,\odot}) \tag{6.2}$$

where m_K is the observed magnitude, $M_{bol,\odot}$=0.45 is the bolometric magnitude of the Sun and M_{bol} is:

$$M_{bol} = BC + M_K + (V - K)_* \tag{6.3}$$

The absolute magnitude M_K in eq. 6.3 depends on the observed magnitude m_K, the extinction A_K, the veiling r_K, and the distance modulus DM,

$$M_K = m_K + 2.5\,Log(1 + r_K - A_K - DM) \tag{6.4}$$

while the values of the bolometric correction BC and the intrinsic stellar colour $(V - K)_*$ depend on the spectra type and age of the objects. Thus, if we assume that our sources are late-type stars located on the birthline and use the parameters provided by a set of evolutionary models, we can obtain an estimate of A_K from the observed K-band magnitude and veiling of the objects.

On this basis, we adopted a procedure that allowed us to derive the different physical quantities in a self-consistent way. Namely, we varied A_K until we have found a value able to reconcile the stellar luminosity from Eq. 6.2 with the value given by $L_{bol} - L_{acc}$, where L_{acc} is derived from the extinction-corrected (by the considered A_K) Brγ line emission using Eq. 6.1.

The described procedure has been carried out assuming the birthline location of Palla & Stahler (1993) and considering the colours and bolometric correction given by Siess et al. (2000) to convert L_* into M_K (Eqs. 6.2 and 6.3). The inferred values of A_V, L_{acc} and the stellar luminosity, mass and radii are reported in Table 6.1.

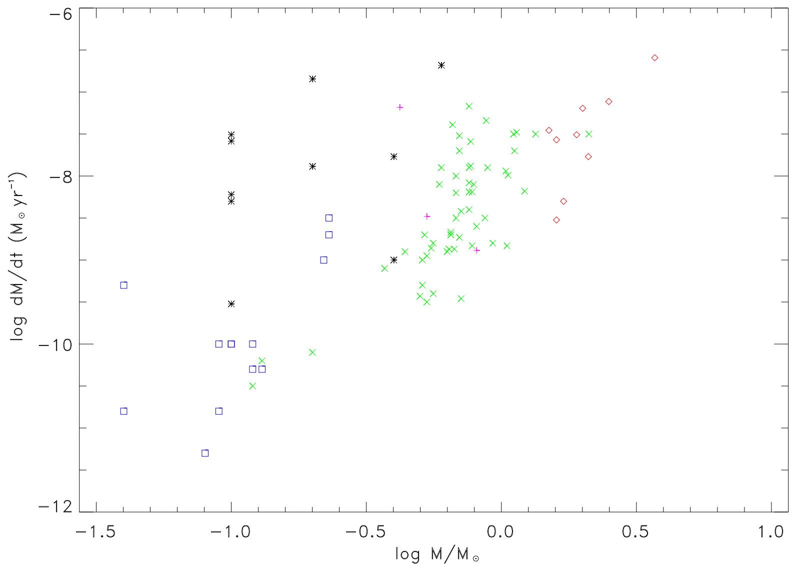

Figure 6.6: Mass accretion rate as a function of the stellar mass for the studied Class I sample (asterisks) and a set of CTTS and brown dwarfs (squares, crosses, plus and rhombi; Muzerolle et al. 2003; White & Ghez 2001; Gullbring et al. 1998; Calvet et al. 2004).

All but two of the sources (GSS26 and IRS43) are actively accreting with $L_{acc} \geq 0.1\,L_\odot$. In particular, WL15 and WL16 show the largest values of L_{acc} (1.9 and $3.0\,L_\odot$, respectively). Despite this fact, the accretion luminosity is a dominant fraction of the total L_{bol} in only four of the ten sources. This is the case of IRS54, WL16, WL17 and WL18 which have $L_{acc}/L_{bol} \geq 0.7$. For the rest of the sources the ratio L_{acc}/L_{bol} is in the 0.1-0.3 range. This work shows therefore that not all the Class I that are assumed to be in an active accretion phase, have their luminosity dominated by the accretion luminosity. This implies that most of the sources of the sample have already accumulated their final mass. This may indicate that an important percentage of objects already classified as Class I sources are not in a high accretion phase. In this case, a large amount of Class I sources would be misclassified Class II stars. This could be principally due to geometrical effects (as e.g., edge-on orientation of the systems) that can significantly affect the colours of the objects, on which the classification of YSOs is mainly based.

It can be also noted that there is no apparent correlation between the value of L_{acc} and the presence of [Fe II] or H_2 emission (associated with jet emission). For example, WL18, where no [Fe II] or H_2 emission has been detected, has $L_{acc}\sim0.8$, roughly the same value found in WL17 that shows bright emission in the H_2 2.122 μm line. Hence, active accretion and ejection do not seem to occur simultaneously.

From the accretion luminosity, it is also possible to derive the mass accretion rate ($\dot{M}_{acc}$) using the expression for disc accretion (Gullbring et al. 1998):

$$\dot{M}_{acc} = \frac{L_{acc} R_*}{G M_*}\left(1 - \frac{R_*}{R_i}\right) \tag{6.5}$$

where R_* and M_* are the stellar radius and mass and R_i is the inner radius of the accretion disc. R_* and M_* are derived from the above analysis and are reported in Table 6.1. For R_i a value of $5\,R_*$ has been assumed following Gullbring et al. (1998).

The inferred $\dot{M}_{acc}$ are reported on Table 6.1. On average, a value of $\dot{M}_{acc}$~$4.5\,10^{-8}\,M_\odot\,yr^{-1}$ have been found among the objects of the sample, with the exception of WL15 and WL16 that show the largest $\dot{M}_{acc}$ with values of $2.1{\times}10^{-7}$ and $1.4{\times}10^{-7}\,M_\odot\,yr^{-1}$, respectively. The same order of magnitude for $\dot{M}_{acc}$ is also found in CTTS (see, Chap 2). It should be noticed, however, that our set of Class I sources are very low-mass stars with $M_* \leq 0.6\,M_\odot$. If we compare the computed $\dot{M}_{acc}$ values with those of CTTS with roughly the same mass then $\dot{M}_{acc}$ is in average larger than the values found for CTTS as shown in Fig. 6.6. Only GSS26 and IRS43, which L_{acc}/L_{bol} ratio is very low, present a $\dot{M}_{acc}$ value similar to the one found in CTTS with the same mass.

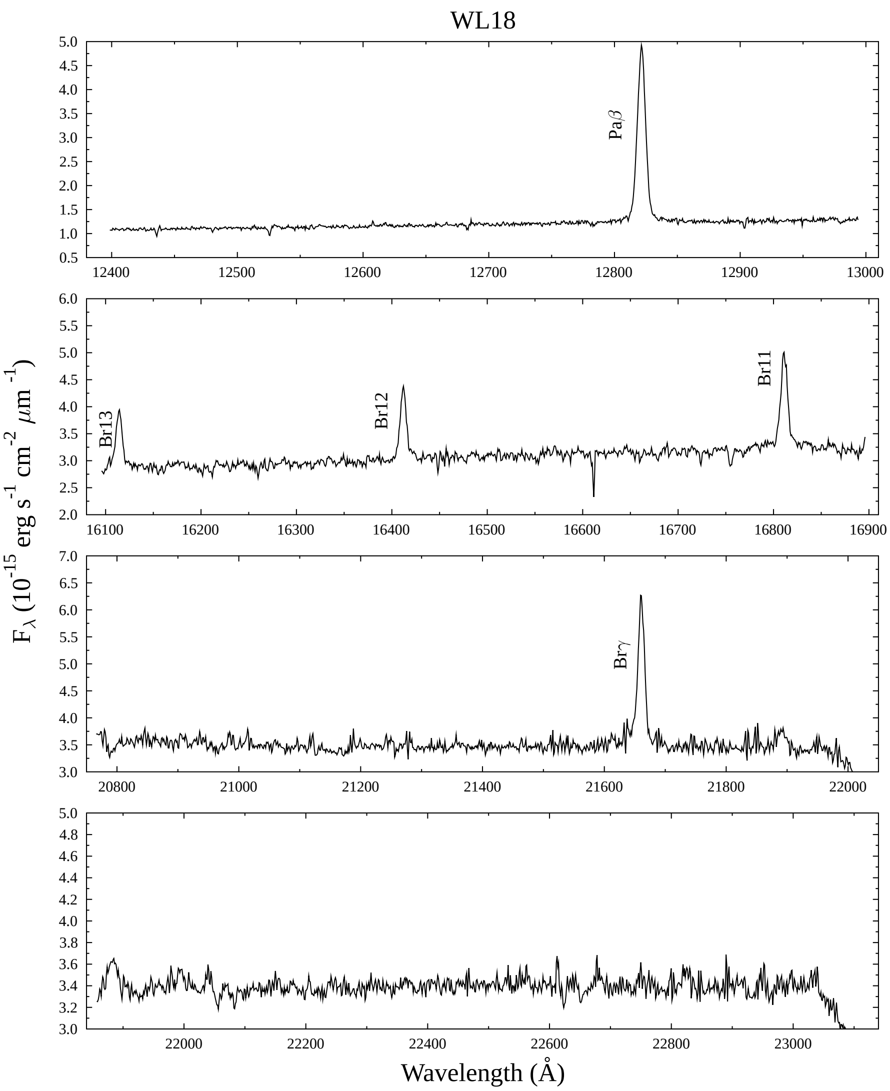

Figure 6.7: J-, H- and K-band spectra of WL18.

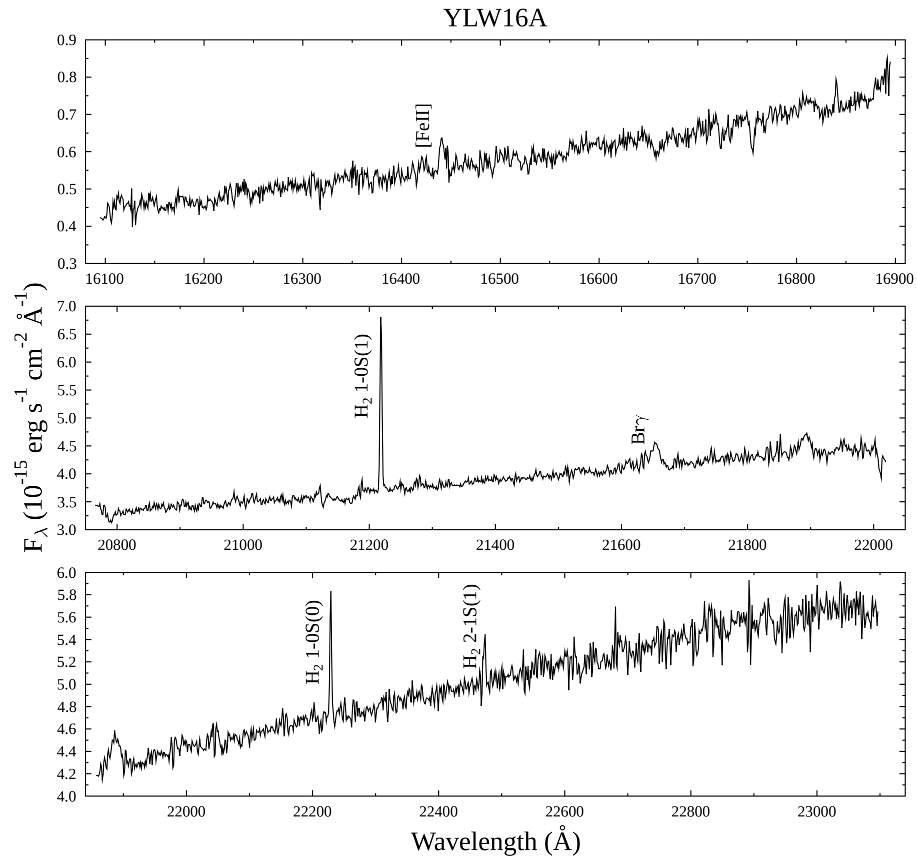

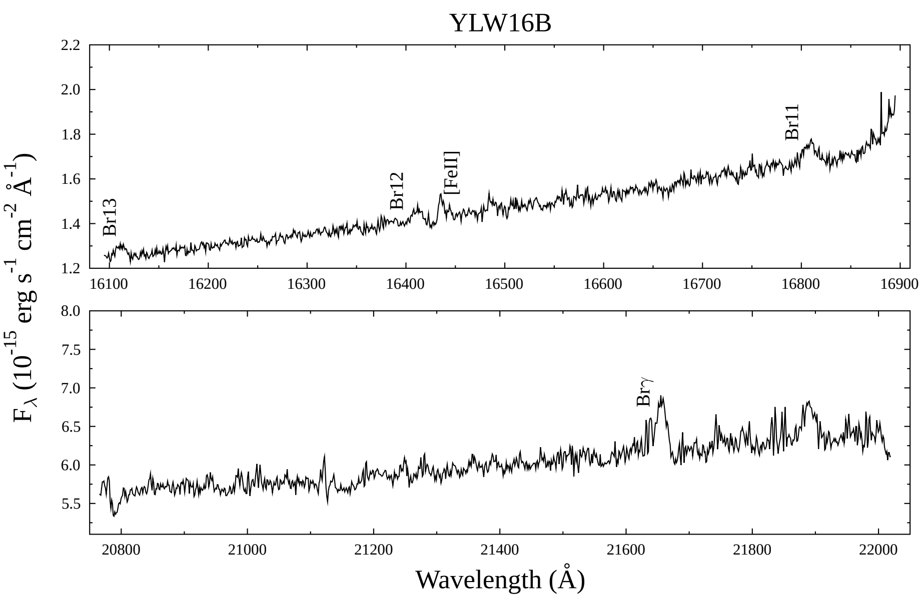

Figure 6.8: (Top)J-, H- and K-band spectra of YLW16A. (Bottom) H- and K-band spectra of YLW16B

Table 6.2: Emission features in the observed Class I sources.

Line id.	λ	WL16	WL12	WL17	YLW16A	YLW16B	IRS54	WL15	WL18	GSS26	IRS43
	μm	10^{-14}	10^{-17}	10^{-16}	10^{-15}	10^{-15}	10^{-15}	10^{-15}	10^{-14}	10^{-15}	10^{-15}
[Fe II] $a^4D_{7/2}$-$a^6D_{9/2}$	1.257	0.03±0.01					0.9±0.1				
Paβ	1.282	0.9±0.1		39.7±0.1			2.8±0.1		2.9±0.1	0.8±0.1	
Br 13	1.611	0.5±0.1		3.2±0.8		1.0±0.3	1.4±0.1	0.5±0.2	0.9±0.1		
Br 12	1.641	1.6±0.2		4.4±0.9		1.0±0.3	1.7±0.1	1.2±0.5	1.1±0.1		
[Fe II] $a^4D_{7/2}$-$a^4F_{9/2}$	1.644		3.5±0.1		0.6±0.1	0.7±0.1	2.5±0.2				
[Fe II] $a^4D_{1/2}$-$a^4F_{5/2}$	1.664		0.6±0.2								
[Fe II] $a^4D_{5/2}$-$a^4F_{7/2}$	1.677		1.3±0.2				0.5±0.3				
Br 11	1.681	2.2±0.2		7.3±0.5	0.8±0.2	1.6±0.3	2.1±0.2	1.8±0.6	1.6±0.1		
H_2 1-0 S(9)	1.687		0.5±0.1								
H_2 1-0 S(1)	2.122		20.6±0.1	5.0±0.7	12.1±0.1		7.2±0.1	8.3±1.3			
Brγ	2.166	310.0±0.1	2.51±0.5	144.0±20.2	7.3±1.1	124.0±1.6	100.6±0.6	758.0±6.9	3.9±0.1	9.6±2.6	2.1±0.5
	2.223		13.2±0.3		3.8±0.2		2.0±0.1				
H_2 2-1 S(1)	2.247		4.9±0.3		1.9±0.2		0.4±0.7				
CO (2-0)	2.294	520.0±0.1									

Fluxes not corrected for extinction in units of 10^x erg s^{-1} cm^{-2}.

Conclusions

The general aim of this thesis is to perform an investigation of the accretion and ejection properties of young embedded protostars (the so-called Class 0/I sources).

One of the main objectives is to probe through IR spectroscopic techniques the physics, kinematics and dynamics of the collimated jet driven by a sample of Class 0/I sources: the set of observationally derived physical parameters has been compared with those of optically visible jets from TTauri stars in order to evidence any evolutionary effect. They have been, in addition, used to constrain the current theoretical models for the jet launching and acceleration. Such a study has been performed using ISAAC instrument mounted at the VLT, that provided the spectral and angular resolution needed to resolve the different kinematical components of the jet at the relevant spatial scales.

In addition to this study, part of the thesis work has been also devoted to the determination of the accretion properties of embedded sources. With this aim, the accretion luminosity and mass accretion rates of a sample of ten Class I sources located in the ρ Oph molecular cloud have been measured through the analysis of their IR permitted line emission in order to revise their evolutionary status.

The main results obtained in this work are summarised below:

Large scale jet properties:

- Deep ISAAC VLT observations have been obtained of two Class I (HH34 and HH46-47) and three Class 0 (HH1, HH111, HH212) objects. The jets from the Class I sources have been detected down to the central object, while the Class 0 jets have been observed when they emerge from the dense envelope of their driving source, at about 1-5$''$ of distance. All the jets show an atomic and molecular component, traced by [Fe II] and H_2 lines, respectively. The two components trace different sections of the same jet: while the atomic gas is located in the inner ionised region, the molecular gas traces the outer and less excited sections.

- The kinematical properties of the jets as a function of the distance have been studied in detail through Position-Velocity Diagrams (PVDs) of the [Fe II] and H_2 line emission. The radial velocities of these two jet components range between ~20-250 km s^{-1} and decrease with the distance from the source. On small scale, radial velocities show, however, cyclic variations along the jets. This modulation in velocity can be due, e.g., to variations of the ejection velocities at different epochs or to jet precession induced by the presence of a companion close to the driving source.

- Individual emission knots often present a double velocity component, probably due to the presence of mini bow shocks, where the velocity decreases going from the bow apex to the bow flanks, intercepted by the instrument slit.

- The FWHM of the detected lines would imply shock velocities between 50 and 80 km s^{-1}. Such high velocity shocks produce ionisation fractions of the order of 0.3-0.4, i.e., higher than the values of x_e measured in these jets, which are lower than 0.2. This indicates that the line widening is determined not only by shock dispersion but also by, e.g., a lateral expansion of the jet.

- The electron density (n_e) in the jet atomic component has been measured in different velocity components from the ratio of density sensitive [Fe II] lines (1.600/1.644 μm). The electron density along the jets decreases from the inner to the outer knots, with values averaged over the brightest knots ranging between 2600 cm^{-3} and 6200 cm^{-3}. Class 0 jets present on average larger electron densities with respect to Class I jets. This fact probably reflects the higher total densities in the environments of the still deeply embedded Class 0 sources. In the knots that can be well represented by non-resolved bow shocks, the electron density increases with velocity, as expected by bow-shock models.

- The observations of additional lines of less abundant species, such as [P II] and [Ti II] have allowed to measure the gas phase abundance of Iron and to study the dust reprocessing of refractory elements. The observed ratio of [Fe II]/[P II] in HH46-47 implies that only about 12% of iron is in gaseous form near the source, increasing to a value of 42% in the external knots. This indicates that a significant fraction of dust is present in the inner jet region. Finally, comparing the observed [Ti II]/[Fe II] ratio in the HH1 jet with the theoretical expected value, a gas-phase Fe/Ti abundance ratio 2-3 times less than solar have been found. This seems to indicate that the release of gas-phase elements from dust grains likely follows a selective pattern in which Ti-bearing condensates are more easily destroyed than the Fe ones.

- The jet mass flux transported by the atomic component have been measured from the [Fe II] 1.644 μm line luminosity. In all the jets, but HH212, most of the mass flux is carried out by the atomic gas that thus represents the dynamically more important component in the jet. The derived values are in the range 2×10^{-8}-2×10^{-7} $M_\odot$ yr^{-1} and remain roughly constant with the distance from the driving source, as expected in steady jet flows. These values of $\dot{M}_{jet}$ are higher by about an order of magnitude with respect to the values inferred in most of the Classical T Tauri stars (CTTSs), as expected for younger actively accreting sources.

The base of Class I jets:

- The kinematics and physical properties of the HH34 and HH46-47 jets within 1 000 AU from the central source have been studied in detail in order to give constrains to the current jet formation theoretical models. The HH34 and HH46-47 [Fe II] PVDs present near the source two components at high ($\sim$100-200 km s^{-1}) and low ($\sim$50 km s^{-1}) velocity (the high velocity component, HVC, and low velocity component, LVC). A fainter red-shifted counterflow has been detected for the first time in HH34 down to the central source and up to a distance of $\sim$25″ (11 500 AU) from the star. At variance with [Fe II] the H_2 PVDs are different in the two objects. The HH34 H_2 PVD shows spatially- and kinematically-separated LVC and HVC, and only the LVC is visible down to the central source. This component is close to 0 km s^{-1} LSR velocity and the blue-shifted and red-shifted jet differs by less than 10 km s^{-1} . At intermediate velocities between these two components, no emission is detected in the H_2 PVD. The H_2 PVD of the HH46-47 jet shows, however, a single velocity component at $\sim$20 km s^{-1}.

- The electron density and mass loss rate has been derived as a function of the velocity component. At variance with found at large distances from the source, both jets show increasing electron densities with decreasing velocities in the innermost regions, with average values ranging from 10.8×10^3 cm^{-3} to 4.7×10^3 cm^{-3} for the LVC and HVC of the HH34 jet and from 7650 cm^{-3} to 5400 cm^{-3} for the LVC and HVC of the HH46-47 jet. The bulk of the mass along the jets is, however, carried out by the HVC.

- The PVDs of the inner region of HH34 and HH46-47 are similar to the ones observed in the forbidden emission line (FEL) regions of CTTS. The LVC in CTTS is, however, confined within a distance of d$\leqslant$200 AU from the source, while in HH34 and HH46-47 it reaches distances up to $\sim$1000 AU.

  In CTTS the electron density near the source has been found to increase with velocity at variance with what is found in HH34 and HH46-47. On the other hand, it seems that in CTTS the total density in the LVC is higher than in the HVC because of the much lower ionisation fraction. Therefore, the density structure in Class I jets and in T Tauri stars might be similar, but they differ in the excitation conditions. The different excitation structure could represent also the cause of the different extent of the LVC in Class I and TTaturi stars.

- The comparison of the PVDs of the HH34 and HH46-47 jets and the electron densities with the predictions provided by MHD launching models suggests that the kinematical features observed close to the source in the analysed spectra can be, qualitatively, reproduced by both disc-wind and X-wind models. Neither of them is able, however, to explain the persistence of the LVC at large distances (up to 1000 AU) from the launching region. Moreover, none of the excitation mechanisms proposed in these models can explain the velocity dependence on electron density that is measured in HH34 and HH46-47. The analysis presented here clearly shows the need for a refinement of the existing models in order to take into account the observed discrepancies.

Accretion properties of Class I sources:

- The near IR spectra of a sample of ten Class I objects in the ρ Oph molecular cloud show different characteristic, with emission lines that varies among the different objects of the sample. In particular, in all the objects permitted HI emission lines have been detected in form of transitions from the Brackett and Paschen series. while transitions typical of jets, such as the [Fe II] and H_2 lines, have been detected in only the 60% and 50% of the sources, respectively.

- The profiles of the Brackett series lines are all symmetric with widths that indicate velocity dispersions of the order of 100-300 km s^{-1}. The only exception is WL16, where the HI transitions clearly show and inverse P-Cygni profile, indicating matter in infall motion toward the source. This source presents also emission from the CO 2.3 μm band, that is a further evidence for the presence of a warm gas probably heated in an accretion disc.

- From the Brγ emission flux, the K-band magnitude of the sources and their bolometric luminosity, important source parameters have been possible to derive such as mass, accretion luminosity and mass accretion rate. These parameters have been used to determine which fraction of the Class I sources are actively accreting and if there is any correlation between the mass accretion rate and the mass of the source.

  Only four of the ten sources (IRS54, WL16, WL17 and WL18) have accretion dominated luminosities (L_{bol}/L_{acc}~0.7-0.8) with $\dot{M}_{acc}$ ranging from 3×10^{-8} $M_\odot$ yr^{-1} to 1×10^{-7} $M_\odot$ yr^{-1}. The derived $\dot{M}_{acc}$ within the sample are in average higher that the values found for CTTS of the same mass, with the exception of GSS26 and IRS43 that show the lowest bolometric to accretion luminosity ratio ($L_{bol}/L_{acc}\leq0.1$). It seems, therefore, that only a few percentage of the sources classified as Class I have accretion dominated luminosities: these sources are probably already in a TTauri phase, but still embedded in their residual envelopes.

The analysis presented here shows the potential of NIR spectroscopy to the study of the accretion and ejection properties of Class I objects. Although this work has lead to important results, these need to be confirmed on a larger number of sources. In particular, observations on larger samples of Class I sources from different molecular clouds and with different masses are needed in order to better understand the accretion properties of these objects and their connection with the TTauri stars. This statistical work together with accurate measurements of the mass loss to accretion rate will help us to understand the connection between accretion and ejection and the jet launching mechanism.

In addition, more stringent constraints to the proposed MHD launching models are needed. These can be obtained only probing the innermost regions, i.e., inside ~100 AU from the driving source. It is therefore fundamental to use the largest spatial resolution available with the present instrumentation. The use of adaptive optics (AO) with laser guide stars (LGS) open the possibility to investigate the inner jet region with diffraction limited performances also in embedded Class I sources. In addition, it will be very important to use integral field unit facilities available with instruments like SINFONI at VLT, to have a 3-D structure of the jets, that will make it possible to study the excitations and kinematics also in the transverse section of the jet. These kind of analysis will make possible to bring the study of jets from young embedded sources at the same level of development as that now reached in CTTSs.

Appendix A

Appendix - Rovibrational diagrams and line fluxes along the HH46-47 jet.

In this Appendix I report the low-resolution spectroscopic line fluxes (not de-reddened) observed on each of the analysed knots along HH46-47 together with the inferred rovibrational diagrams, with the exception of knot Z2 which line fluxes and rovibrational diagram are reported on Chap. 5.

Line Fluxes

Table 6.3: Observed unreddened lines along HH46-47: H_2 lines.

Line id.	$\lambda(\mu$m)	F (Δ F)(10^{-16}erg s^{-1}cm^{-2})					
		S	Z2	X	Y3	Y2	Y1
H_2 2-1 S(5)	1.945	...	...	...	...	...	2.7(0.7)
H_2 1-0 S(2)	2.034	...	2.1(0.6)	26.6(0.6)	10.0(0.6)	13.2(0.4)	8.7(0.4)
H_2 2-1 S(3)	2.074	...	...	3.7(0.5)	2.3(0.2)	3.9(0.4)	...
H_2 1-0 S(1)	2.122	12.0(0.5)	5.6(0.3)	36.3(0.3)	27.0(0.3)	3.3(0.2)	22.7(0.2)
H_2 2-1 S(2)	2.154	...	...	1.1(0.2)	...	1.6(0.2)	...
H_2 1-0 S(0)[1]	2.224	12.7(0.6)	3.1(0.6)	7.7(0.4)	5.4(0.5)	6.9(0.3)	5.2(0.2)
H_2 2-1 S(1)	2.248	...	1.4(0.4)	3.4(0.3)	3.0(0.5)	4.6(0.2)	3.5(0.3)
H_2 1-0 Q(1)	2.407	16.6(1.3)	4.8(0.6)	28.9(0.6)	20.8(0.8)	24.3(0.7)	17.8(0.5)
H_2 1-0 Q(2)	2.413	13.8(1.5)	2.3(0.3)	...	...	...	...
H_2 1-0 Q(3)	2.424	16.2(1.3)	5.8(0.5)	30.7(0.6)	23.3(1.5)	26.5(0.7)	17.8(0.5)
H_2 1-0 Q(4)	2.437	9.3(1.1)	...	8.4(0.7)	6.1(1.2)	8.0(0.6)	5.2(0.6)
H_2 1-0 Q(5)	2.455	...	...	23.4(0.9)	15.7(1.6)	21.6(0.8)	14.9(0.7)
H_2 1-0 Q(6)	2.476	...	...		...	6.6(0.6)	...

Table 6.4: Observed unreddened lines along HH46-47: atomic lines.

Line id.	$\lambda(\mu m)$	F (Δ F)(10^{-16}erg s^{-1}cm^{-2})				
		S	HH46-1	B8	Z2	X
[P II] $^3P_2$-$^1D_2$	1.188	6.2(1.2)	...	...	...	...
[Fe II] $a^4D_{5/2}$-$a^6D_{7/2}$	1.249	1.9(0.6)	...	...	...	...
[Fe II] $a^4D_{7/2}$-$a^6D_{9/2}$	1.257	54.2(0.8)	15.8(0.9)	11.9(0.7)	7.1(0.9)	6.4(1.0)
[Fe II] $a^2G_{9/2}$-$a^4D_{7/2}$	1.267	3.2(0.8)	...	...	...	...
[Fe II] $a^4D_{1/2}$-$a^6D_{1/2}$	1.271	2.0(0.3)	...	...	...	...
[Fe II] $a^4D_{3/2}$-$a^6D_{3/2}$	1.279	2.4(0.6)	...	...	...	...
[Fe II] $a^4D_{5/2}$-$a^6D_{5/2}$	1.295	8.9(1.1)	...	...	...	...
[Fe II] $a^4D_{3/2}$-$a^6D_{1/2}$	1.298	3.4(0.9)	...	...	...	...
[Fe II] $a^2G_{7/2}$-$a^4D_{3/2}$	1.300	1.7(0.6)	...	...	...	...
[Fe II] $a^4D_{7/2}$-$a^6D_{7/2}$	1.321	13.1(0.4)	4.5(1.4)	3.5(0.5)	3.0(1.2)	2.4(1.2)
[Fe II] $a^4D_{5/2}$-$a^6D_{3/2}$	1.328	4.3(0.6)	...	...	...	...
[Fe II] $a^4D_{5/2}$-$a^4F_{9/2}$	1.534	9.9(1.0)	...	...	0.7(0.4)	...
[Fe II] $a^4D_{3/2}$-$a^4F_{7/2}$	1.600	11.2(1.0)	...	...	0.9(0.4)	...
[Fe II] $a^4D_{7/2}$-$a^4F_{9/2}$	1.644	85.8(0.7)	8.9(0.5)	8.7(0.8)	20.1(0.5)	4.4(0.5)
[Fe II] $a^4D_{1/2}$-$a^4F_{5/2}$	1.664	5.7(0.8)	...	...	1.1(0.7)	...
[Fe II] $a^4D_{5/2}$-$a^4F_{7/2}$	1.677	13.3(0.9)	...	...	1.8(0.4)	...
[Fe II] $a^4D_{3/2}$-$a^4F_{3/2}$	1.797	5.2(0.9)	...	...	...	...
[Fe II] $a^4D_{5/2}$-$a^4F_{5/2}$	1.800	14.3(0.7)	...	...	...	...
[Fe II] $a^4D_{7/2}$-$a^4F_{7/2}$	1.810	52.6(1.1)	...	...	...	...
[Fe II] $a^2P_{3/2}$-$a^4P_{3/2}$	2.133	3.2(0.5)	...	...	...	...

Table 6.5: Observed unreddened lines along HH46-47: other lines.

Line id.	$\lambda(\mu m)$	F (Δ F)(10^{-16}erg s^{-1}cm^{-2})	
		S	HH46-1
Paβ	1.282	19.8(1.2)	2.7(0.7)
Brγ	2.166	9.4(0.8)	1.1(0.5)
CO (2-0)	2.294		...
CO (3-1)	2.323	4.7(1.4)	...

Rovibrational diagrams

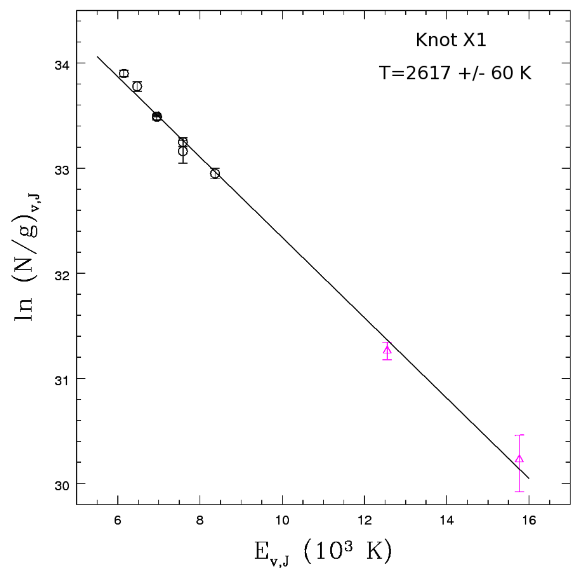

Figure 1: H_2 rotational diagram for the different lines in the knot X1. Different symbols indicate lines coming from different vibrational levels. The straight line represents the best fit through the data. The corresponding temperature is indicated. An extinction of A_V=5.5 mag was adopted.

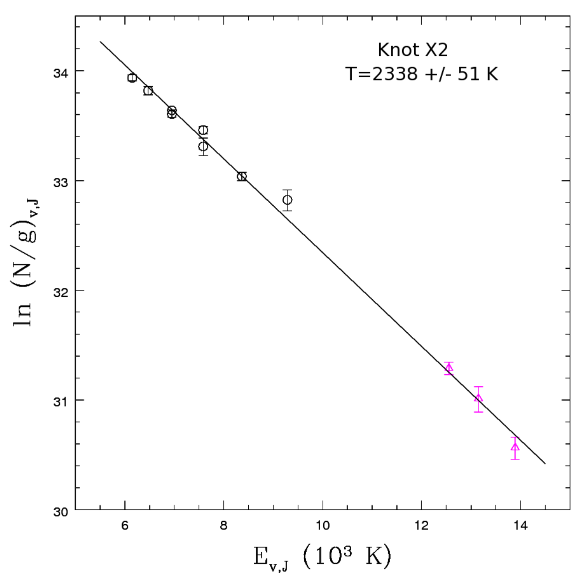

Figure 2: H_2 rotational diagram for the different lines in the knot X2. Different symbols indicate lines coming from different vibrational levels. The straight line represents the best fit through the data. The corresponding temperature is indicated. An extinction of A_V=7 mag was adopted.

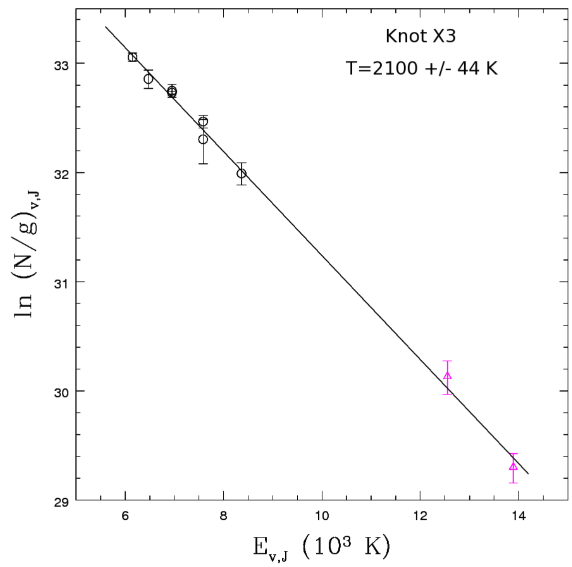

Figure 3: H_2 rotational diagram for the different lines in the knot X3. Different symbols indicate lines coming from different vibrational levels. The straight line represents the best fit through the data. The corresponding temperature is indicated. An extinction of A_V=8.5 mag was adopted.

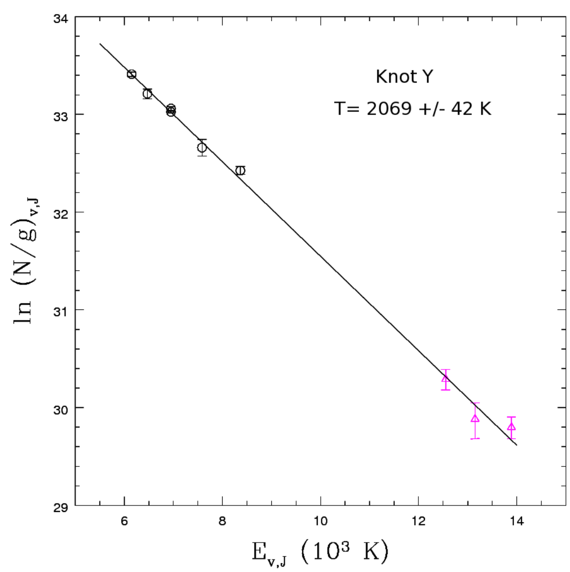

Figure 4: H_2 rotational diagram for the different lines in the knot Y. Different symbols indicate lines coming from different vibrational levels. The straight line represents the best fit through the data. The corresponding temperature is indicated. An extinction of A_V=8 mag was adopted.

Bibliography

2009, in Lecture Notes in Physics, Berlin Springer Verlag, Lecture Notes in Physics, Berlin Springer Verlag

Adams, F. C., Lada, C. J., & Shu, F. H. 1987, ApJ, 312, 788

Andre, P., Ward-Thompson, D., & Barsony, M. 1993, ApJ, 406, 122

Andre, P., Ward-Thompson, D., & Barsony, M. 2000, Protostars and Planets IV, 59

Anglada, G., Estalella, R., Mauersberger, R., et al. 1995, ApJ, 443, 682

Antoniucci, S., Nisini, B., Giannini, T., & Lorenzetti, D. 2008, A&A, 479, 503

Asplund, M., Grevesse, N., & Sauval, A. J. 2005, in Astronomical Society of the Pacific Conference Series, Vol. 336, Cosmic Abundances as Records of Stellar Evolution and Nucleosynthesis, ed. T. G. Barnes, III & F. N. Bash, 25–+

Bacciotti, F. & Eislöffel, J. 1999, A&A, 342, 717

Bacciotti, F., Mundt, R., Ray, T. P., et al. 2000, ApJ, 537, L49

Bacciotti, F., Ray, T. P., Mundt, R., Eislöffel, J., & Solf, J. 2002, ApJ, 576, 222

Bally, J., Heathcote, S., Reipurth, B., et al. 2002, AJ, 123, 2627

Bally, J. & Lane, A. P. 1982, ApJ, 257, 612

Bautista, M. A., Hartman, H., Gull, T. R., Smith, N., & Lodders, K. 2006, MNRAS, 370, 1991

Beck, T. L. 2007, AJ, 133, 1673

Beck, T. L., McGregor, P. J., Takami, M., & Pyo, T.-S. 2008, ApJ, 676, 472

Beck, T. L., Riera, A., Raga, A. C., & Reipurth, B. 2007, AJ, 133, 1221

Bonito, R., Orlando, S., Peres, G., Favata, F., & Rosner, R. 2007, A&A, 462, 645

Bouvier, J. 2007, in IAU Symposium, Vol. 243, IAU Symposium, ed. J. Bouvier & I. Appenzeller, 231–240

Bouvier, J., Covino, E., Kovo, O., et al. 1995, A&A, 299, 89

Bragg, S. L., Smith, W. H., & Brault, J. W. 1982, ApJ, 263, 999

Cabrit, S., Codella, C., Gueth, F., et al. 2007, A&A, 468, L29

Cabrit, S., Ferreira, J., & Raga, A. C. 1999, A&A, 343, L61

Calvet, N., Hartmann, L., & Strom, S. E. 2000, Protostars and Planets IV, 377

Calvet, N., Muzerolle, J., Briceño, C., et al. 2004, AJ, 128, 1294

Camenzind, M. 1990, in Reviews in Modern Astronomy, Vol. 3, Reviews in Modern Astronomy, ed. G. Klare, 234–265

Caratti o Garatti, A., Froebrich, D., Eislöffel, J., Giannini, T., & Nisini, B. 2008, A&A, 485, 137

Caratti o Garatti, A., Giannini, T., Nisini, B., & Lorenzetti, D. 2006, A&A, 449, 1077

Chernin, L. M. & Masson, C. R. 1995, ApJ, 443, 181

Chini, R., Reipurth, B., Sievers, A., et al. 1997, A&A, 325, 542

Choi, M. & Zhou, S. 1997, ApJ, 477, 754

Claussen, M. J., Marvel, K. B., Wootten, A., & Wilking, B. A. 1998, ApJ, 507, L79

Codella, C., Cabrit, S., Gueth, F., et al. 2007, A&A, 462, L53

Coffey, D., Bacciotti, F., Woitas, J., Ray, T. P., & Eislöffel, J. 2004, ApJ, 604, 758

Cohen, M. & Schwartz, R. D. 1987, ApJ, 316, 311

Davis, C. J., Berndsen, A., Smith, M. D., Chrysostomou, A., & Hobson, J. 2000a, MNRAS, 314, 241

Davis, C. J., Hodapp, K. W., & Desroches, L. 2001a, A&A, 377, 285

Davis, C. J., Ray, T. P., Desroches, L., & Aspin, C. 2001b, MNRAS, 326, 524

Davis, C. J., Smith, M. D., & Eislöffel, J. 2000b, MNRAS, 318, 747

Davis, C. J., Stern, L., Ray, T. P., & Chrysostomou, A. 2002, A&A, 382, 1021

Davis, C. J., Whelan, E., Ray, T. P., & Chrysostomou, A. 2003, A&A, 397, 693

Doppmann, G. W., Greene, T. P., Covey, K. R., & Lada, C. J. 2005, AJ, 130, 1145

Dougados, C. 2009, in Lecture Notes in Physics, Berlin Springer Verlag, ed. T. Ray & K. Tsinganos, Lecture Notes in Physics, Berlin Springer Verlag

Dougados, C., Cabrit, S., Lavalley, C., & Ménard, F. 2000, A&A, 357, L61

Draine, B. T. 2003, ARA&A, 41, 241

Eislöffel, J. & Mundt, R. 1992, A&A, 263, 292

Eislöffel, J. & Mundt, R. 1994, A&A, 284, 530

Eislöffel, J. & Mundt, R. 1997, AJ, 114, 280

Eislöffel, J., Mundt, R., & Böhm, K.-H. 1994, AJ, 108, 1042

Eislöffel, J., Smith, M. D., & Davis, C. J. 2000, A&A, 359, 1147

Esposito, S. & Pinna, E. 2008, in Lecture Notes in Physics, Berlin Springer Verlag, Vol. 742, Lecture Notes in Physics, Berlin Springer Verlag, ed. F. Bacciotti, L. Testi, & E. Whelan, 45–+

Fernandes, A. J. L. 2000, MNRAS, 315, 657

Ferreira, J. 1997, A&A, 319, 340

Ferreira, J. & Casse, F. 2004, Ap&SS, 292, 479

Ferreira, J., Dougados, C., & Cabrit, S. 2006, A&A, 453, 785

Flower, D. R., Le Bourlot, J., Pineau des Forêts, G., & Cabrit, S. 2003, MNRAS, 341, 70

Garcia, P. J. V., Ferreira, J., Cabrit, S., & Binette, L. 2001a, A&A, 377, 589

Garcia, P. J. V., Ferreira, J., Cabrit, S., & Binette, L. 2001b, A&A, 377, 609

Giannini, T., Calzoletti, L., Nisini, B., et al. 2008, A&A, 481, 123

Giannini, T., McCoey, C., Caratti o Garatti, A., et al. 2004, A&A, 419, 999

Goodman, A. A., Benson, P. J., Fuller, G. A., & Myers, P. C. 1993, ApJ, 406, 528

Greene, T. P. & Lada, C. J. 1996, AJ, 112, 2184

Greene, T. P. & Lada, C. J. 2002, AJ, 124, 2185

Gullbring, E., Hartmann, L., Briceno, C., & Calvet, N. 1998, ApJ, 492, 323

Hamann, F., Simon, M., Carr, J. S., & Prato, L. 1994, ApJ, 436, 292

Hartigan, P., Edwards, S., & Ghandour, L. 1995, ApJ, 452, 736

Hartigan, P., Morse, J. A., Heathcote, S., & Cecil, G. 1993, ApJ, 414, L121

Hartigan, P., Morse, J. A., & Raymond, J. 1994, ApJ, 436, 125

Hartigan, P., Morse, J. A., Reipurth, B., Heathcote, S., & Bally, J. 2001, ApJ, 559, L157

Hartigan, P., Raymond, J., & Hartmann, L. 1987, ApJ, 316, 323

Hartmann, L. 1998, Accretion Processes in Star Formation (Accretion processes in star formation / Lee Hartmann. Cambridge, UK ; New York : Cambridge University Press, 1998. (Cambridge astrophysics series ; 32) ISBN 0521435072.)

Heathcote, S., Morse, J. A., Hartigan, P., et al. 1996, AJ, 112, 1141

Heathcote, S. & Reipurth, B. 1992, AJ, 104, 2193

Herbig, G. H. 1960, ApJS, 4, 337

Hirth, G. A., Mundt, R., & Solf, J. 1997, A&AS, 126, 437

Indebetouw, R. & Noriega-Crespo, A. 1995, AJ, 109, 752

Isella, A. & Natta, A. 2005, A&A, 438, 899

Johansson, S. 1978, Phys. Scr, 18, 217

Joy, A. H. 1945, ApJ, 102, 168

Kenyon, S. J., Hartmann, L. W., Strom, K. M., & Strom, S. E. 1990, AJ, 99, 869

Kirk, J. M., Ward-Thompson, D., & André, P. 2002, in EAS Publications Series, Vol. 4, EAS Publications Series, ed. M. Giard, J. P. Bernard, A. Klotz, & I. Ristorcelli, 321–321

Konigl, A. & Pudritz, R. E. 2000, Protostars and Planets IV, 759

Koo, B.-C., Moon, D.-S., Lee, H.-G., Lee, J.-J., & Matthews, K. 2007, ApJ, 657, 308

Lada, C. J. 1987, in IAU Symposium, Vol. 115, Star Forming Regions, ed. M. Peimbert & J. Jugaku, 1–17

Lada, C. J. & Wilking, B. A. 1984, ApJ, 287, 610

Lavalley, C., Cabrit, S., Dougados, C., Ferruit, P., & Bacon, R. 1997, A&A, 327, 671

Lavalley-Fouquet, C., Cabrit, S., & Dougados, C. 2000, A&A, 356, L41

Lee, C.-F., Ho, P. T. P., Beuther, H., et al. 2006, ApJ, 639, 292

McCaughrean, M., Zinnecker, H., Andersen, M., Meeus, G., & Lodieu, N. 2002, The Messenger, 109, 28

McGroarty, F. & Ray, T. P. 2004, A&A, 420, 975

Moro-Martín, A., Cernicharo, J., Noriega-Crespo, A., & Martín-Pintado, J. 1999, ApJ, 520, L111

Motte, F., Andre, P., & Neri, R. 1998, A&A, 336, 150

Muzerolle, J., Hartmann, L., & Calvet, N. 1998, AJ, 116, 2965

Muzerolle, J., Hillenbrand, L., Calvet, N., Briceño, C., & Hartmann, L. 2003, ApJ, 592, 266

Natta, A., Testi, L., & Randich, S. 2006, A&A, 452, 245

Nisini, B., Antoniucci, S., Giannini, T., & Lorenzetti, D. 2005a, A&A, 429, 543

Nisini, B., Bacciotti, F., Giannini, T., et al. 2005b, A&A, 441, 159 (N05)

Nisini, B., Caratti o Garatti, A., Giannini, T., & Lorenzetti, D. 2002, A&A, 393, 1035

Nussbaumer, H. & Storey, P. J. 1988, A&A, 193, 327

Oliva, E., Marconi, A., Maiolino, R., et al. 2001, A&A, 369, L5

Osterbrock, D. E. & Ferland, G. J. 2006, Astrophysics of gaseous nebulae and active galactic nuclei (Astrophysics of gaseous nebulae and active galactic nuclei, 2nd. ed. by D.E. Osterbrock and G.J. Ferland. Sausalito, CA: University Science Books, 2006)

Palla, F. & Stahler, S. W. 1993, ApJ, 418, 414

Pesenti, N., Dougados, C., Cabrit, S., et al. 2003, A&A, 410, 155

Pesenti, N., Dougados, C., Cabrit, S., O'Brien, D., & Garcia, P. J. V. 2004, Ap&SS, 292, 539

Podio, L., Bacciotti, F., Nisini, B., et al. 2006, A&A, 456, 189 (P06)

Pravdo, S. H., Rodriguez, L. F., Curiel, S., et al. 1985, ApJ, 293, L35

Pudritz, R. E., Ouyed, R., Fendt, C., & Brandenburg, A. 2007, in Protostars and Planets V, ed. B. Reipurth, D. Jewitt, & K. Keil, 277–294

Pyo, T.-S., Hayashi, M., Kobayashi, N., et al. 2002, ApJ, 570, 724

Pyo, T.-S., Hayashi, M., Kobayashi, N., et al. 2006, ApJ, 649, 836

Quinet, P., Le Dourneuf, M., & Zeippen, C. J. 1996, A&AS, 120, 361

Raga, A. & Noriega-Crespo, A. 1998, AJ, 116, 2943

Raga, A. C., Velázquez, P. F., Cantó, J., & Masciadri, E. 2002, A&A, 395, 647

Ray, T., Dougados, C., Bacciotti, F., Eisl´offel, J., & Chrysostomou, A. 2007, in Protostars and Planets V, ed. B. Reipurth, D. Jewitt, & K. Keil, 231–244

Reipurth, B., Chini, R., Krugel, E., Kreysa, E., & Sievers, A. 1993, A&A, 273, 221

Reipurth, B., Hartigan, P., Heathcote, S., Morse, J. A., & Bally, J. 1997, AJ, 114, 757

Reipurth, B., Heathcote, S., Morse, J., Hartigan, P., & Bally, J. 2002, AJ, 123, 362

Reipurth, B., Heathcote, S., Yu, K. C., Bally, J., & Rodríguez, L. F. 2000a, ApJ, 534, 317

Reipurth, B. & Wamsteker, W. 1983, A&A, 119, 14

Reipurth, B., Yu, K. C., Heathcote, S., Bally, J., & Rodríguez, L. F. 2000b, AJ, 120, 1449

Reipurth, B., Yu, K. C., Rodríguez, L. F., Heathcote, S., & Bally, J. 1999, A&A, 352, L83

Schwartz, R. D. 1975, ApJ, 195, 631

Shang, H., Shu, F. H., & Glassgold, A. E. 1998, ApJ, 493, L91+

Shu, F. H., Najita, J., Ostriker, E. C., & Shang, H. 1995, ApJ, 455, L155+

Shu, F. H., Najita, J. R., Shang, H., & Li, Z.-Y. 2000, Protostars and Planets IV, 789

Siess, L., Dufour, E., & Forestini, M. 2000, A&A, 358, 593

Smith, N. & Hartigan, P. 2006, ApJ, 638, 1045

Solf, J., Raga, A. C., Boehm, K. H., & Noriega-Crespo, A. 1991, AJ, 102, 1147

Stanghellini, L., Shaw, R. A., Balick, B., et al. 2003, ApJ, 596, 997

Sturm, E., Lutz, D., Verma, A., et al. 2002, A&A, 393, 821

Takami, M., Chrysostomou, A., Ray, T. P., et al. 2004, A&A, 416, 213

Takami, M., Chrysostomou, A., Ray, T. P., et al. 2006, ApJ, 641, 357

Terebey, S., Shu, F. H., & Cassen, P. 1984, ApJ, 286, 529

Velusamy, T., Langer, W. D., & Marsh, K. A. 2007, ApJ, 668, L159

White, R. J. & Ghez, A. M. 2001, ApJ, 556, 265

White, R. J. & Hillenbrand, L. A. 2004, ApJ, 616, 998

Williams, J. P., Blitz, L., & McKee, C. F. 2000, Protostars and Planets IV, 97

Wiseman, J., Wootten, A., Zinnecker, H., & McCaughrean, M. 2001, ApJ, 550, L87

Woitas, J., Ray, T. P., Bacciotti, F., Davis, C. J., & Eislöffel, J. 2002, ApJ, 580, 336

Zinnecker, H., Mundt, R., Geballe, T. R., & Zealey, W. J. 1989, ApJ, 342, 337

Acknowledgments

The work presented in this thesis is part of a larger collaboration between the writer, Brunella Nisini, Teresa Giannini (INAF - Osservatorio Astronomico di Roma), Jochen Eislöffel (Thüringer Landessternwarte Tautenburg) and Francesca Bacciotti (INAF - Osservatorio Astrofisico di Arcetri). The data presented in this work have been collected at the ESO VLT telescope by Dr. Teresa Giannini, Dr. Simone Antoniucci and Dr. Linda Podio.

Firstly, I would like to thank Dr. Brunella Nisini and Dr. Jochen Eislöffel for firstly giving me the opportunity to participate in the JETSET network and also for their help. I have enjoyed fruitful discussions within all the JETSETers. I would like to especially thank Dr. Brunella Nisini for her patience during these last three years.

I am especially grateful to Alessio for his help and encouragement.

Lastly, I would like also to thank my parents Maria Raquel and Jose Maria. Everything I have achieved is because of the sacrifices they have made on my behalf.